The Pennsylvania State University

The Graduate School

ANALYSIS OF ORIFICE METERING AND PERFORATION EROSION FOR SHALE GAS WELLS VIA COMPUTATIONAL FLUID DYNAMICS (CFD) MODELING

A Dissertation in

Energy and Mineral Engineering

by

Yiming Zhang

Submitted in Partial Fulfillment
of the Requirements
for the Degree of

Doctor of Philosophy

August 2022

The dissertation of Yiming Zhang was reviewed and approved by the following:

John Yilin Wang
Associate Professor of Petroleum and Natural Gas Engineering
Dissertation Advisor
Chair of Committee

Derek Elsworth
Professor of Energy and Geo-Environmental Engineering

Gregory King
Professor of Practice, Petroleum and Natural Gas Engineering

Xiang Yang
Assistant Professor, Mechanical Engineering

Mort D. Webster
Professor of Energy Engineering
Associated Department Head for Graduate Education

ABSTRACT

Coriolis, turbine, V-cone, and orifice meters have been used in measurement of gas production in shale wells. However, shale gas wells are producing at high flow rates, high pressure, and possibly gas compositions change, which might affect volumetric measurement accuracy that was developed for conventional gas wells. Thus, it is critical to investigate the metering and measurements technologies that are being applied in shale gas wells to further understand and improve the accuracy of gas volumetric measurements. This paper provides a comprehensive review and analysis of background information, design, measurement, and uncertainties associated with Coriolis meters, turbine meters, V-cone meters, and orifice meters. We also discussed the lessons learned through our field experiences in computing gas volumes using SCADA information in shale gas and conventional gas production.

Flange-tapped concentric orifice meters are commonly used in measurement of shale gas production volumes due to their low cost, accuracy, and ease of maintenance compared to other types of meters. Computational Fluid Dynamics (CFD) models were established to numerically analyze the flow field for an orifice meter and its associated uncertainties, including chemical and organic contamination and solid particle erosion. The base model for the orifice was implemented and validated against experimental data and the same methodology is used to perform parametric studies on the uncertainty effects.

The effect of chemical and organic contamination layer on the orifice plate is studied by changing the length and width of the layer from the upstream or the downstream side of the plate. The results showed the most changes of discharge coefficient occur when

the layer is half of the plate length. The results also showed the changes of discharge coefficient increase with the increase in width of the layer.

For the solid particle erosion on the orifice plate, we observed smaller particle sizes would lead to an increase in maximum erosion on the orifice plate while and increase of gas flow rate would also lead to an increase in maximum erosion on the orifice plate. However, the solid particles entering with the measuring fluid will cause minimal erosion to the orifice plate as the erosion rate are negligible.

Research on fluid flow through orifice is helpful in establishing criteria for the analysis of perforation erosion, as field and experimental data have shown that slurry erodes perforations during shale gas stimulation, which invalidates the assumption of a constant coefficient of discharge used in the past. However, perforation erosion is not fully understood yet.

In this work, a perforation erosion model was built using CFD and validated against laboratory data. We then conducted parametric studies to investigate the impact of treatment rate, proppant concentration, proppant size, and fluid viscosity on perforation erosion.

Our results demonstrated that higher treatment rate and larger proppant lead to higher erosion to the perforation diameter. Perforation erosion decreased when fluid viscosities increased from 10 *cp* to 100 *cp*, and then increased when the fluid viscosity was increased to 1,000 *cp*. Our new understandings could be applied to improve perforation design in shale wells.

TABLE OF CONTENTS

LIST OF FIGURES

LIST OF TABLES

ACKNOWLEDGEMENTS

First and foremost, I would like to express my sincere gratitude to my advisor, Dr. John Yilin Wang, for his constant guidance, encouragement, and patience throughout my Ph.D. journey. Dr. Wang always able to guide me through during the many obstacles I have faced during my research. My skills as a researcher and as a person have grown tremendously under the influence from his knowledge, experience, and personality. Working with Dr. Wang is such an invaluable experience for me and I feel very proud to be one of his Ph.D. graduates.

I would like to thank Dr. Derek Elsworth, Dr. Gregory King, and Dr. Xiang Yang for their time, effort, and guidance as a part of the committee members through their busy schedules. Their wisdom and knowledge led to insightful suggestions toward the progress of this research. I would also like to thank Dr. Turgay Ertekin for his influence and guidance throughout my career as a graduate student.

I would like to thank Qian Sun and Miao Zhang for their help and encouragement throughout these years as a graduate student, especially when I came across difficulties.

Last but not least, I would like to thank my mother, Dr. Wenxia Zhang, for her tremendous support and unconditional love.

Chapter 1

Introduction

Erosion due to particles occurs in oil and gas industry under a wide range of flow conditions. For low flow applications, failure due to erosion may not even happen or could take many years to become noticeable. However, there are flow regimes that can cause significant erosion such as erosion in flow through restrictions.

Solid particles erosion has been one of the serious problems in many oil and natural gas applications, as produced oil and natural gas streams typically carry a significant amount of sand along with the flow. Pipe fittings and equipment such as orifice plates, chokes, valves, and sudden contraction/expansions rapidly discharge the fluid resulting in much faster fluid velocities. These types of flow regimes can cause rapid erosion on the equipment as well as the pipe walls, thus lead to inaccurate measurements and safety concerns.

Flange-tapped concentric orifice meters are commonly used in measurement of shale gas production volumes due to their low cost, accuracy, and ease of maintenance compared to other types of meters. Flow through orifice meter can be viewed as flows through restrictions, as thin orifice plate, thick orifice plate, and sudden contraction/expansion are differentiate based on the plate thickness to the plate diameter ratio.

With the successful development of shale gas resources in U.S., a large number of shale gas wells were put on-line and supplying large amount of gas as energy and raw materials for industries, power plants, buildings, homes, etc. However, shale gas wells are producing at high flow rates, high pressure, and possibly gas compositional change, which affect gas measurement accuracy using AGA method that was developed for conventional gas wells. Thus, it is critical to investigate the metering and measurements technologies that are being applied in shale gas wells to further understand and improve the accuracy of gas volumetric measurements.

Multistage hydraulic fracturing of horizontal wells has been widely used in developing unconventional reservoirs, especially for shale gas reservoirs. Plug-and-perf completions are one of the most commonly used completion methods for horizontal wells in unconventional reservoirs. The plug-and-perf system stimulates the wells by creating multiple isolated fracturing stages. The stages are completed with a cemented casing or liners as it combines two common fracturing techniques: limited entry and segmented fracturing. Numerical simulation studies done by various researchers have shown that the limited-entry can effectively promote the uniform growth of fractures in multi-stage hydraulic fracturing. However, there are instances where some fractures within the treatment began to propagate at a lower rate or even stopped growing after proppants were pumped. This indicates the proppant-carrying fracturing fluid flowing with high velocity erodes the perforations during fracturing, making the perforations lose their ability of limited entry.

In designing the completions of a horizontal shale well, the perforations can be viewed as another application for flow through restrictions, similar to orifice flow. Proppants erode the perforation edge when they pass through a perforation during a treatment, leading to simultaneous increase in both coefficient of discharge and perforation diameter (**Figure 1-1**). The increase of either of these parameters will also increase flow capacity of the perforations and creates pressure drop for the perforations.

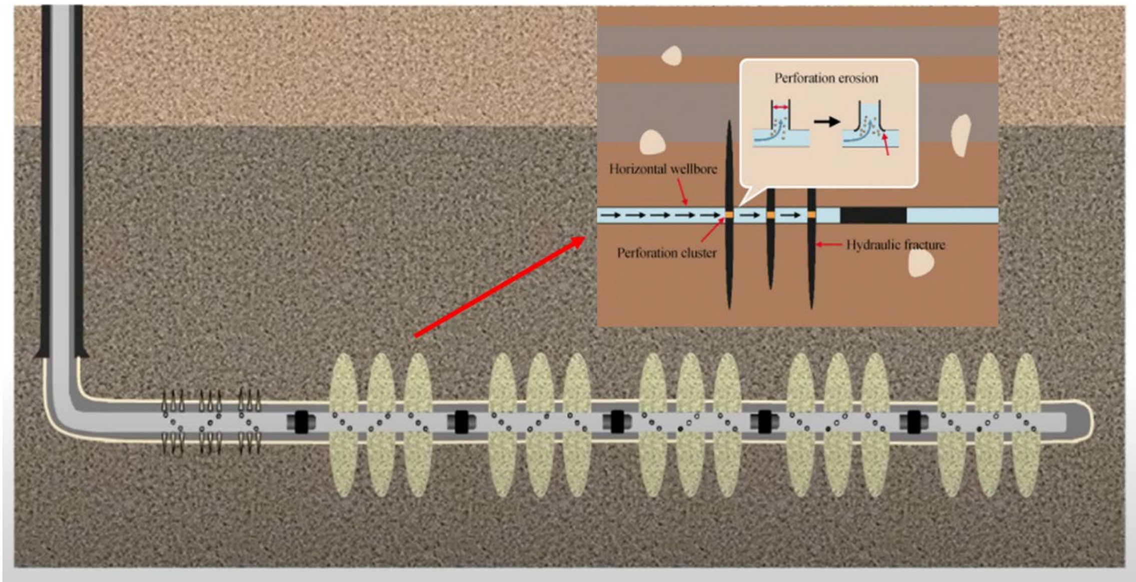

Figure **1-1**: Perforation Erosion in Multistage Hydraulic Fracture (Li et. al, 2017)

Understanding of erosion phenomenon plays a critical role in the oil and gas industry, including measurements and fractures treatments. However, it has not been fully understood especially with the large amount of stimulation fluids and proppants when it comes to hydraulic fracturing. Most of the times, coefficient of discharge was assumed to be constant or estimated using a simplified correlation. When it comes to perforation erosion inspection, existing magnetic, acoustic and caliper tools do not offer the resolution required to quantify the detailed erosional patterns, shapes, and diameter increases that perforations experience (Robinson 2020).

Computational Fluid Dynamics (CFD) based erosion models for flows in complex geometries have been developed recently to examine erosions numerically. For CFD based erosion modeling, it typically consists of three main steps: a flow model, a particle tracking model, and an erosion model. The next objective of this research is to analyze and understand perforation erosion through a comprehensive and systematic numerical experiment after building a state of art perforation erosion model via CFD and to develop charts and correlations for more accurate estimation of coefficient of discharge in the stimulation of shale reservoirs.

Chapter 2 provides a comprehensive and critical review and analysis of background information, design, measurement, and uncertainties for Coriolis meters, turbine meters, v-cone meters, and orifice meters.

Chapter 3 includes the development of orifice models via CFD modeling for numerical analysis and orifice meter uncertainty analysis.

Chapter 4 reviews the literatures related to perforation erosion in shale reservoirs, including lab results, field experiments, imaging, and numerical studies. It also includes the development of perforation erosion model via CFD modeling for numerical analysis and parametric studies.

Chapter 3, and Chapter 4 share the same methodology for the flow model, particle tracking model, and erosion model. Chapter 3 and Chapter 4 also share the same model validations for erosion CFD model.

Chapter 5 provides an overall summary of all the studies conducted in this paper as well as recommendations and future works.

Chapter 2

Review of Metering and Gas Measurements in High-Volume Shale Gas Wells[1]

Abstract

Coriolis, turbine, V-cone, and orifice meters have been used in measurement of gas production in shale wells. Flange-tapped concentric orifice meters are commonly used in measurement of shale gas production volumes due to their low cost, accuracy, and ease of maintenance compared to other types of meters.

However, shale gas wells are producing at high flow rates, high pressure, and possibly gas compositions change, which might affect volumetric measurement accuracy that was developed for conventional gas wells. Thus, it is critical to investigate the metering and measurements technologies that are being applied in shale gas wells to further understand and improve the accuracy of gas volumetric measurements.

This paper provides a comprehensive review and analysis of background information, design, measurement, and uncertainties associated with Coriolis meters, turbine meters, V-cone meters, and orifice meters. We also discussed the lessons learned through our field experiences in computing gas volumes using SCADA information in shale gas and conventional gas production.

---

[1] This chapter has been submitted to and published on the Journal of Petroleum Exploration and Production Technology (Springer):
Zhang, Y., Wang, J. Review of metering and gas measurements in high-volume shale gas wells. *J Petrol Explor Prod Technol* **12,** 1561–1594 (2022). https://doi.org/10.1007/s13202-021-01395-9

2.1 Coriolis Meter

2.1.1 Background Information

Coriolis mass flowmeters were introduced in the early 1980s for natural gas measurements and gained popularity in many gas flow applications in the past few decades due to the meters' improved accuracy and the capability of measuring the mass flow rate directly. The first application of Coriolis meters was proposed by Li and Lee in 1953 for liquid measurement, as the meter was proved successful for mass flow measurement of liquids with reliable accuracy prior to the application for natural gas measurements. However, due to the relatively low density of gas compared to liquids, the Coriolis effect induced by the gas mass flow was too small for the frequency phase change to be detected (about three orders of magnitude smaller than liquid). Kolahi et al. (1994) presents a Coriolis meter prototype to measure the gas mass flow under normal conditions in their studies. They first studied whether the Coriolis effects can be amplified by increasing the radial velocity of the tube. Since gas cannot be considered as incompressible fluid, the increase in the radial profile would not amplify the torsional oscillation unlimitedly and the Coriolis forces and torsional amplitude would eventually start to decrease. Their design of the prototype meter consisted of dual vibrating U-shaped tubes with tunable eigenfrequency designed for low density fluids measuring purposes. Their prototype results in an amplification of the torsional amplitude by a factor of 100, allowing the gas mass flow to be measured under normal conditions. Their works have opened up the possibilities for the Coriolis gas measurements applications.

Stewart (2002) performed experimental studies to assure the gas measurement quality using Coriolis meters with water calibration for validation. The measurements for water calibration were within ±0.1% as expected, but only one of the meters falls within ±0.5% of mass flow rates for air calibrations, with some of the meters displayed unexpected behavior. Grimley (2002) performed laboratory tests on Coriolis meters with natural gas using five Coriolis meters from three different manufacturers. The testing meters consist of the beam-mode dual bent-tube and shell-mode Coriolis meter designs. The natural gas flows were tested with a critical nozzle as the reference ranging from 180 to 1,000 psi. The gas flow measurements showed promises using water calibration as the results fall within the uncertainty level of the reference meter. Wang and Baker (2014) provided a comprehensive review of Coriolis flow measurement technology over the past two decades across a wide range of fields and applications.

API first published methods to achieve custody transfer levels of accuracy when a Coriolis mass meter is used to measure liquid hydrocarbons (API, 2002). American Gas Association (2001) also published *Measurement of Natural Gas by Coriolis Meter*, which is one of the most notable publications on Coriolis mass meters as their acceptance grows rapidly.

2.1.2 Design

Coriolis mass meter, **Figure 2-1**, directly measures the mass flow rate of a fluid by vibrating a fluid-conveying tube at resonance. Coriolis meters can be categorized into rotary or vibratory types, with rotary types are more commonly used for bulk solid applications whereas the vibratory types are designed for fluid measurement applications. Common configurations include dual or single U-shaped, horseshoe-shaped, tennis-racket-shaped, or straight flow tubes with inlet on one side and outlet on the other as shown in **Figure 2-2**. Dual-tube meters with a deep U shape configuration have the highest sensitivity to flow and the lowest pressure drop at a given accuracy, providing the advantage of having the widest range of flowrates. The dual-tube deep-U meter designs are optimal for low-mass-flow applications such as gases and high-viscosity liquids (O'banion, 2013). The two U-shaped flow tubes spilt the flow entering from the pipeline by the inlet manifold and rejoin at an outlet manifold then continue down the pipeline. However, the dual- tube designs require flow splitters that are prone to plugging, whereas the single tube designs offer a better solution in applications with such fluids. For single tube designs the tube length increases dramatically as they would require more spaces and also results in increased pressure loss due to the pipe length. Every commercially available Coriolis mass meters all have an electromagnetic drive system consisting of a magnet and a coil causes the tube to vibrate toward and away from each other at their resonant frequency. This frequency is determined by the tubes' stiffness and their mass.

A Coriolis mass meter typically consists of two main components with the primary element being electromagnetic sensors (pickoff sensors) and a secondary unit of a driver (transmitter). At zero flow, both the inlet and outlet sinusoidal waves are in phase with each other. Under flowing conditions, when an oscillating excitation force is applied to the tube causing it to vibrate, the fluid flowing through the tube will induce a rotation or twist to the tube due to the Coriolis Effect acting in the opposite direction on either side of the applied force. Working principle of a Coriolis mass meter is presented in **Figure 2-3**. The amount of twist creates the phase difference (*dt*, time lag) measured by the transmitter between the pickoff sensors on the inlet and outlet sides which directly correlates with the mass flow through the tube.

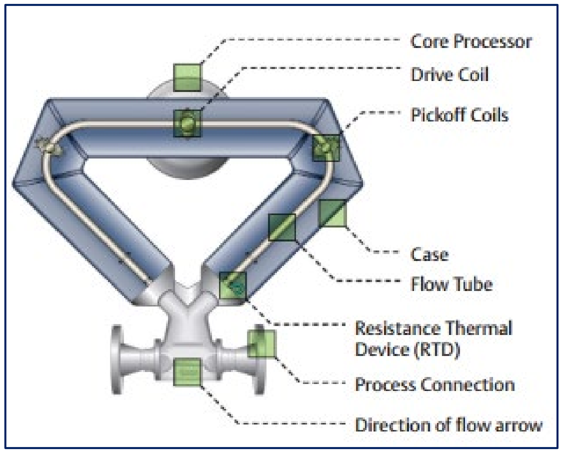

Figure **2-1** Coriolis Mass Meter (Stappert, 2013)

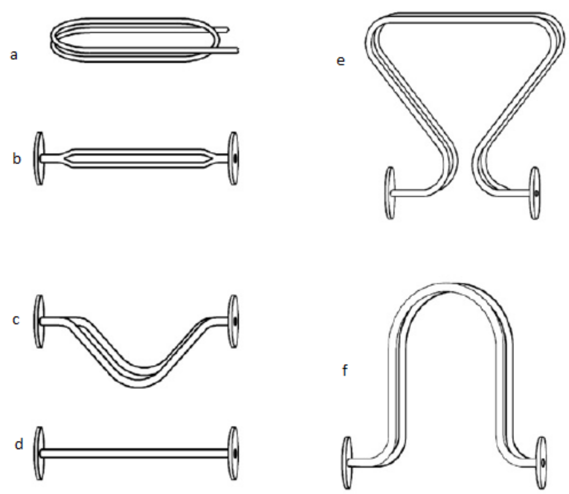

Figure **2-2** Geometries of various Coriolis mass flowmeters (Anklin, 2006), a) bended single tube, b) dual straight tubes, c) V-shaped bended twin tubes, d) single straight tube, e) horseshoe-shaped twin tubes, f) curved twin-tubes

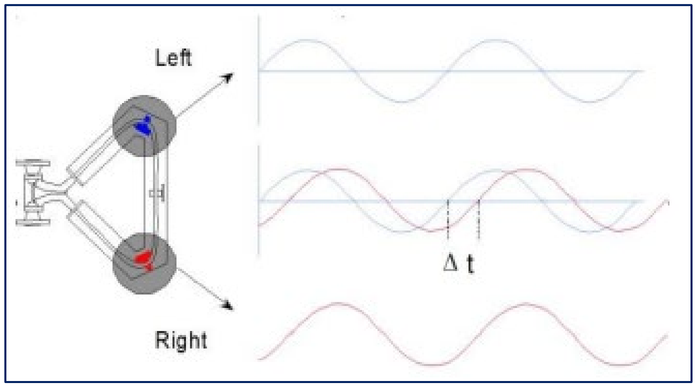

Figure **2-3** Coriolis Sensing/Pickoff Signals (Stappert, 2013)

Coriolis mass meters are expensive in terms of capital costs compared to other types of meters, and their price increases rapidly as the size of the meter goes up. The meter unit's weight also goes up significantly with size. However, since this type of meters does not require flow conditioners along with their low maintenance and high reliability, it can be advantageous in terms of life cycle costs. In a simple cost-analysis study of comparison between a small Coriolis meter and an orifice meter setup, O'banion demonstrates the long-term cost for the small Coriolis mass meter is about 55%-76% of an orifice meter over 10 years, with the capital cost of the Coriolis mass meter at four to seven times of the latter (O'banion, 2013).

Coriolis mass meters are limited in terms of range of sizes as well as the configuration of tubes, which may not be suitable for measuring large mass flow rate without resulting in excessive pressure drop. Each meter size and type have a pressure drop characteristic curve that is prepared by the manufacturers as illustrated in **Figure 2-4**. The curve shows the tradeoff between pressure drop and flow accuracy and the user must accommodate for the selection of a specific Coriolis mass meter to balance pressure drop and accuracy.

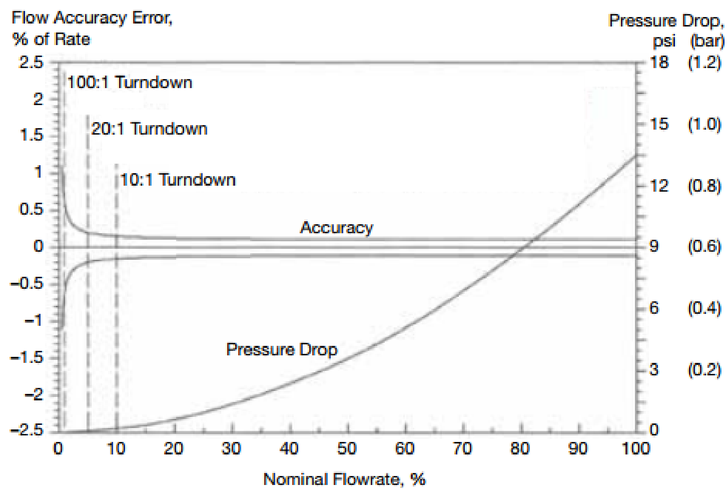

Figure **2-4** Coriolis mass meter pressure drop (O'banion, 2013)

The Tek-Cor 1100A series Coriolis flow meter consists of line sizes ranging from 0.5 to 6 inch for gas measurements with accuracy up to ±0.5% (based on water measurement under standard conditions), density accuracy up to ±0.001 g/cm^3, and repeatability up to ±0.25%. The sensor types for this model series include standard (dual U-tubes), U-tube, nano, super bend, straight tube, and dual path. It is recommended to have velocity less than one third of the sound velocity for gas measurement as high-speed gas flow introduces loud noise that can interfere with the accuracy of the measurements (Tek-Trol, 2021).

The Micro-Bend Coriolis mass flowmeter ALCM-MB from SmartMeasurement consists of line sizes ranging from 0.5 to 8 inch for gas measurements with accuracy up to ±0.5 % (based on water measurement under standard conditions), density accuracy up to ±0.001 g/cm3, and repeatability up to 0.075%. It employs a unique U-tube design with a significantly smaller radius compared to the traditional U-tube type Coriolis meters as the compact design can significantly reduce pressure differential. The construction of the meter is typically built with 304 stainless steel (SmartMeasurement, 2019).

Micro Motion has several series of Coriolis Meter includes ELITE, F-Series, and T-Series as they are capable for gas measurements. The ELITE series consists of line sizes ranging from 1/12 to 16 inch for gas measurements with accuracy up to ±0.35% and repeatability up to ±0.20%. The F-Series consists of line sizes ranging from 0.25 to 4 inch for gas measurements with accuracy up to ±0.50% and repeatability up to ±0.25%. The T-Series consists of line sizes ranging from 0.25 to 2 inch for gas measurements with accuracy up to ±0.50% and repeatability up to ±0.05% (Emerson, 2021b).

2.1.3 Measurement

A practical implementation for the curved tube Coriolis meter (**Figure 2-2f**) operating equation is shown in **Equation 2-1** (AGA No.11, 2001). Equations and methods for the conversion of mass to base volume are documented in AGA Report Number 11 and AGA Report Number 8, *Compressibility Factors for Natural Gas and Other Hydrocarbon Gases*. **Equation 2-2** shows the relationship between direct mass flow measurement and volumetric flow at base conditions. This equation is developed based on the conservation of mass and requires the knowledge of the gas composition to calculate base density using an equation of state.

$$q_m = FCF \times F_T \times F_P \times (\Delta t - \Delta t_0) \tag{2-1}$$

$$F_T = 1 - K_T T \tag{2-2}$$

$$F_P = 1 + K_P P \tag{2-3}$$

$$q_b = \frac{q_m}{\frac{P_b \times M_r}{Z_b \times R \times T_b}} \tag{2-4}$$

where:

q_b - Volumetric flow rate at base conditions, in cubic feet per hour

q_m - Mass flow measured by the Coriolis mass meter, in pounds per hour

q_f - Volumetric flow rate at line conditions, in cubic feet per hour

FCF - Flow calibration factor

F_T - Temperature compensation

K_T - Temperature coefficient (directly related to changing Young's modulus vs. temperature)

F_P - Pressure compensation

K_P – Pressure coefficient

M_r - Gas molar mass at base conditions, in pound mass per pound mole

P - Operating fluid pressure, in psi

P_b - Absolute pressure of the gas at base conditions, in psia

P_f - Pressure of the gas at line conditions, in psi

R - Universal gas constant

Δt - Phase induced by the flowing gas

Δt_0 - Residual phase at zero flow

T - Primary element flow tube temperature, in degree Fahrenheit

T_b - Absolute temperature of the gas at base conditions, in degree Rankine

T_f - Temperature of the gas at line conditions, in degree Rankine

Z_b - Fluid compressibility at base conditions

Z_f - Fluid compressibility at line conditions

Density is determined at no flow conditions by measuring the natural frequency of the tube containing the particular fluid. Electromagnetic sensors excite the measuring tubes at their resonance frequency and any changes in mass (thus the density) of the oscillating system (measuring tubes and fluid) will result in a change of the resonance frequency. The resonance frequency is directly related to the density of the fluid inside the tubes. Typically, a microprocessor flow computer will utilize this relationship in order to obtain the density signal of the fluid. Some manufacturers have dedicated gas density/specific gravity unit (SGU) devices for gas density measurements because changes in density are too small to resolve with Coriolis technology. AGA Report No.8, *Compressibility Factors of Natural Gas and Other Related Hydrocarbon Gases* can also be used as a reference in calculating the density of the flowing gas.

The temperature of the measuring tubes is determined in order to calculate the compensation factor due to any temperature effects. The flow computer utilizes this signal, which corresponds to the product temperature, along with the mass flow determination and density of the fluid to determine the volumetric flow accurately. Most Coriolis mass meters are equipped with a temperature sensor to compensate for any slight changes in the tube's stiffness (Young's modulus) resulted by the temperature.

Since it is not quite common in the industry to use mass measurement for custody transfers, with volume being equal to mass flow divided by density, a flow computer can convert the Coriolis mass meters' outputs into volume. The accuracy of volumetric flow rates measured by Coriolis mass meters would be dependent on the accuracy of both the density measurement as well as the mass measurement.

2.1.4 Uncertainties

Coriolis mass meters are well known for their phenomenal accuracy, ±0.1% for liquid mass and volume measurement accuracy, ±0.5% for gas's mass measurement accuracy, and error range of ±0.002 to ±0.0005 g/cm^3 for density measurement accuracy. They are also independent of flow profile, fluid composition, and material constants such as heat conductivity, heat capacity, and viscosity.

Such a single device can provide multivariable outputs, there are fewer instruments to specify, install, calibrate, and maintain, which makes Coriolis mass meters ideal for relatively low flow rate measurement ranging from 2.8 to 400 *lb/min* (or 64 to 9,500 SCFM) for gas measurements. Coriolis mass meters can measure the flow rate accurately over a 100:1 turndown ratio and density in the range of 0 to 5 g/cm^3. This type of mass meters is even suitable for liquid flow measurements with a small amount of gas, but it is ideal for single phase measurement. Coriolis mass meters are also bidirectional, which can handle flow in either direction with no adjustments Every Coriolis mass meter should be calibrated accordingly to the measuring fluid types prior to use. The uncertainty of the calibration is primarily affected by meter linearity, repeatability, and calibration reference uncertainty. Most manufacturers state an uncertainty of ±0.5% of mass flow rate which includes all of these effects. Most Coriolis mass meters operate on signal levels below 60 *microseconds* and can even detect *dt* as small as a few nanoseconds.

Since the amplitude of the oscillation from the Coriolis meters may be only a few tens of micrometers, the measurement can be very sensitive to even small disturbances. To minimize measurement errors from such effects, Coriolis meters must be balanced accurately. The symmetry of dual-tube designs offers the best performance for the decoupling of the meters from the external disturbances with its robust balancing system. For the single tube meters however, it is quite challenging and difficult to find a balancing mechanism that allows the meter to measure precisely under various external conditions and the changing in fluid densities.

Koudal et al. (1998) in their studies shown that the pulsation effects are not only crucial at the frequency of pulsation but also at frequency differences between the pulsation and the Coriolis effect frequency. Coriolis meters with high working frequencies are much less sensitive these external disturbances as the differences between the frequencies is high, typically above 200 *Hz*. Cheesewright et al. (2000) investigated the response of Coriolis meters to a variety of external disturbances. Their studies showed the Coriolis calibration accuracy is not affected by inlet flow conditions, such as upstream swirl effects, asymmetric flow profile, or increased turbulence. But for meter external disturbances, the tested Coriolis meters resulted in severe calibration errors at the presence of flow pulsations and/or mechanical vibrations at the Coriolis frequency. However, these errors are predominately due to failure of the outdated phase measurement algorithm, they can be overcome by using high performance filtering techniques, especially with the improved designs of Coriolis meters to minimize the effect of external influences. The disturbances at frequencies close to the meter drive frequency will produce measurement errors.

Bobovnik et al. (2005) developed a fully coupled, partitioned, numerical model using finite volume method (FVM) for the turbulent fluid flow and finite element method (FEM) for the deformable shell structure for a straight-tube Coriolis meter. The FVM/FEM numerical model was validated with the solutions of the Euler beam one-dimensional flow model and the Flügge shell and potential flow model. Mole et al. (2008) improved upon the iterative coupling method by introducing forced vibration simulation into the model. The effects of Reynolds number on a straight flow tube were analyzed using this improved model and results agreed well with weight vector analysis conducted by Kutin et al. (2006). Bobovnik et al. used this iterative coupling method to study the effects of disturbed velocity profiles due to installation effects for a short straight tube full-bore design (2013) and single and twin tube (2015).

Pope and Wright (2014) conducted experiments to analyze the performance of Coriolis meters in transient gas flow using nitrogen and helium gases through two Coriolis meters at the National Institute of Standards and Technology's Transient Flow Facility. Both meters were capable of measuring the totalized mass from the transient flows within 1.0%.

For natural gas measurements, Anklin et al. (2006) described due to the low density of the flowing gas, Coriolis mass meters for gas applications are often used near the lower end of their rangeability. The performance of the gas mass measurement will be increased with higher mass flow. The turndown of the mass meter can also be improved by increasing the inline pressure of the flowing gas, which is why it is recommended to have the Coriolis meter be installed at the high-pressure side. The preferred orientation of installation for gas applications is to install the meter vertically with the flow direction upwards. This set up allows the entrained solids to sink downwards as the gases flowing upwards when the medium is not flowing; this also protects the meter and tubes from solids build up as well as draining the meter tubes completely.

Anklin et al. (2006) describes the effects of corrosion and erosion to the Coriolis metering system, as these effects will diminish the wall thickness thus change the stiffness of the tube. The results can lead to inaccuracy in mass measurements and safety issues. For strongly abrasive fluids, erosion can be reduced by keeping the flow velocity low. The effects of erosion are also the smallest for straight single tube meters. There are built-in diagnostic implementations for Coriolis meters available for detecting corrosion or erosion.

2.2 Turbine Meter

2.2.1 Background Information

Turbine meter measures volumetric flow rate by counting the revolutions of a rotor inside the meter as the angular velocity of the rotor is proportional to the gas flow velocity. The idea of such a meter can be dated all the way back to the ancient Rome, as Roman architect Vitruvius developed one of the first odometer primary used as a surveying instrument consisted of a wheel of known circumference that dropped a pebble into a container on every rotation. Robert Hook utilized the mechanics of a small windmill in 1681 to measure air velocity based on the windmill's rotations and eventually implemented as a distance meter for naval ships.

The first modern Turbine meters were developed in 1938 in the United States, consisting of a helically bladed rotor and simple bearings as they became quite popular for fuel flow measurement in airborne applications. In 1961, Potter developed and patented his version of Turbine meter. As Potter profiles the hub of the rotor, the observations of the pressure balance across the rotor held it against the axial drag forces rather than the thrust bearings, which led to the implementation of his meter to allow the rotor to run on a single journal bearing.

2.2.2 Design

Turbine meter converts the kinetic energy of the flowing fluid into rotational energy. For an ideal turbine meter, barring any drag forces, the rotational speed of the rotor inside the meter would be directly proportional to the volumetric flow rate of the measuring fluid. In practice however, the drag forces from the system can slightly retard the rotation and lead to a non-linearity relationship for the measuring mechanisms. These drag forces include frictional drag on the blades, the hub, the faces of the rotor, and the tip of the blades; bearing drag; magnetic drag due to the means by which the rotation is measured (Baker, 1991).

A typical Turbine meter consists of either straight or helical blades and designed to create the minimum disturbance to the oncoming flow. The advantages of the helical blades are due to the relative angle of approach of the fluid on to the blades whereas the straight blades will not allow a constant angle of attack, which lead to unnecessarily large incidence angles and introduce flow disturbance and drag. The rotor spindle must be held centrally in the pipe in bearings, which are commonly used as flow straighteners as they reduce swirl due to conservation of angular momentum as the fluid redistributed into the annular passage past the blades. The rotation of the rotor is sensed most commonly by a change in the magnetic field around the sensor.

For a gas turbine meter, the most obviously differences in design are the large hub and comparatively small flow passage, allowing the fluid to impart as large a torque as possible on the rotor by moving the flow to the maximum radius and increasing the flow velocity. **Figure 2-5** shows a schematic of axial-flow, single-rotor gas Turbine meter. The flowing gas enters the meter increases in velocity through the annular passage formed by the nose cone and the interior wall of the body. The movement of the gas over the angled rotor blades rotates the rotor and the rotation is registered by either a mechanical or an electrical readout. Another type of gas Turbine meter, shown in **Figure 2-6**, consists of a dual-rotor design with a secondary rotor placed behind the primary rotor. The primary rotor still serves the same function as the single rotor system. The secondary rotor downstream from the main rotor typically operates at a lower speed than the main rotor in order to extend its service life and differentiate the measurements of the two rotors for validation purposes. Some of the dual-rotor designs also provide self-diagnostic and self-correction capabilities as the secondary rotor can provide measurement adjustments to improve the output error from the primary rotor.

The rotor material is typically made of Delrin or aluminum for sizes greater than six inch. Number of blades are typically 12 to 24 with the maximum pulse frequencies up to 3,000 Hz. The maximum pressure rating is up to 1,450 psi, but these figures can vary significantly among manufacturers. It is quite common to include an electrical readout as well as a mechanical register especially for gas Turbine meters.

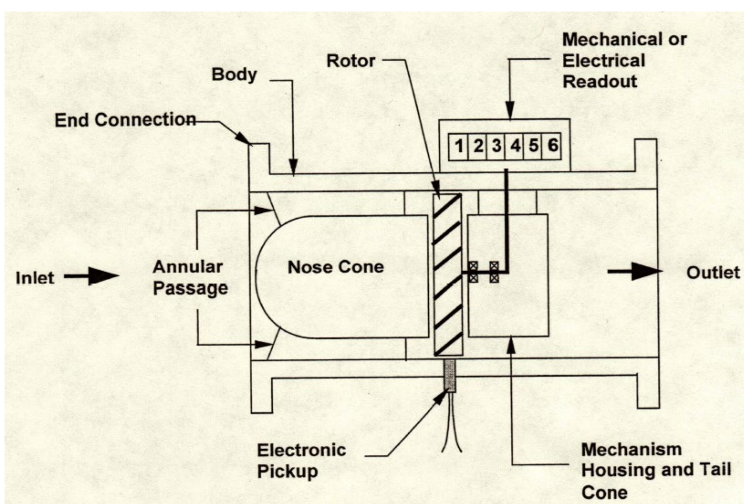

Figure **2-5** Single Rotor Turbine Meter, Gas Design (AGA 7, 2006)

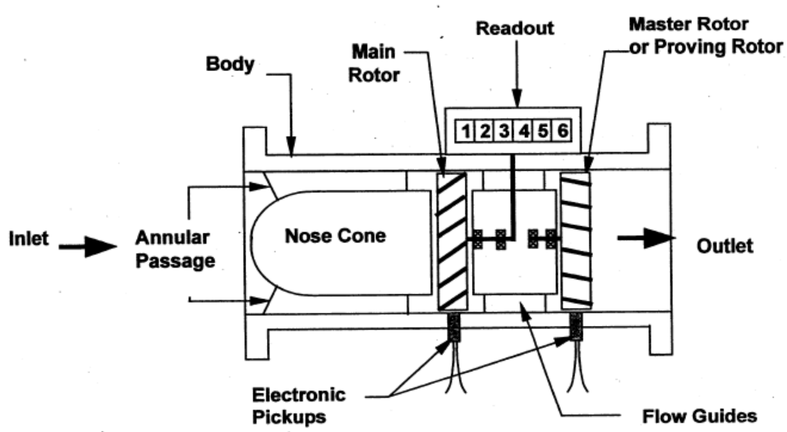

Figure **2-6** Dual-Rotor Turbine Meter with Independent Tandem Separated by Flow Guides (AGA 7, 2006)

2.2.3 Measurement

Turbine meter typically registers gas volume continuously at flowing pressure and temperature conditions converted on the rotor revolutions counted mechanically or electrically. For measurement, the registered volume must be corrected to the specified base conditions using the following equations (AGA 7, 2006).

$$V_b = V_f \left(\frac{P_f}{P_b}\right)\left(\frac{T_b}{T_f}\right)\left(\frac{Z_b}{Z_f}\right) \tag{2-5}$$

$$Q_f = \frac{V_f}{t} \tag{2-6}$$

$$Q_b = Q_f \left(\frac{P_f}{P_b}\right)\left(\frac{T_b}{T_f}\right)\left(\frac{Z_b}{Z_f}\right) \tag{2-7}$$

where:

V_b – Volume at base conditions, in cubic feet

V_f– Volume measured at flowing conditions during time interval t, in cubic feet

Q_b - Volumetric flow rate at base conditions, in cubic feet per hour

Q_f – Volumetric flow rate at flowing conditions, in cubic feet per hour

P_b - Absolute pressure of the gas at base conditions, in psia

P_f - Pressure of the gas at flowing conditions, in psi

t – Time, in hour

T_b - Absolute temperature of the gas at base conditions, in degree Rankine

T_f - Temperature of the gas at line conditions, in degree Rankine

Z_b - Fluid compressibility at base conditions

Z_f - Fluid compressibility at flowing conditions

2.2.4 Uncertainties

Gases entering the Turbine meter shall be clean and free of any liquids and dust. A filter with 5 μm filtration quality or better should be used if the gases are impure. The upstream pipe should also be cleaned before the installation of the meter. Maximum flow velocities can be up to 98.43 *ft/s* and excessive gas velocities can damage the meter, but 20% excess may be allowable for short periods. The Turbine meter is designed for horizontal orientation and shall be installed accordingly, as vertical orientation may introduce drags due to gravitational forces.

The linear performance for metering accuracy can be as good as ±0.5 for volume measurements on about 20:1 turndown ratio with repeatability of ±0.02%. The turndown ratio of a simple turbine meter increases proportionally with the square root of the gas density ratio. Griffiths et al. (1970) indicated in their studies that at a pressure of 290 *psi*, the turndown can be as high as 100:1 compared with 15:1 at working pressure close to atmosphere pressure. For each meter design and size, the manufacturer shall specify flow rate limits for Q_{min}, Q_t, and Q_{max}. The performance for a turbine meter can be summarized as shown in **Figure 2-7**.

where:

Q_{max} – The maximum gas flow rate through the meter that can be measured within the specified performance requirement

Q_{min} – The minimum gas flow rate through the meter that can be measured within the specified performance requirement

Q_t – The transition flow rate, the flow rate through the meter at which performance requirements may change

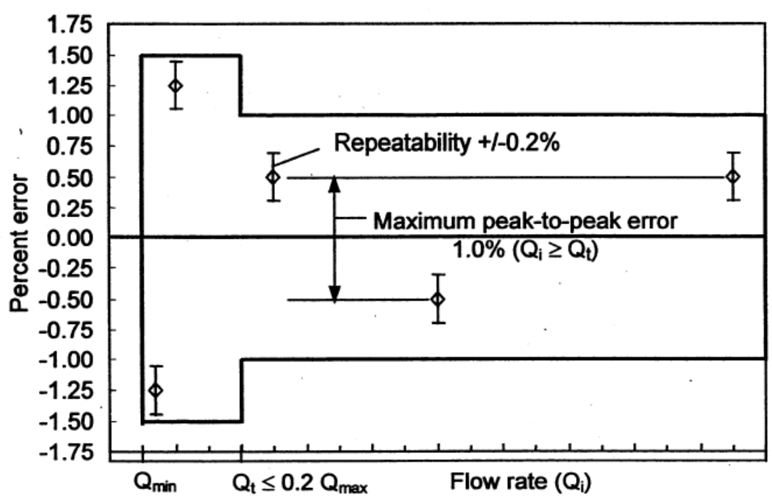

Figure **2-7** Turbine Meter Tolerances at Atmospheric Pressure (AGA 7, 2006)

2.3 V-Cone Meter

2.3.1 Background Information

The V-cone meter (cone meter) was introduced in the late 1980s by McCrometer, it is a type of differential meters, but unique as this type of design constricts the flow by positioning a cone in the center of the pipe. The cone design forces the high velocity core to mix with the lower velocity flows closer to the pipe walls. This design also allows the flow profile to be flattened under extreme conditions as V-cone forms very short vortices as the flow passes the cone. The low amplitude, high frequency signal produced by these short vortices ensures the stability of the signal. This implies that as different flow profiles approach the cone, there will always be a predictable flow profile at the cone, which ensures the measurement accuracy even in non-ideal conditions and reduces the permanent pressure loss. The cone meter is covered by international standards found in ISO 5167-5:2016.

2.3.2 Design

The V-cone meter, **Figure 2-8**, is designed to minimize the pressure loss and withstand years of normal wear from erosion and corrosion without developing any significant shifts in calibration due to its V-shaped restriction that has no critical surface dimensions or sharp edges that must remain within strict tolerances of original manufacture to maintain accuracy of measurement. Due to the geometry of the V-cone meter, it prevents the collection of any contaminates as flow passes through. The unique geometry of the V-cone also allows for a wide range of beta ratios, with standard beta ratios ranging from 0.45 to 0.75. V-cone meters with values of beta ratios less than 0.45 are not normally manufactured while beta ratios larger than 0.75 requires calibration. The V-cone meter is installed such that the V-cone centreline is concentric to the centreline of the pipe section (ISO 5167-5, 2016).

There are two types of V-cone meter primary elements: the precision tube V-cone meter range in line sizes from 0.5 to 150 inch (**Figure 2-9**) and the Wafer-cone range from 1 to 6 inch (**Figure 2-10**).

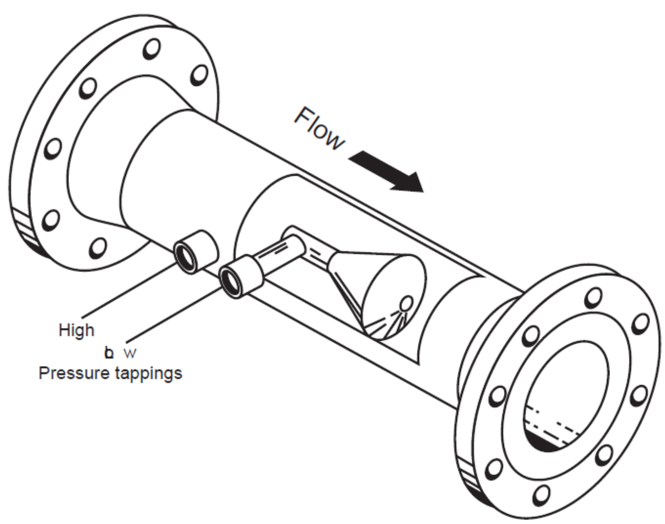

Figure **2-8** McCrometer V-cone Meter (Baker, 2016)

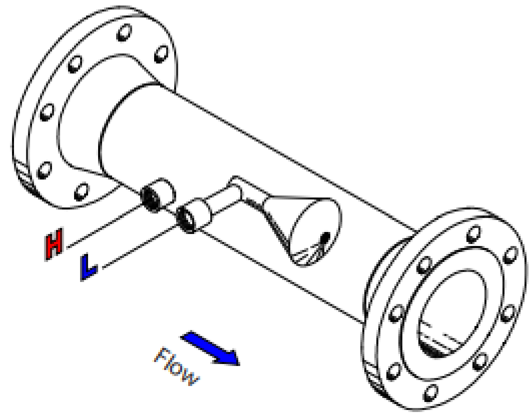

Figure **2-9** McCrometer Precision Tube V-Cone (McCrometer, 2013)

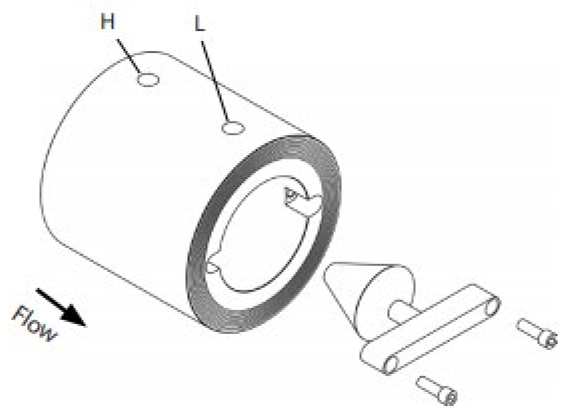

Figure **2-10** McCrometer Wafer-Cone (McCrometer, 2013)

McCrometer is the leading manufacturer for the V-cone meter as their most recent V-cone meter for the oil and gas industry consists of line sizes from 0.5 to 120 inch or larger with standard accuracy of ±0.5%, repeatability of ±0.1% or better, and flow ranges of 10:1 and greater. Their V-cone meter consists of standard beta ratios ranging from 0.45 to 0.85, with custom beta ratios available. The typical materials of the constructed V-cone meter include S304, S316, Duplex 2205 and 2507, Carbon steels, Hastelloy C276, 6Mo with end fittings consist of flanged, threaded, and hub or weld-end standard. It is typically installed zero to three diameters upstream and zero to one diameter downstream of the cone (McCrometer, 2018). As for their Wafer-cone, it can be installed within line sizes from 1 to 6 inch with ±1.0% of accuracy, 0.1% or better for repeatability, and turndown ratio of 10:1. It consists of standard beta ratios ranging from 0.45 to 0.85 and the material of construction is typically 304 or 316 stainless steel. The installation for the Wafer-cone requires one to three diameters upstream and one diameter downstream of the cone (McCrometer, 2013).

2.3.3 Measurement

Flow equations for V-cone flow meter are the actual volume flowrate (**Equation 2-8**) and gas volume flowrate under standard condition (**Equation 2-9**).

$$Q = F_a C_D Y k_1 \sqrt{\frac{\Delta p}{\rho}} \qquad \textbf{(2-8)}$$

$$Q_{STD} = Q \frac{p T_b Z_b}{p_b T Z} \qquad \textbf{(2-9)}$$

where:

Q – Actual volume flow, in cubic feet per hour

Q_{STD} – Standard gas volume flow, in cubic feet per hour

F_a – Material thermal expansion factor

C_d – Meter coefficient

Y – Gas expansion factor

k_1 – Flow constant

Δp – Differential pressure, in psi

ρ – Flowing density, in pounds per cubic feet

p – Operating pressure, in psi

T_b – Base temperature, in degree Rankine

Z_b – Base gas compressibility

p_b – Base pressure, in psia

T – Operating temperature, in degree Rankine

Z – Gas compressibility

2.3.4 Uncertainties

The V-cone meter can be accurate to ±0.5% of reading in an ideal setting, with the level of accuracy dependent to a degree on application parameters and secondary instrumentation. It also exhibits excellent repeatability of 0.1% in terms of repeatability. Another huge advantage for the V-cone meter is the turndown ratio, as the manufacturers claimed to be typically 10:1, which reaches a range far beyond the traditional DP meters. The standard beta ratio ranges from 0.45 through 0.75 and has a relatively low head loss that varies with beta ratio and differences in pressure. The V-cone forms relatively short vortices as the flow passes the cone as these short vortices create a low amplitude, high frequency signal. As compared to other differential pressure meters such as orifice meter, the V-cone has much higher signal stability as shown in **Figure 2-11**.

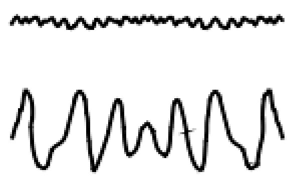

Figure **2-11** DP Meter Signal Stability (McCrometer, 2013)

Due to the design of the V-cone meter, it is effective for wet gas flow measurement applications especially when comparing to orifice meter. The cone shaped design allows the amplitude of oscillation of the measured pressure field to be dampened and directs flow away from the critical edge to decrease corrosion to the meter. Manufacturers claim the V-cone meter to be highly insensitive to velocity profile effects, thus requires a much shorter upstream straight-pipe lengths compare to orifice meter by a factor of up to 9. The recommended installation for the V-cone meter is zero to three pipe diameters of straight run upstream and zero to one pipe diameter downstream. The V-cone meter has been tested in several common configurations and proven to be within accuracy specifications, including close coupled with single 90° elbows or double 90° elbows out-of-plane (McCrometer, 2013).

Szabo et al. (1992) studied the V-cone meter for natural gas flow and compared the flow equations to the standard orifice flow calculation equations. The experiment was conducted using a V-cone meter with 29.376-inch internal diameter and a cone diameter of 27.160-inch and compared to an orifice meter with orifice plate bore diameter of 13.318-inch and meter tube diameter of 29.376-inch, as the two different meter specifications produce the same differential pressure under the same flow conditions. The investigation into the sensitivity of the governing flow rate equations shown that the two meters have the same characteristics and sensitivities to errors in terms of measured input values, including gas composition, temperature, pressure, and differential pressure. For the sensitivity to measured temperature, both meters shown a ±0.10% error in calculated flow rate for ±1.0% error in temperature measurement. For the sensitivity to measured static pressure, both meters resulted in a ±0.06% error in calculated flow rate for a ±0.1% error in static pressure measurement. For sensitivity to measured differential pressure, both meters displayed a ±0.4% error in calculated flow rate for a ±0.1% measurement error in differential pressure measurement.

Singh et al. (2006) conducted experiments using water and oil to cover a wide range of Reynolds number to study the effects of upstream flow disturbances by placing gate valve upstream of the V-cone meter at a distance of five pipe diameter, ten pipe diameter and 15 pipe diameter and at 25%, 50%, 75%, and fully open conditions of the valve. They found that the discharge coefficient is nearly independent of Reynolds number and has a weak dependence on the beta ratio. The discharge coefficient is also unaffected by the upstream disturbance at a distance of ten pipe diameters or more. However, for upstream disturbance less than ten pipe diameters, the maximum change in the discharge coefficient is approximately 6%.

Liu et al. (2015) conducted numerical studies via CFD and experimental studies for verification to examine different beta edges of sharp angle, corner cut, and arc for beta ratios of 0.45, 0.55, and 0.65. The results show that different beta edges cause different changes to the recirculation quantity and the dissipation in the cone wake flow region. From their CFD-simulated data, the corner cut beta edge have the least discharge coefficient linearity error and also the least permanent pressure loss. Their experimental results demonstrate that the sharp angle beta edges have the best mechanical processing consistency while the arc beta edge performed the worst out of the three types.

V-cone meters requires a high Reynolds number to measure correctly. In shale gas production, as gas flow rates drop and Reynolds number decreases with time, measurement could be compromised in late life of a well.

2.4 Orifice Meter

2.4.1 Background Information

Orifice meter is one of the most widely used measuring devices for natural gas flow measurements. The theory orifice meter embodies on is given by Bernoulli's Equation. The name essentially describes the orifice plate itself as a plate with a hole machined into it, which is inserted into a pipe to measure the flowing fluid. As flow passes through, the constriction created by the orifice produces a pressure difference from the upstream to the downstream of the orifice plate. The most common type of orifice meters uses the square-edged concentric plates with flange taps for measuring points. The AGA Report No.3 provides the standard for this type of orifice meter set up with the most readily available flow coefficients from extensive testing and studies.

Most of the early experimental works almost focused exclusively on the determination of discharge coefficients, with modern orifice meter for natural gas measurement dates back to early 1900s. Weymouth (1912) completed and published his experimental studies for orifice meter with a thin plate measured using flange taps. The orifice meter line was also in series with a pitot tube to make a comparison between the two, as availability of any orifice meter data was almost nonexistent as the time. Weymouth compared his study with published studies by Hodgson (1917) from England and had similar results despite the widely separated places and the experiments done independently. After Weymouth's publication, numerous other groups turned their attentions to the studies of orifice meter as the accumulated data and literatures eventually compiled into the first AGA report (1930), which is collected by a joint committee formed by AGA and American Society of Mechanical Engineers (ASME), with the National Bureau of Standards (NBS) for the review of the data. The establishment for the AGA Report No.1 upstarts the research projects on orifice meters, particularly the determination of the absolute values of orifice coefficients, and eventually became the standard guideline for natural gas measurements using orifice meters in America.

Beitler (1935) led the largest single collection of experiments, also known as the Ohio State University (OSU) data base, for the determination of discharge coefficients for orifice meters from 1932 to 1933 sponsored by the industry. The experiments conducted using water flowing through seven pipe diameters ranging from one to 14 inch. The data from the smallest sizes are especially valuable since no data in pipes smaller than 2 inch were taken during the European and API tests. Buckingham (1932) and Bean of NBS develop a mathematical equation to calculate the flow coefficient for orifice meters using the OSU data base. The data base and equation were however, collected with water flows, indicating that any equations based on them require significant extrapolation in Reynolds number when used in high-pressure gas. The high quality of work became the base for all flange-tapped orifice metering standards until 1990.

Stolz (1978) combined the Beitler's data into a single, dimensionless equation applicable for all three pressure taps and adapted by for the international standard in the ISO standard 5167 (1980). This universal equation was eventually fortified using the much more comprehensive data base conducted over a ten-year period at eleven laboratories using four different fluids: oil, water, air, and natural gases, to cover the pipe Reynolds numbers ranging from 100 to 35,000,000. In the United States, Whetstone et al. (1988) conducted experiments with natural gas over the Reynolds number ranging from 25,000 to 16,000,000 to measure the discharge coefficients of orifice for the 6 inch and 10 inch pipe diameters. The two-year collection of data contained 1,345 valid test points over eight beta ratios for the two selected pipe diameters. In 1988, a joint meeting of the United States and European flow measurement experts in New Orleans unanimously accepted the orifice plate discharge coefficient equation derived by the National Engineering Laboratory (NEL), based on the data collection from the past ten years in Europe and United States. Reader-Harris et al. (1990) describes the development of the discharge coefficient equation based on the physics of the orifice meter in their publication, as the equation is divided into tapping term, slope term, upstream and downstream tapping terms. Reader-Harris et al. (1995) further describes the two principal changes to the discharge coefficient equation previously accepted in 1988 based on the expanded collection of the orifice test data including the data collected in 2 inch and 24 inch pipes. The updated discharge coefficient equation includes the improved tapping terms for low Reynolds number and an additional term for small orifice diameter. The empirically derived discharge coefficient equation by the NEL set the standard for the discharge coefficient for both the ISO and the AGA for orifice metering.

The first edition of AGA Report No. 3 (1955) expanded the application conditions for orifice meter as well as setting the standard condition for pressure to 14.73 *psia* from the previous 14.4 *psia*. This report also introduces the formula using factors approach built upon the first law of thermodynamics in order to calculate the volumetric flow rate for the measured gas. The second edition of AGA Report No.3 (1985a). AGA-3 (1985b) expands the compressibility to cover a wider selection of gas composition as well as increasing the pressure up to 20,000 *psi*. The third edition of AGA Report No. 3 (1992) focuses on the flange-tapped orifice meter and provides the updated empirical coefficient of discharge equation for this type of pressure tap. This report also sets the revised standards with the recent extensive database conducted by the international standards that covers the range of beta ratios from 0.05 to 0.75. The report also includes the uncertainty guidelines for calculating uncertainties using the equations. For orifice metering of gas measurements, the AGA-3 (2012) is the standard for natural gas industries in the United States.

The study of the velocity profiles and pressure profiles are essential in order to understand the fluid mechanics of differential pressure meters, particularly orifice meter. Durst and Wang (1988) measured the flow velocities through a 1-inch orifice plate in a 2 inch pipe with Reynolds numbers ranging from 200 to 60,000 using LDV techniques. The experimental results demonstrate a similarity relationship of the maximum value of the Reynolds stress lines that is independent of Reynolds numbers. The experimental results are also compared with Durst and Wang (1989) numerical model using FVM and the agreement between the results justifies the use of this computational approach for this type of orifice plate CFD models.

Morrison and his team from Texas A&M University collected a very substantial amount of data by measuring velocity profiles and pressure profiles in orifice meter. Morrison et al. (1990) measured the flow field data through a 1-inch pipe and 0.5-inch orifice plate with airflow at a Reynolds number of 18,400 using 3-D LDV. DeOtte et al. (1991) measured the flow profile for a 1-inch orifice meter inside a 2-inch pipe operating with airflow at a Reynolds number of 54,700 using a 3-D LDV. Morrison et al. (1992) measured the flow profile for a 1.5-inch orifice meter inside a 2-inch pipe operating with a constant mass flowrate using airflow at a Reynolds number of 91,100. The experiment used a flow-conditioning unit to vary the inlet velocity while holding the mass flowrate constant. The results show the various inlet velocity profiles can affect the actual coefficient discharge significantly, as this variation correlates with the first, second, and third-order moments of momentum. Morrison et al. (1993) measured the flow field inside an orifice flowmeter with a beta ratio of 0.50 for a 2-inch pipe operating at a Reynolds number of 91,000 using a 3-D LDV. This study examined a farther downstream location for the vena contracta and flow reattachment to the pipe wall for this setting. The experiment observed a small upstream recirculation zone and both a primary and secondary recirculation zone downstream of the orifice plate. The study also included the distributions of the entire Reynolds stress tensor and calculated into values of turbulence kinetic energy, turbulence kinetic energy production, vorticity, and turbulence induced accelerations, which further interpret the complex turbulent flow field inside an orifice meter.

These recent experiment studies, particularly the ones led by Morrison and his team, provided more in-depth measurements and studies into a deeper understanding of the fluid mechanics inside a pipe with the presence of different sizes of orifice meters. These studies established the foundations for further experimental works, including various conditions and factors that could affect the accuracy of the orifice measurements. The data also set the framework for numerical studies, such as simulating orifice meter with CFD models, as many of the recent numerical studies verifies their results with the data for from Morrison and his team, including our numerical studies on the orifice meter.

The flow through orifice meters is very difficult to describe mathematically, especially for turbulence gas flows. However, we can gain much insight by inspecting the various flow regimes that occur in an orifice flow to help us further understand flow mechanisms. (Upstream flow regime. Downstream flow regime: vena contracta, recirculation zones, sudden expansion, separate flow, reattach to the wall).

Perhaps the most important characteristic of an orifice meter, or any types of differential pressure flow meter, is the discharge coefficient, C_d, as it provides the ratio of the actual discharge to the theoretical discharge. The C_d is a function of the Reynolds number and can be obtained by calibrating it in a flowing fluid. The extensive studies and research over the past in effort to determine the C_d, as 1% increase/decrease can affect directly to the flow volume by the same percentage. The latest standard, AGA No. 3 (2012), uses the discharge coefficient equation derived empirically by Reader-Harris and Gallagher (RG) determined from a vast collection of laboratory data. Reader-Harris and Gallagher developed this equation based on the understanding of orifice meter physics consists of the tapping term, the slope term consisting of throat Reynolds number term and velocity profile term, and upstream and downstream tapping terms (Reader-Harris, 1990).

2.4.2 Design

By American Petroleum Institute (API) and AGA Standards, the primary element of the orifice meter consists of the orifice plate, the orifice plate holder (with its associated differential pressure sensing taps), and the meter tube as illustrated in **Figure 2-12**. The orifice plate typically is a flat, thin plate consisting of a circular concentric aperture with a sharp, square edge. The orifice plate holder is used to contain and position the orifice plate in the piping system that functions as a pressure-containing piping element. The meter tube is the straight sections of pipe that include all segments that are integral to the orifice plate holder, upstream and downstream of the orifice plate. For Orifice meter to measure within the specified uncertainty, the measuring fluids have to be under steady-state mass flow conditions and considered to be clean, single phase, homogeneous, and Newtonian with pipe Reynolds numbers of 4,000 or greater (AGA-3.1, 2012).

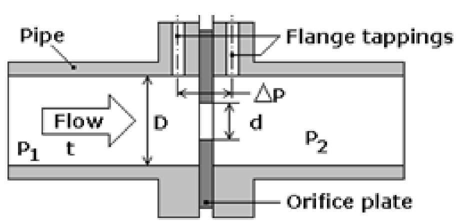

Figure **2-12** Flange-tapped Orifice Meter (AGA 3.1, 2012)

There are different locations for differential-pressure tappings: D and D/2 tapping (radius), pipe tapping ($2\frac{1}{2}$ D and 8D, full-flow), flange tapping, corner tapping, and vena contracta tapping. Vena contracta taps have been replaced by D and D/2 taps since today's taps require no tap relocation as vena contracta taps vary with changes in orifice beta ratio. Pipe taps are sometimes used as bypass pump restrictors for natural gas or where the other tapping arrangements require drilling too close to the plate. Corner and D and D/2 taps are widely used in Europe, while flange taps predominate in the United States for pipe sizes 2 inch and larger. The tappings should be positioned to prevent any unwanted component of the flowing line or any second phase in the flowing line from entering or being trapped in the impulse line. The orifice plate holder should maintain perpendicularly to the meter tube axis for dry gas applications. For moist gases, it should be positioned between angles of 30^{o} above the horizontal and vertically upward to the meter tube axis (Miller, 1996). A pair of flange taps are located 1 inch of the nearest plate face on the upstream side and 1 inch from the nearest plate face on the downstream side, measured from the center of the taps.

In terms of gas flow measurements, it should be designed carefully to accommodate for the changes in operating pressure and temperature since they can alter the gas density significantly during operation. Typically, flow computers are designed to obtain flow from sensors measuring the differential and static pressure, fluid temperature, and fluid density and/or specific gravity by either mechanical recording devices or electronic calculators. Although these secondary devices are not included within the scope of the API/AGA standards, they are essential for the precision in determining the flow rate of the measured gas flow.

At the pressure tap, the differential pressure element and the static pressure element can measure and record the pressures of the flowing gas. The differential pressure element measures and records Δp, Δp_{avg}, Δp_{rms}, Δp_t, while the static pressure element measures and records p_f (can also be measured with absolute static pressure = gauge static pressure + local barometric pressure). The temperature element is installed in the flowing stream designated on the upstream or downstream location to measure and record T_f. If the fluid velocity is higher than 25% of the fluid sound speed at the measuring point, corrections for the increase in temperature due to dynamic effects will have to be applied. The thermometer well is installed on the downstream side in between the dimension range of DL and 4DL to sense the average temperature of the fluid at the orifice plate (AGA-3.2, 2003).

Daniel orifice plates can be installed within line sizes ranging from 0.25 to 24 inch while having a discharge coefficient uncertainty of ±0.5 to 0.75% with a 10:1 or better turndown ratio. Their plates are typically constructed with 316/316L stainless steel with plate thickness ranging from 0.125 to 0.5 inch. The bore type of the plates includes concentric bore (bevel or no bevel), bore and counter bore, segmental, eccentric, quadrant round, and blank. Their standard for plate finish is typically less than 30 micro-inch of roughness (Emerson, 2017).

Rosemount 3051SFC compact orifice flow meter can be installed within line sizes ranging from 0.5 to 12 inch with an accuracy of ±1.30% of flow rate at 14:1 turndown ratio or ±1.45% of flow rate at 8:1 turndown ratio. Rosemount 1495 orifice plates are configured as square-edged concentric bore and can be installed within line sizes ranging from 2 to 24 inch. Their plates are typically constructed with 316/316L stainless steel or 304/304L stainless steel and with plate thickness ranging from 0.125 to 0.5 inch (Emerson, 2021a).

2.4.3 Measurement

Gas flow volume can be calculated using the most recent and updated gas flow rate equation for flange-tapped Orifice meter published by AGA in 2012 below in field units (AGA 3.3, 2012), Nomenclature is available in **Table 2-1**.

$$Q_v = C'\sqrt{h_w p_{f1}} \quad \textbf{(2-10)}$$

where

$$C' = F_n(F_c + F_{sl})Y_1 F_{pb} F_{tb} F_{tf} F_{gr} F_{pv} \quad \textbf{(2-11)}$$

- F_n is the numeric conversion factor that combines the numeric element of the volumetric flow equation, which can be calculated through **Equation 2-12**, where E_v is the velocity of approach factor calculated through **Equation 2-13**.

$$F_n = 338.196 E_v D^2 \beta^2 \quad \textbf{(2-12)}$$

$$E_v = 1/(1-\beta^4)^{0.5} \quad \textbf{(2-13)}$$

- F_c is the orifice calculation factor. The modification of the previous orifice meter coefficient discharge, C_d, which is determined empirically from test data, is now the sum of F_c and F_{sl}. F_c can be calculated through **Equation 2-14**. But if meter tubes internal diameter is less than 2.8 inch, **Equation 2-15** should be used to correct F_c.

$$F_c = 0.5961 + 0.0291\beta^2 - 0.2290\beta^8 + \big(0.0433 + 0.0712e^{-8.5/D} - 0.1145e^{-6.0/D}\big)\left[1 - 0.23\left(\frac{19{,}000\beta}{Re_D}\right)^{0.8}\right]\frac{\beta^4}{1-\beta^4} - 0.0116\left[\frac{2}{D(1-\beta)} - 0.52\left(\frac{2}{D(1-\beta)}\right)^{1.3}\right]\beta^{1.1}\left[1 - 0.14\left(\frac{19{,}000\beta}{Re_D}\right)^{0.8}\right] \quad \textbf{(2-14)}$$

$$F_c = F_{c,old} + 0.003(1-\beta)(2.8 - D) \quad \textbf{(2-15)}$$

- F_{sl} is the orifice slope factor. It is the slope term from the coefficient of discharge equation and is a function of Re_D and β. For most natural gases, Re_D can be estimated using **Equation 2-16**, which is a function of Q_v, D, and G_r. Since Re_D is a function of Q_v, it can only be obtained through iteration. Typically, three iterations of Q_v and Re_D are required to provide an accurate solution for Re_D. After obtaining the value for Re_D, the orifice slope factor can be calculated using **Equation 2-17**.

$$Re_D = 47.0723\frac{Q_v G_r}{D} \quad \textbf{(2-16)}$$

$$F_{sl} = 0.000511\left(\frac{1{,}000{,}000\beta}{Re_D}\right)^{0.7} + \left[0.0210 + 0.0049\left(\frac{19{,}000\beta}{Re_D}\right)^{0.8}\right]\beta^4\left(\frac{1{,}000{,}000\beta}{Re_D}\right)^{0.35} \quad \textbf{(2-17)}$$

- Y_1 is the expansion factor referenced to upstream pressure. It depends on the expansion of gas through the orifice. The expansion factor corrects for the variation in density since the density of the stream changes due to the pressure drop and the adiabatic temperature change. It is a function of *the differential pressure, the absolute pressure, the diameter of the pipe, the diameter of the orifice, and the type of taps, and the isentropic exponent.* Typically for natural gas applications, the perfect gas isentropic exponent, k_p, is used as k_p=k=1.3. For the calculation of Y_1,

Equation 2-19 can be used to calculate Y_1 as long as the criterion for **Equation 2-18** is valid. If upstream static pressure is measured to calculate volumetric flow, **Equation 2-20** is used to calculate the ratio of differential pressure to absolute static pressure, x_1. The ratio of x_1 and k is also known as the *acoustic ratio*.

$$0 < \frac{h_w}{27.707 p_f} \leq 0.20 \quad \textbf{(2-18)}$$

$$Y_1 = 1 - (0.41 + 0.35\beta^4)\left(\frac{x_1}{k}\right) \quad \textbf{(2-19)}$$

$$x_1 = \frac{h_w}{27.707 p_{f_1}} \quad \textbf{(2-20)}$$

- F_{pb} is the base pressure factor which is a direct application of Boyle's law in order to calculate the difference in base pressure, p_b, from 14.73 *psia*.

$$F_{pb} = \frac{14.73}{p_b} \quad \textbf{(2-21)}$$

- F_{tb} is the base temperature factor which is a direct application of Charles's law in order to calculate the difference in base temperature change.

$$F_{tb} = \frac{T_b}{519.67} \quad \textbf{(2-22)}$$

- F_{tf} is the flowing temperature factor which is used to correct the effects of temperature variation. Higher flowing temperature implies a lighter gas which led to increases in flow, but it also causes the gas to expand, which reduces the flow. The flowing temperature factor is usually applied to the average temperature during the time gas is passing through.

$$F_{tf} = \sqrt{\frac{519.67}{T_f}} \quad \textbf{(2-23)}$$

- F_{gr} is the real gas relative density factor which is used to correct for changes in the specific gravity based on the actual flowing specific gravity of the gas, which is updated constantly by a recording gravitometer or by gravity balance. Since the basic orifice factor is determined by air with a specific gravity of 1, it is expressed as:

$$F_{gr} = \sqrt{\frac{1}{G_r}} \quad \textbf{(2-24)}$$

- F_{pv} is the supercompressibility factor which is used to correct for the fact that gas does not behave exactly as the ideal gas law stated, but all gases do deviate from this ideal gas law to a greater or lesser extent. The term supercompressibility accounts for the deviation between the actual density of a gas under high pressure and the theoretical density obtained by the base conditions. z_b is the gas compressibility at the base conditions, z_f is the gas compressibility at operating/flowing conditions.

$$F_{pv} = \sqrt{\frac{z_b}{z_{f1}}} \quad \textbf{(2-25)}$$

- Typically, the gas volume is calculated through measured data of *differential pressure*, *daily average pressure, flowing temperature*, and *flow hours*, along with the provided *gas composition*, *orifice plate size*, and the *pipe size*. The differential pressure data is the input for h_w and the daily average pressure data is the input for p_{f1} in **Equation 2-10**. For a more precise calculation, the orifice plate bore diameter (**Equation 2-26**) and the meter tube internal diameter (**Equation 2-27**) should be calibrated with the flowing temperature data used as T_f. The reference temperature,

T_r, per AGA standard is assumed to be at 68°F. The linear coefficient of thermal expansion, α_1 and α_2, can found through ASME database for -100°F to +300°F or API database for -7°F to 154°F. For our cases, we typically use orifice plate and pipe constructed materials of type 304 and 316 stainless steels with α value of 0.00000925.

$$d = d_r\left[1 + \alpha_1\left(T_f - T_r\right)\right] \quad \textbf{(2-26)}$$

$$D = D_r\left[1 + \alpha_2\left(T_f - T_r\right)\right] \quad \textbf{(2-27)}$$

The new calculation does not require readings from AGA's published tables to obtain factor/coefficients in **Equation 2-11**. The factors are calculated through the measured parameters as well as gas properties, including specific gravity and Z-factor. The ideal gas specific gravity, G_i, is calculated as the ratio of the molecular weight of the measured gas, Mr_{gas}, to the molecular weight of the air, Mr_{air}, in **Equation 2-28**, with Mr_{air}=28.9625 pounds mass per pound-mole. The real gas specific gravity, G_r, is calculated through **Equation 2-29**, with the Z-factor for air at base conditions, Z_{bair}=0.999590.

$$G_i = \frac{Mr_{gas}}{Mr_{air}} \quad \textbf{(2-28)}$$

$$G_r = G_r \frac{Z_{b_{air}}}{Z_{b_{gas}}} \quad \textbf{(2-29)}$$

The Z-factor for gas is calculated through the equation of state fitted by Dranchuk and Kassem (1975), as their method is more convenient for estimating the z-factor for gas with computer programs. For orifice metering of natural gases, we are typically dealing with low temperature conditions, hence the bisection method is applied to estimate the Z-factor through iterations instead of using the Newton-Raphson method, as the latter becomes unstable and perform slower at low temperature conditions.

The discharge coefficient for orifice meter, C_d, has been correlated from test data as a function of diameter ratio, meter tube diameter, and pipe Reynolds number. For a concentric, square-edged flange-tapped orifice meter, $C_d(FT)$ can be calculated as the sum of the orifice calculation factor, F_c, and the orifice slope factor, F_{sl}, as shown in **Equation 2-30** using the factors approach. The equation is applicable to nominal pipe sizes of 2 inch and larger while within the beta ratio range of 0.1 to 0.75, provided that the orifice plate bore diameter is greater than 0.45 inch, and also a pipe Reynolds number greater than or equal to 4000. For meter tube with internal tube diameter less than 2.8 inch, F_c should be modified accordingly as shown in **Equation 2-15**. For typical operating gas flow range, the pipe Reynolds numbers exceeds the requirement in orders of magnitude.

$$C_d(FT) = F_c + F_{sl} \tag{2-30}$$

The discharge coefficient can also be calculated with the RG equation as follows:

$$C_d(FT) = C_i(FT) + 0.000511\left(\frac{10^6\beta}{Re_D}\right)^{0.7} + (0.0210 + 0.0049A)\beta^4 C \tag{2-31}$$

$$C_i(FT) = C_i(CT) + Tap\ Term \tag{2-32}$$

$$C_i(CT) = 0.5961 + 0.0291\beta^2 - 0.2290\beta^8 + 0.003(1-\beta)M_1 \tag{2-33}$$

$$Tap\ Term = Upstrm + Dnstrm \tag{2-34}$$

$$Upstrm = [0.0433 + 0.0712e^{-8.5L_1} - 0.1145e^{-6.0L_1}](1 - 0.23A)B \tag{2-35}$$

$$Dnstrm = -0.0116[M_2 - 0.52M_2^{1.3}]\beta^{1.1}(1 - 0.14A) \tag{2-36}$$

where,

$$B = \frac{\beta^4}{1-\beta^4} \tag{2-37}$$

$$M_1 = max\left(2.8 - \frac{D}{N_4}, 0.0\right) \tag{2-38}$$

$$M_2 = \frac{2L_2}{1-\beta} \quad \textbf{(2-39)}$$

$$A = \left(\frac{19{,}000\beta}{Re_D}\right)^{0.8} \quad \textbf{(2-40)}$$

$$C = \left(\frac{10^6}{Re_D}\right)^{0.35} \quad \textbf{(2-41)}$$

The computer codes we have developed allow pipe Reynolds number to be updated simultaneously based on flow data and plate sizes that provides calculations that are more precise. The discharge coefficients for the Reynolds number iterations are calculated using **Equation 2-31** through **Equation 2-32**, as the factor approach is not feasible for the iterating.

Table **2-1** Nomenclature in the gas volume calculation (AGA 3.3, 1992)

Symbol	Description
C'	composite orifice flow factor
$C_d(FT)$	coefficient of discharge at a specific pipe Reynolds number for a flange-tapped orifice meter
$C_i(CT)$	coefficient of discharge at an infinite pipe Reynolds number for a corner-tapped orifice meter
$C_i(FT)$	coefficient of discharge at an infinite pipe Reynolds number for a flange-tapped orifice meter
D	meter tube internal diameter calculated at flowing temperature (T_f), in inch
D_r	reference meter tube internal diameter calculated at reference temperature (T_r), in inch
d	orifice plate bore diameter calculated at flowing temperature (T_f), in inch
d_r	reference orifice plate bore diameter calculated at reference temperature (T_r), in inch
e	Napierian constant, 2.71828
E_v	velocity of approach factor
F_c	orifice calculation factor
F_{gr}	real gas relative density factor
F_n	numeric conversion factor
F_{pb}	base pressure factor
F_{pv}	supercompressibility factor

F_{sl}	orifice slope factor[1]
F_{tb}	base temperature factor
F_{tf}	flowing temperature factor
G_i	ideal gas relative density (specific gravity)
G_r	real gas relative density (specific gravity)
h_w	orifice differential pressure, in inch of water at 60°F
k	isentropic exponent
k_p	perfect gas isentropic exponent
L_1, L_2	L_1=L_2, dimensionless correction for tap location, N_4/D for flange taps
Mr_{air}	molecular weight of air, in pounds mass per pound-mole
Mr_{gas}	molecular weight of gas, in pounds mass per pound-mole
N_4	1.0 when D is in inch
P_b	base pressure, in pounds force per square inch absolute
p_{f1}	absolute flowing pressure (upstream tap), in pounds force per square inch absolute
Q_v	volume flow rate at standard conditions of Z_b, T_b, and P_b, in cubic feet per hour
Re_D	pipe Reynolds number
T_b	base temperature, in degrees Rankine
T_f	absolute flowing temperature, in degrees Rankine
Tr	reference temperature of the orifice plate bore diameter and/or meter tube inside diameter, in degrees Fahrenheit
Y_1	expansion factor based on upstream absolute static pressure
Z_b	compressibility at base conditions (P_b, T_b)
Z_{f1}	compressibility at upstream flowing conditions (P_{f1}, T_f)
α_1	linear coefficient of thermal expansion of the orifice plate material, in inch/inch-°F
α_2	linear coefficient of thermal expansion of the meter tube material, in inch/inch-°F
β	ratio of orifice plate bore diameter to meter tube internal diameter (d/D) calculated at flowing temperature (T_f)
μ	absolute viscosity of flowing fluid, in pound mass per feet-second

2.4.4 Uncertainties

Orifice meter is typically simple, inexpensive, consisting of no moving parts, mechanically stable, and has no limitation on temperature, pressure, or size. Orifice meters for gas measurement are considered to be accurate to ±1 to ±2%, accuracies better than ±1% can be achieved by individual calibration. However, it tends to have relative low accuracy when measuring at low flow conditions. The turndown for this design typically is less than 5:1, which is a relatively low range compared to other meters. It also has high-pressure loss (15-55%) which can impact operating cost. Orifice meter is also flow-profile sensitive and usually requires a long meter tube or flow conditioner and it is not capable of self-cleaning thus can be easily damaged or clogged by high flow rates.

The AGA-3 equation and the Reader-Harris/Gallagher equation were developed implicitly assumes that the velocity profile in the upstream of the orifice is fully developed, symmetric, swirl-free, and turbulent for the orifice meter to measure accurately. However, this is not always the case for the field measurement as different factors can affect the flow profile and the “pureness” of the flowing gas, which could possibly affect the accuracy of the orifice measurement. Extensive studies on different factors are reviewed in each of the sub sections as how each factor affect the measurement accuracy.

Installation Effects

The orifice coefficient equations were developed assuming the upstream axial velocity profile is “fully developed” as it implies that the discharge coefficient would not change if the meter tube were lengthened further. However, standard pipefittings such as tees, elbows, and valves from the upstream of the pipe can introduce velocity profile distortion and increase turbulence levels with significant swirl velocity component. The effect of a peaked velocity profile increases the discharge coefficient whereas a flattened profile will reduce the discharge coefficient. An asymmetric flow will reduce the discharge coefficient since it would require more energy to move an asymmetric flow through the orifice than a symmetrical flow. The effect of swirl increases the discharge coefficient as it would increase the diameter of the *vena contracta*.

Morrow et al. (1991) performed experimental studies to measure the upstream velocity profiles for a 45D, four-inch diameter meter tube using nitrogen flow at a Reynolds number of 9×10^5 with orifice plate in beta ratios of 0.40 and 0.75. The measured velocity profiles were compared to the power law velocity profile model and the modified logarithmic velocity profile model. The results show that the flow is still far from fully developed in a length of 45D as a greater meter tube length or flow conditioners may be needed.

Morrison et al. (1992) investigated the effect of the inlet velocity distribution upon the discharge coefficient in a two inch pipe with beta ratio of 0.75 using airflow at a Reynolds number of 91,000. The velocity profiles obtained are compared with the profiles measured using a laser Doppler velocimeter. The experimental study shows that the upstream velocity profile can affect the discharge coefficient significantly and the changes in discharge coefficient is correlated with the first, second, and third-order moments of momentum.

Swirl

Like most of the flow meters, orifice meter is affected by how and where it is installed. Orifice meters need to be calibrated according to the AGA 3.2 guidelines to give a predictable performance when installed where the flow profile approximates to a fully developed flow profile at the Reynolds number of the flow. A fully developed turbulent velocity profile is symmetric around the pipe axis with maximum fluid velocity at the axial centerline of the pipe. The Reader-Harris/Gallagher (RG) equation used to develop the discharge coefficient implicitly assumes that the velocity profile is fully developed, symmetric, swirl-free, and turbulent. Installation effects may disturb the flow profile that could lead to a change in the metering performance and the effect of upstream fittings and pipework is considered in terms of peakiness of profile, asymmetry, and swirl (Reader-Harris, 2015). The effect of a peaked profile, for example, to a roughened pipe, is to reduce the pressure drop for a given flowrate and thus increase the discharge coefficient. On the contrary, the effect of a flattened profile will reduce the discharge coefficient. An asymmetric flow reduces the discharge coefficient since more energy is required to move an asymmetric flow through the orifice as compared to the same flow flowing symmetrically. The effect of swirl is more complex as it is almost always accompanied by a change in axial velocity profile. The velocity profile from the swirl effect is flattened and typically asymmetric which reduces the discharge coefficient and under measures the flowrates.

A flow conditioner may be used to improve the velocity profile from the effect of swirl. According to AGA 3.2, flow conditioners can be classified into straighteners or isolating flow conditioners. Flow straighteners are devices that effectively remove or reduce the swirl component of a flowing stream but may have limited ability to produce the flow conditions necessary to accurately replicate the discharge coefficient values. Isolating flow conditioners are devices that effectively remove the swirl component from the flowing stream while redistributing the stream to produce the flow conditions that accurately replicate the discharge coefficient (AGA 3.2, 2012).

Shen (1991) investigated effects of swirl on the measurement accuracy of a 6-inch orifice meter with airflow using an axial vane-type swirler. Shen conducted experiments separately for the velocity profile and orifice meter performance with swirl angle ranging from −30° to +30°. The results showed the swirling flows can cause an up to 5% under-measurement on orifice metering accuracy, whereas beta ratio and flow rate have much less effects on the meter's performance. The swirl also flattens the axial velocity profiles compared to the power-law profile for turbulent flow in smooth pipes. The study included the test of the tube bundle conditioner as well, which can significantly reduce the effects of the swirl and to some extent cause the orifice meter to over-measure the true flow rate slightly. Reader-Harris (1994) studied the decay of swirl in a pipe through extensive mathematical equations based on the approximation to the Navier-Stokes equations. He simplifies the Navier-Stokes equations by introducing an order-of-magnitude analysis and a turbulent viscosity to solve the swirl equation. After verifying with experimental data, the study concludes the swirl will be extremely persistent in smooth pipes at high Reynolds number, but flow straighteners are recommended for the measurement accuracy of orifice meter. Morrison et al. (1995) studied the effect of a concentric tube flow conditioner and a vane-type swirl generator for different orifice plate sizes with beta ratios of 0.43, 0.45, 0.484, 0.55, 0.6, 0.65, 0.7, and 0.726 in a 2-inch pipe with Reynolds number of 91,100 and 120,000. The data provides optimal orifice beta ratios for installation in cases that swirl effect is expected to dominate the flow.

Flow Conditioner

Upstream disturbances can be reduced through flow straighteners and/or flow conditioners. Flow straighteners eliminate swirl from the inlet flow but has little or no effect on the upstream velocity profiles. They are only effective for orifice plate with small beta ratio. Typical flow straighteners are installed in the forms of tube bundles. Flow conditioners, on the other hand, not only eliminate swirl but also produces a repeatable downstream velocity profile, regardless of upstream flow disturbances.

Ouazzane and Behnhadj (2002) studied two flow conditioners for orifice meter, vaned-plate flow conditioner (**Figure 2-13**) and NEL-plate flow conditioner. For vaned-plate, orifice meter performance improves at high operating Reynolds numbers regardless of the beta ratio and the severity of the distortions in the upstream flow. For NEL-plate, the errors at low and moderate Reynolds numbers were stills significant and inefficient in short installations.

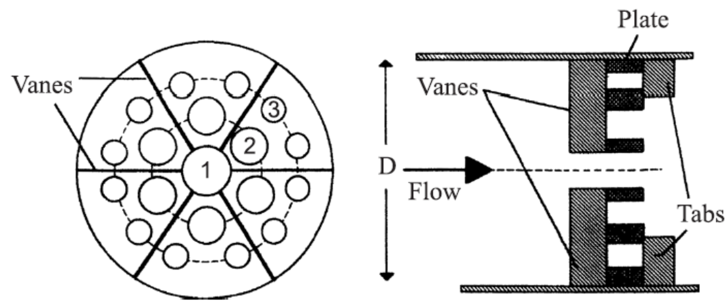

Figure **2-13** Vaned-plate flow conditioner (Ouazzane, 2012)

Chemical and Organic Contamination

The flowing fluids, such as oil, grease, pipeline sludge or other liquids or solids, can contaminate orifice plates. The accumulation of such contaminates can also build up flow restrictions inside the pipe and on the orifice plate, which would create additional pressure drop for the flowing fluid. One of the common contamination related problems is black powder, which is made up of various corrosive materials in forms of iron sulfide, iron oxide, hydrocarbons, and asphalt components.

Tsochatzidis (2008) performed experimental analysis of the black powder to study its effect on gas metering equipment. The black powder he collected consists of about 80% corrosion products while the rest is made up of typical soil minerals. From the examination of the orifice plate, he found a thick layer of black powder mixing with oil or grease on the upstream face of orifice plates from the Sirdirokastro border metering station. Contamination of black powder was found in other instruments and installations as well, including pressure measurements, water dewpoint analyzer, gas chromatographs, specific gravity meters, and online densitometers. The effect of black powder causes these instruments to deviate beyond acceptable tolerance of the standards and cause permanent damage to the instruments as well as the installations. Black powder contamination was also present for the inner pipe wall and decreased the pipe roughness by smoothing the rougher surfaces. In another study by Trifilieff and Wines (2009), they found the opposite as black powder increases the interior pipe wall surface roughness, and to some extents, the accumulation of the black powder to a sufficient level creates a flow restriction for the path. For either case, the changes in pipe wall roughness affect the discharge coefficient and alters the velocity profiles for the flowing fluids, thus increases the uncertainty in orifice measurements.

Reader-Harris et al. (2012) conducted experimental work in conjunction with CFD simulations to examine the effects of contamination on the orifice plate from the upstream side. His laboratory works and CFD models included orifice plates with beta ratios of 0.2, 0.4, 0.6, and 0.75 with pipe diameter of 11.81-inch, with 35 simulation runs at a pipe Reynolds number of 10^7 and three runs at a pipe Reynolds number of 10^6 using nitrogen gas as the flowing fluid. The CFD models overall are in remarkably good agreement with the experimental results. The contamination layer was simulated on the upstream face of the orifice plate using uniform layer with thickness h and an angle θ created by the distance from the plate edge r, as shown in **Figure 2-14**. The contamination layer increased the size of the vena contracta and reduce the pressure difference across the plate and increase the discharge coefficient as compared to the results simulated from a clean orifice plate. To analyze how each contamination layer parameters can affect the discharge coefficient, he also performed parametric studies using parameters h and r for different beta ratios. The results showed the thickness of the contamination layer *h* have a much larger impact on the discharge coefficient than the radius of the contamination layer *r*.

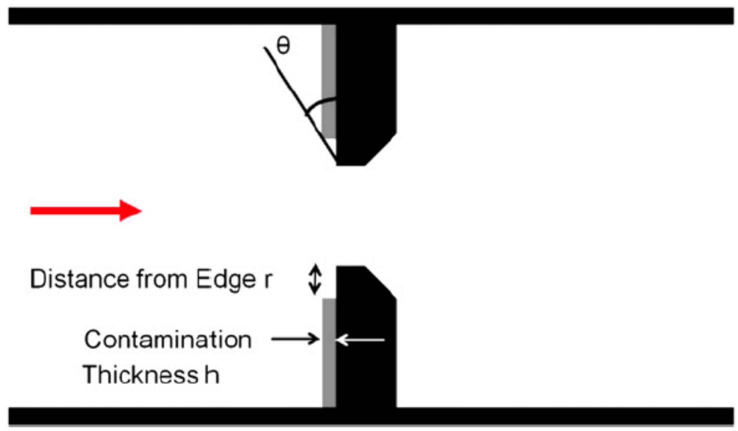

Figure **2-14** Geometry used in Orifice Contamination Simulations (Reader-Harris, 2012)

Li et al. (2013) studied the effect of sludge deposition on orifice metering accuracy through CFD simulations for a 2-inch pipe with beta ratio of 0.75 using water as the flowing fluid. The sludge deposition, shown in **Figure 2-15**, were simulated with inlet velocities of 4.0, 8.0, 12.0, 16.0, and 20.0 m/s using degrees of 0.1 to 1.0 and verified with experimental results using deposition degrees of 0.25, 0.5, 0.75, and 1.0, as deposition degree, Y_u, is defined as $h/[0.5(D\text{-}d)]$, with *h* as the deposition height. Simulation results show that the deposition affects the downstream pressure significantly and causes an increase in terms of discharge coefficients of the orifice. The changes in discharge coefficients also increases with higher degrees of depositions. Their models provide a method for further CFD studies for deposition effects on orifice meter, which can be related to similar effects such as contamination, wear conditions, and etc. Their studies also provide us insights on how to perform discharge coefficient calculations for CFD models based on AGA standards.

However, since their models are based on water as the flowing fluid with beta ratio of only 0.75, we should establish our CFD models using gas (air) as the flowing fluid with a more reasonable beta ratio, preferably a beta ratio of 0.50 before we develop further into this type of models.

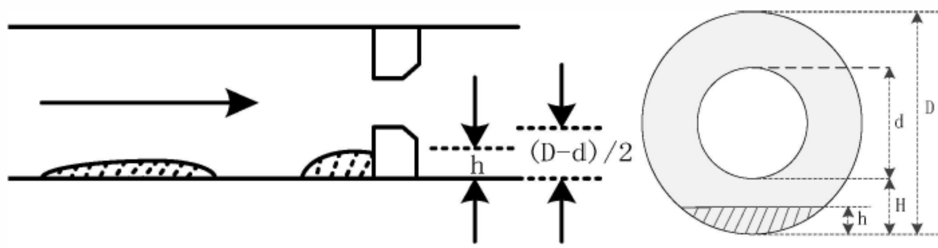

Figure **2-15** Schematic of the Orifice Plate Deposition (Li et al., 2013)

Physical Deformation

Benedict et al. (1975) investigated the effect of edge sharpness on the discharge coefficient of an orifice plate through experimental studies. The edge roundness of the orifice plates are measured based on the optical method, which uses the projection from a fine beam of light directed at the orifice edge in conjunction with a geometric equation to determine radius of curvature of the orifice edge. The roundness measurements are in good agreement compared with the lead foil method measurements provided by Daniel Industries, Inc. The experiments are conducted using five random orifice plates, significantly different in terms of measured edge sharpness, set up in a 4 inch pipe to measure the discharge coefficients. By comparing the results from Crockett et al. (1972) and Brian et al. (1973) with their similar experimental studies, the edge sharpness of the upstream face of an orifice plate has a significant effect on the discharge coefficient of an orifice meter; this effect can be quantified especially with further studies and data collections.

Jepson and Chipchase (1975) investigated into the effect of plate buckling on orifice meter accuracy through experimental studies (**Figure 2-16**). The orifice plate will always experience elastic deformation during operation, as the measuring fluids are flowing with high velocities that generate deflections on the plate. The experiments were conducted using orifice plates with beta ratios of 0.2 and 0.7 through an 8-inch pipe, with bore deflections of 0, 1/32, 1/16, 1/8, ¼, 3/8, and ½ inch relative to the support using natural gas as the testing fluid. The tangential stress generated from the buckling effect causes a decrease in the orifice bore diameter, thus result in a flow over-estimation. However, the coefficient of contraction will increase due to the elastic deformation, which results a drop in the differential pressure and an under-registration in flow. These two opposite effects will partially cancel each other and causes an under-measurement of the flow; the flow measurement error due to elastic defection can be quantified in terms of geometry and the mechanical properties of the buckled orifice plate. Norman et al. (1984) further investigated into elastic deformation of the orifice plate through static loading test to verify their theoretical developed equation describing the under-registration of the flow. They also found that orifice plate exhibits a non-linear relationship between deflection and load, whereas the flow error equation is based on a linear elastic theory. However, the change in slope of the orifice plate deflection and the flow error follow a linear relationship, thus eliminates the need to know the modulus of elasticity of the plate material as the error can be directly related to deformation.

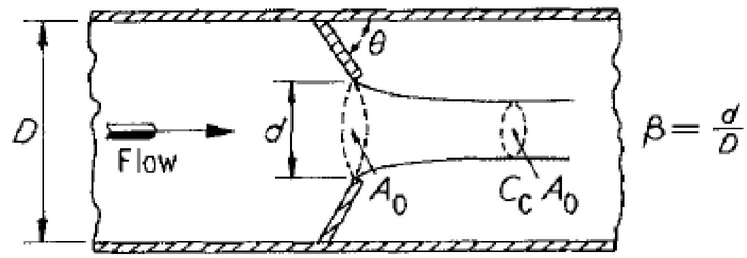

Figure **2-16** Effect of Orifice-Plate Buckling on the Coefficient of Contraction (Jepson, 1975)

Norman et al. (1984) also studied the effects of plate eccentricity through a 5.9-inch pipe using beta ratios of 0.2, 0.37, 0.57, 0.66, and 0.75 for D+D/2 and flanged tapped orifice meters using air with Reynolds number ranging from 22,000 to 200,000. The eccentricity tests were conducted for both away from and toward the upstream tap. The experimental results show the eccentricity of the plate cause an increase in the discharge coefficient, with beta ratio of 0.2 to be quite insensitive to the effect. While comparing their results with the ISO 5167 standards for eccentricity effect, they suggested that there is substantial scope for relaxing the eccentricity limit from the standards to the benefit of users without substantially increasing uncertainty of discharge. They also suggested locating taps in perpendicular with the expected direction of maximum eccentricity to minimize the effect of eccentricity for orifice metering accuracy.

Nemitallah et al. (2014) performed CFD simulations to study the effect of solid particle erosion on the downstream of an orifice using 2% solid particle concentration with water as the particle carrying fluid for carbon steel and aluminum pipes. The rate of erosion and the erosion pattern for the downstream of orifice plate due to the solid particles are investigated through the effect of flow velocity and sand particle size. The mathematical models are based on the solution of the conservations of mass and momentum using realizable turbulence model while the particle trajectories are tracked using a Lagrangian particle-tracking model. The results display two erosion peaks in the downstream side of the orifice plat with the first peak occurs in the separation zone right after the vena contracta and the second peak forming in the reattachment region. Increase in the inlet flow velocity will cause an increase in the total erosion rate whereas an increase in particle size would result in a decrease of the total erosion rate.

2.4.5 Parametric Studies

Sheikholeslami et al. (1988) studied the variations in discharge coefficient as results of variation in beta ratio, Reynolds number, upstream and downstream boundary conditions, pipe surface roughness, and upstream swirl. Reynolds number of $4x10^4$, $4x10^5$, $4x10^6$, $4x10^7$, and $4x10^8$ are studied for beta ratios of 0.4 and 0.75 by changing the fluid properties. The numerical results are all within 2% of the empirical values from the standards and shown smaller variations for the changes in discharge coefficient. The results displayed similar trends as discharge coefficients increase with decreasing Reynolds number. Beta ratios of 0.4, 0.6 and 0.75 are studied for the effect of beta ratio at Reynolds number of $4x10^4$ and $4x10^6$. The overall trends for the variation of the discharge coefficients with beta ratio followed well with the empirical data. The effect for pipe surface roughness is less than 0.7% of maximum increase for the discharge coefficient for roughness heights up to 500 μm. The effect of upstream and downstream boundary conditions is studied with partially open valve, reducer, and expander for beta ratio of 0.4

with Reynolds number of $4x10^6$. The effect of downstream boundary condition is insignificant to the discharge coefficient from the model while the upstream flowing boundary conditions can affect the discharge coefficient significantly. Shan et al. (2016) studied the effects of the beta ratio on the flow field employing a planar particle image velocimetry measuring technique. The experiment was conducted through a 1.811 *inch* pipe for beta ratios of 0.41, 0.5, and 0.62 with a Reynolds number of 25,000. The experiment results display a slight beta ratio dependence for the location of the vena contracta. The effect of beta ratios is insignificant for the lengths of the primary and secondary recirculation regions. However, as flow progress downstream, the wall effects showed strong beta ratios as shear layer develop.

We also compared with the experimental data from the National Institute of Standards and Technology (Whetstone, 1988) for the validation of the codes. For the 6 inch meter tube inner diameter, we validated over the beta ratios of 0.20618, 0.37125, and 0.57724; for the 10 *inch* meter tube inner diameter, we validated over the beta ratios of 0.37405, 0.49876, and 0.57373. For the 116 cases we have validated, the flowrates for all of the cases are within 1% of the experimental data using the reference gas composition.

To perform the sensitivity analysis for the gas volume and coefficients to the measuring parameters of the Orifice meter, the following base case presented in **Table 2-2** are used to perform the calculations with the codes we have developed based on the gas volume calculation equations.

Table 2-**2** Data for Base Case (100712472)

Differential Pressure in inch of Water (inch)	144.36
Flowing Pressure (psia)	1197.03
Flow Temperature (°F)	68.31
Flow Hours (hr)	24
Meter Tube Internal Diameter (inch)	4.026
Orifice Plate Bore Diameter (inch)	2
Real Gas Relative Density	0.5701
Gas Density (lb_m/ft^3)	4.0882
Gas Density (lb_m/gal)	0.5465
Gas Viscosity (cp)	0.0132
Reynolds Number	3136516.29
Gas Volume (Mcf/hr)	496.43
Gas Volume (Mcf/Day)	11914.37

For the parameters of differential pressure, flowing pressure, flowing temperature, the study is conducted by keeping the other parameters constant while running the calculations through the studied parameter from -100% to +100% of the base case. For the other parameters, similar approach is conducted but the ranges are limited due to the physicality of the orifice meter setup and other factors.

After the calculations over the selected range for each of the parameters, **Table 2-3** provides an overview of how each metering parameter affects the gas volume calculations. An arrow ↑ indicates that gas volume is larger with the increased metering parameter, for example that a higher than actual flowing pressure p_{fl} measured/reported at the meter would results into a larger than actual gas volume. For parameter flow hours, it follows strictly a linear relationship with gas volume, but flow hours should be recorded precisely as it can cause significant inaccuracy if not recorded correctly. **Table 2-4** provides an overview how each of the coefficients is affected by metering parameter(s).

An arrow ↑ indicates that a coefficient is larger with the increased metering parameter, for example that a higher than actual flowing pressure P_{f1} measured/reported at the meter would results into a larger than actual expansion factor Y_1. In terms of volume calculations, the numeric conversion factor has a significant impact, which is affected by the orifice plate bore diameter and the meter tube internal diameter.

Table 2-**3** Relationship of Metering Parameters and Gas Volume

Metering Parameters	**Gas Volume Calculation, Q_v**
Differential pressure, h_w, inch	↑
Flowing pressure, p_{f1}, psia	↑
Orifice plate bore diameter, d, inch	↑
Meter tube internal diameter, D, inch	↓
Flowing Temperature, T_f, °R	↓
Real gas relative density, G_r	↓
Flow hour, hr	↑
Base pressure, p_b, psia	↓
Base temperature, T_b, °R	↑
Compressibility at base conditions, Z_b	↑
Compressibility at flowing conditions, Z_{f1}	↓

Table 2-**4** Relationship of Metering Parameters and Coefficients

Metering Parameters \ Coefficients	Numeric conversion factor, F_n	Orifice calculation factor, F_c	Orifice slope factor, F_{sl}	Expansion factor, Y_1	Base pressure factor, F_{pb}	Base temperature factor, F_{tb}	Flowing temperature factor, F_{tf}	real gas relative density factor, F_{gr}	Super-compressibility factor, F_{pv}
Differential pressure, h_w, inch				↓					
Flowing pressure, p_{f1}, psia				↑					
Orifice plate bore diameter, d, inch	↑	↑	↑	↓					
Meter tube internal diameter, D, inch	↓	↓	↓	↑					
Base pressure, p_b, psia					↓				
Base temperature, T_b, °R						↑			
Flowing Temperature, T_f, °R							↓		
Real gas relative density, G_r			↓					↓	↑
Compressibility at base conditions, Z_b									↑
Compressibility at flowing conditions, Zf1									↓
Reynolds Number		↑	↓	↓					

The sensitivity of gas volume to the parameter of differential pressure in inch of water is shown in **Figure 2-17**. Gas volume increases as differential pressure in inch of water increases and vice versa. As differential pressure in inch of water decreases by 10% from the base case, gas volume is decreased by 5.11%; as differential pressure in inch of water increases by 10% from the base case, gas volume is increased by 4.86%. As for the coefficients, changes in differential pressure will have its effect on the expansion factor and the sensitivity is shown in **Figure 2-23**. Expansion factor decreases as differential pressure in inch of water increases and vice versa. As differential pressure in inch of water decreases by 10% from the base case, expansion factor is increased by 0.02%; as differential pressure in inch of water increases by 10% from the base case, expansion factor is decreased by 0.02%.

The sensitivity of gas volume to the parameter of flowing pressure is shown in **Figure 2-18**. Gas volume increases as flowing pressure increases and vice versa. As flowing pressure decreases by 10% from the base case, gas volume is decreased by 5.83%; as flowing pressure increases by 10% from the base case, gas volume is increased by 5.62%. As for the coefficients, changes in flowing pressure will have its effect on the expansion factor and the sensitivity is shown in **Figure 2-24**. Expansion factor increases as flowing pressure increases and vice versa. As flowing pressure decreases by 10% from the base case, expansion factor is decreased by 0.02%; as flowing pressure increases by 10% from the base case, expansion factor is increased by 0.02%.

The sensitivity of gas volume to the parameter of flowing temperature is shown in **Figure 2-19**. Gas volume decreases as flowing temperature increases and vice versa. As flowing temperature decreases by 10% from the base case, gas volume is increased by 1.12%; as flowing temperature increases by 10% from the base case, gas volume is decreased by 1.05%. As for the coefficients, changes in flowing temperature will have its effect on the flowing temperature factor and the sensitivity is shown in **Figure 2-25**. Flowing temperature factor decreases as flowing temperature increases and vice versa. As flowing temperature decreases by 10% from the base case, flowing temperature factor is increased by 0.45%; as flowing temperature increases by 10% from the base case, flowing temperature factor is decreased by 0.44%.

The sensitivity of gas volume to the parameter of meter tube internal diameter is shown in **Figure 2-20**. Gas volume decreases as meter tube internal diameter increases and vice versa. As meter tube internal diameter decreases by 10%, gas volume is increased by 1.97%.; as meter tube internal diameter increases by 10%, gas volume is decreased by 1.19%. As for the coefficients, changes in meter tube internal diameter will have its effect on the numeric conversion factor, orifice calculation factor, orifice slope factor, and expansion factor. The sensitivity for the numeric conversion factor is shown in **Figure 2-26** and numeric conversion factor decreases as meter tube internal diameter increases and vice versa. As meter tube internal diameter decreases by 10%, numeric conversion factor is increased by 1.74%.; as meter tube internal diameter increases by 10%, numeric conversion factor is decreased by 1.01%. The sensitivity for the orifice calculation factor is shown in **Figure 2-27** and orifice calculation factor decreases as meter tube internal diameter increases and vice versa. As meter tube internal diameter decreases by 10%, orifice calculation factor is increased by 0.17%.; as meter tube internal diameter increases by 10%, orifice calculation factor is decreased by 0.15%. The sensitivity for the orifice slope factor is shown in **Figure 2-28** and orifice slope factor decreases as meter tube internal diameter increases and vice versa. As meter tube internal diameter decreases by 10%, orifice slope factor is increased by 42.25%.; as meter tube internal diameter increases by 10%, orifice slope factor is decreased by 25.83%. The sensitivity for the expansion factor is shown in **Figure 2-29** and expansion factor increases as meter tube internal diameter increases and vice versa. As meter tube internal diameter decreases by 10%, expansion factor is decreased by 0.005%.; as meter tube internal diameter increases by 10%, expansion factor is increased by 0.003%.

The sensitivity of gas volume to the parameter of orifice plate bore diameter is shown in **Figure 2-21**. Gas volume increases as orifice plate bore diameter increases and vice versa. As orifice plate bore diameter decreases by 10%, gas volume is decreased by 20.05%; as orifice plate bore diameter increases by 10%, gas volume is increased by 23.10%. As for the coefficients, changes in orifice plate bore diameter will have its effect on the numeric conversion factor, orifice calculation factor, orifice slope factor, and expansion factor. The sensitivity for the numeric conversion factor is shown in **Figure 2-30** and numeric conversion factor increases as orifice plate bore diameter increases and vice versa. As orifice plate bore diameter decreases by 10%, numeric conversion factor is decreased by 19.89%.; as orifice plate bore diameter increases by 10%, numeric conversion factor is increased by 22.86%. The sensitivity for the orifice calculation factor is shown in **Figure 2-31** and orifice calculation factor increases as orifice plate bore diameter increases and vice versa. As orifice plate bore diameter decreases by 10%, orifice calculation factor is decreased by 0.18%.; as orifice plate bore diameter increases by 10%, orifice calculation factor is increased by 0.15%. The sensitivity for the orifice slope factor is shown in **Figure 2-32** and orifice slope factor increases as orifice plate bore diameter increases and vice versa. As orifice plate bore diameter decreases by 10%, orifice slope factor is decreased by -24.63%.; as orifice plate bore diameter increases by 10%, orifice slope factor is increased by 32.37%. The sensitivity for the expansion factor is shown in **Figure 2-33** and expansion factor decreases as orifice plate bore diameter increases and vice versa. As orifice plate bore diameter decreases by 10%, expansion factor is increased by 0.003%.; as orifice plate bore diameter increases by 10%, expansion factor is decreased by 0.004%.

The sensitivity of gas volume to the parameter of real gas relative density is shown in **Figure 2-22**. Gas volume decreases as meter tube internal diameter increases and vice versa. As meter tube internal diameter decreases by 10%, gas volume is increased by 3.91%.; as meter tube internal diameter increases by 10%, gas volume is decreased by 3.06%. As for the coefficients, changes in real gas relative density will have its effect on the orifice slope factor, real gas relative density factor, and supercompressibility factor. The sensitivity for the orifice slope factor is shown in **Figure 2-34** and orifice slope factor decreases as real gas relative density increases and vice versa. As real gas relative density decreases by 10%, orifice slope factor is increased by 2.80%.; as real gas relative density increases by 10%, orifice slope factor is decreased by 2.61%. The sensitivity for the real gas relative density factor is shown in **Figure 2-35** and real gas relative density factor decreases as real gas relative density increases and vice versa. As real gas relative density decreases by 10% from the base case, real gas relative density factor is increased by 5.41%; as real gas relative density increases by 10% from the base case, real gas relative density factor is decreased by 4.65%. The sensitivity for the supercompressibility factor is shown in **Figure 2-36** and supercompressibility factor increases as real gas relative density increases and vice versa. As real gas relative density decreases by 10% from the base case, supercompressibility factor is decreased by 1.43%; real gas relative density increases by 10% from the base case, supercompressibility factor is increased by 1.68%.

One of the fluid and flowing conditions for measuring using orifice meter set by AGA is that the Reynolds number has to be greater than 4,000. Fluid behavior between a Reynolds number of 2,000 and 4,000 is difficult to predict and for Reynolds number below 2,000 the flow becomes laminar flow. Since **Equation 2-10** and **Equation 2-11** are developed using Reynolds number greater than 4,000, for any Reynolds number below that limit, the standard empirical equations of coefficients of discharge will not be valid to the same tolerance.

Reynolds number is calculated based on an iterative scheme using **Equation 2-42**, starting with an assumed coefficient of discharge of 0.6. Gas volume decreases as Reynolds number increases and vice versa as in **Figure 2-37**. As Reynolds number decreases by 10%, gas volume is increased by 0.006%; as Reynolds number increases by 10%, gas volume is decreased by 0.007%. For the base case, the lowest threshold for the gas flow rate would be 0.60 *Mcf/hr* and 14.40 *Mcf/Day* for Reynolds number of 4,000. For the normal operating flow range of gases, the Reynolds numbers are orders of magnitude higher than this low limit of 4,000 and can easily surpass well above this requirement. Also, for high Reynolds number, the effect of viscosity is negligible and the viscosity variation can be ignored. Viscosity of the flowing gas will still be monitored in our calculations in cases of any discrepancies.

$$ReD = 47.0723\frac{Q_v G_r}{D} \quad \textbf{(2-42)}$$

Reynolds Number affects the calculations of orifice calculation factor and the orifice slope factor, as the sum of these two factors is the coefficients of discharge. orifice calculation factor increases as Reynolds number increases and vice versa (**Figure 2-38**). orifice slope factor decreases as Reynolds number increases and vice versa (**Figure 2-39**). Coefficients of discharge decreases as Reynolds number increases and vice versa (**Figure 2-40**) due to the larger magnitude of change of the orifice slope factor compared to the magnitude of change of the orifice calculation factor. As Reynolds number decreases by 10%, coefficients of discharge are increased by 0.006%; as Reynolds number increases by 10%, coefficients of discharge are decreased by 0.007%. The relationship is also observed in **Table 2-4**. The coefficients of discharge approach a constant as the Reynolds number approaches infinity as we can observe from the trends of the **Figure 2-40**, as Reynolds number gets larger and larger, the uncertainty of the coefficients will become more negligible especially in terms of gas volume calculations.

To summarize the sensitivity of gas volume with respect to each of the input parameters, for every 10% of increase in orifice meter parameters, **Table 2-5** provides the ranking (largest to smallest) of the parameters to changes in gas volume. For every 10% of decrease in orifice meter parameters, **Table 2-6** provides the ranking (largest to smallest) of the parameters of changes in gas volume.

Table 2-**5** Rankings of the Parameters to the changes in Gas Volume .

10% Change of Orifice Meter Parameter	Percentage of Change of Gas Volume
Orifice Plate Bore Diameter	23.10
Flowing Pressure	5.62
Differential Pressure in inch of Water	4.86
Flowing Temperature	-1.05
Meter Tube Internal Diameter	-1.19
Real Gas Relative Density	-3.06

Table 2-**6** Rankings of the Parameters to the changes in Gas Volume

-10% Change of Orifice Meter Parameter	Percentage of Change of Gas Volume
Real Gas Relative Density	3.91
Meter Tube Internal Diameter	1.97
Flowing Temperature	1.12
Differential Pressure in inch of Water	-5.11
Flowing Pressure	-5.83
Orifice Plate Bore Diameter	-20.05

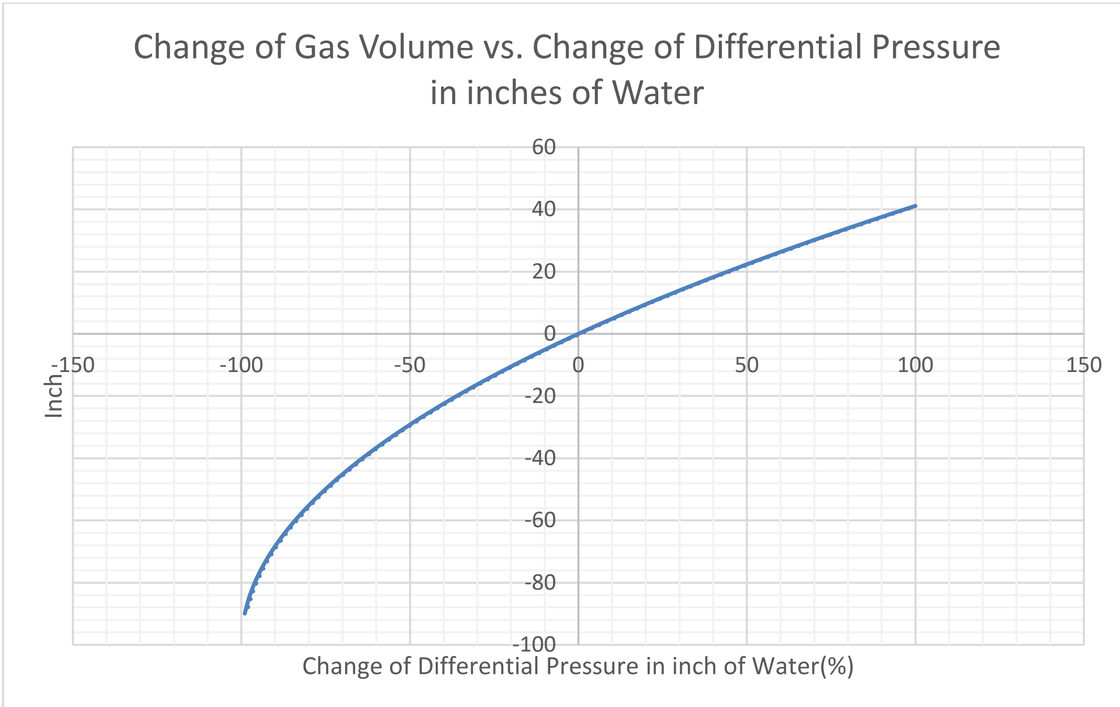

Figure **2-17** Change of Gas Volume vs. Change of Differential Pressure

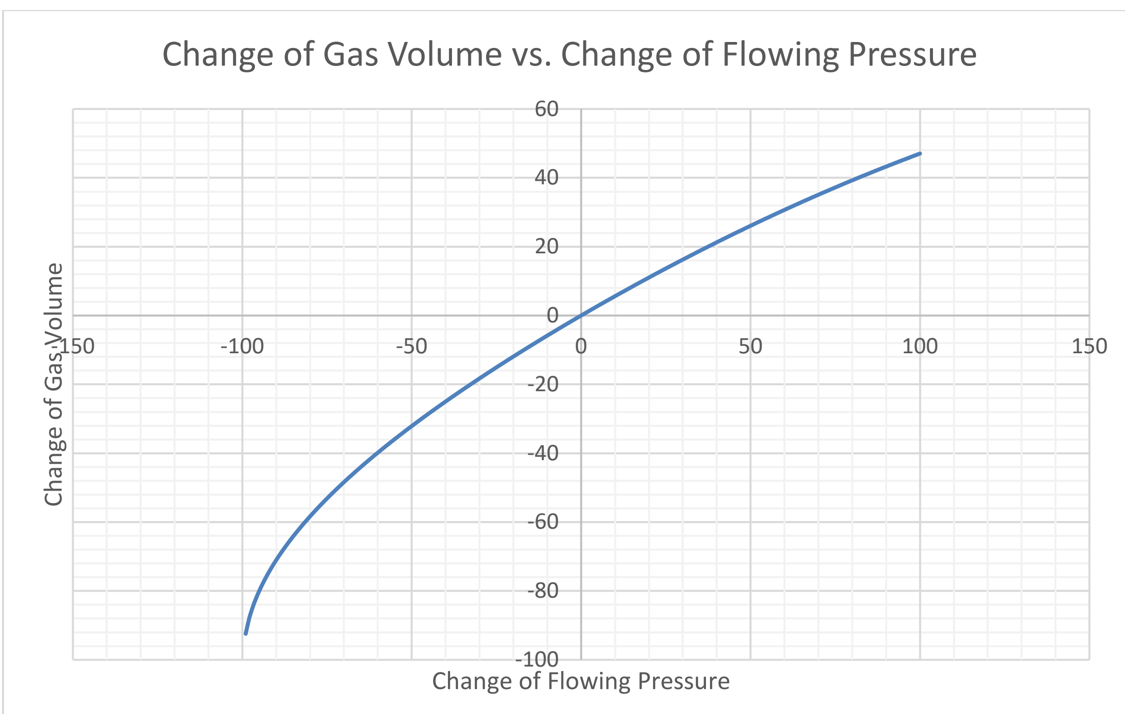

Figure **2-18** Change of Gas Volume vs. Change of Flowing Pressure

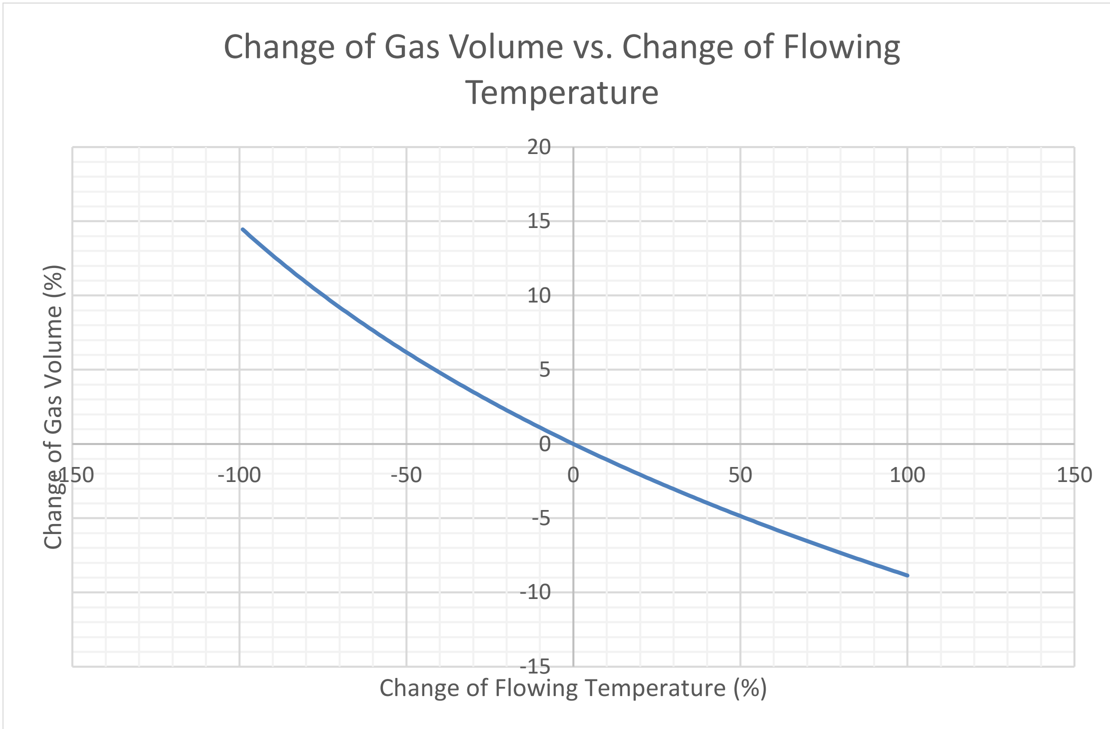

Figure **2-19** Change of Gas Volume vs Change of Flowing Temperature

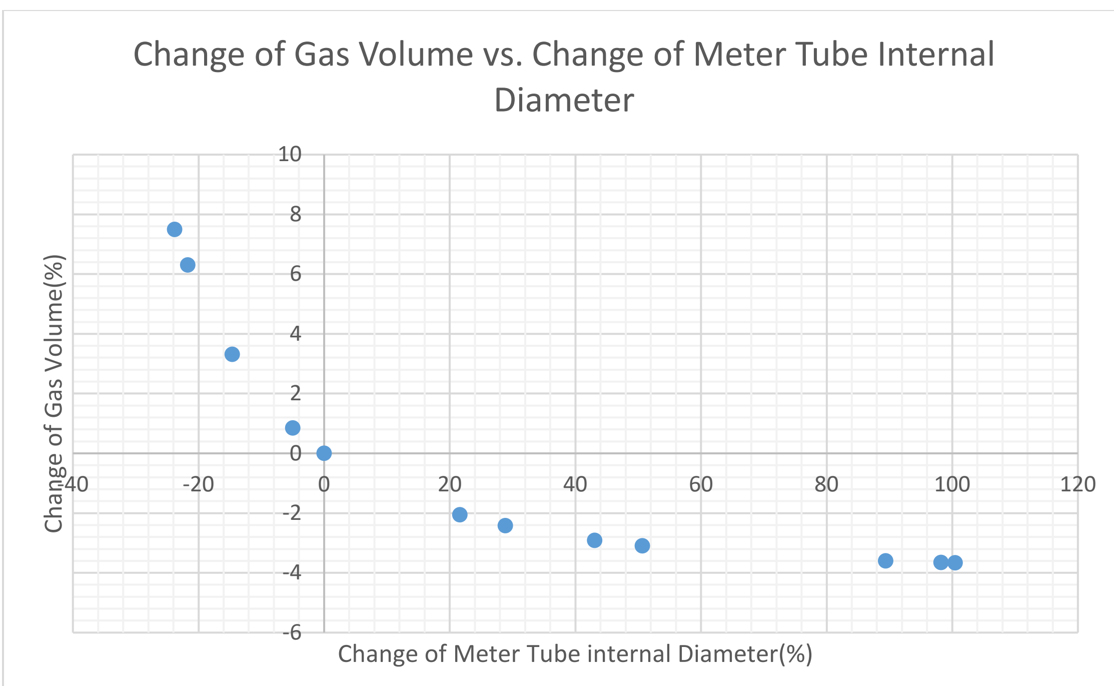

Figure **2-20** Change of Gas Volume vs. Change of Meter Tube Internal Diameter

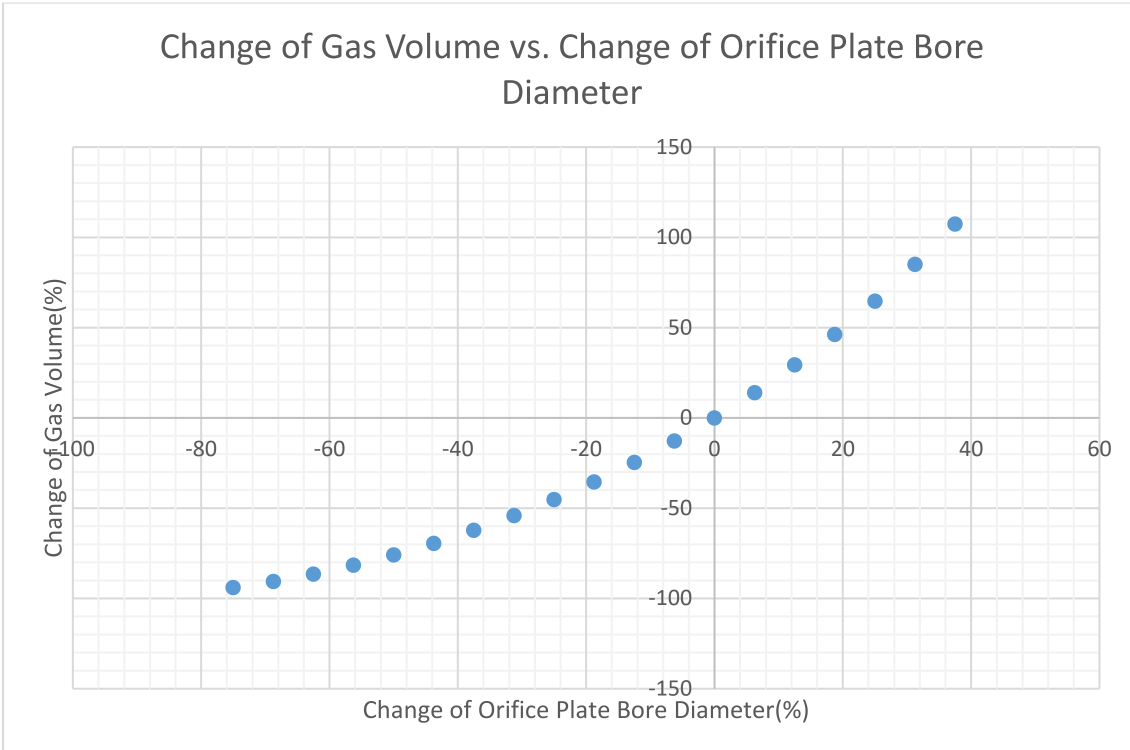

Figure **2-21** Change of Gas Volume vs. Change of Orifice Plate Bore Diameter

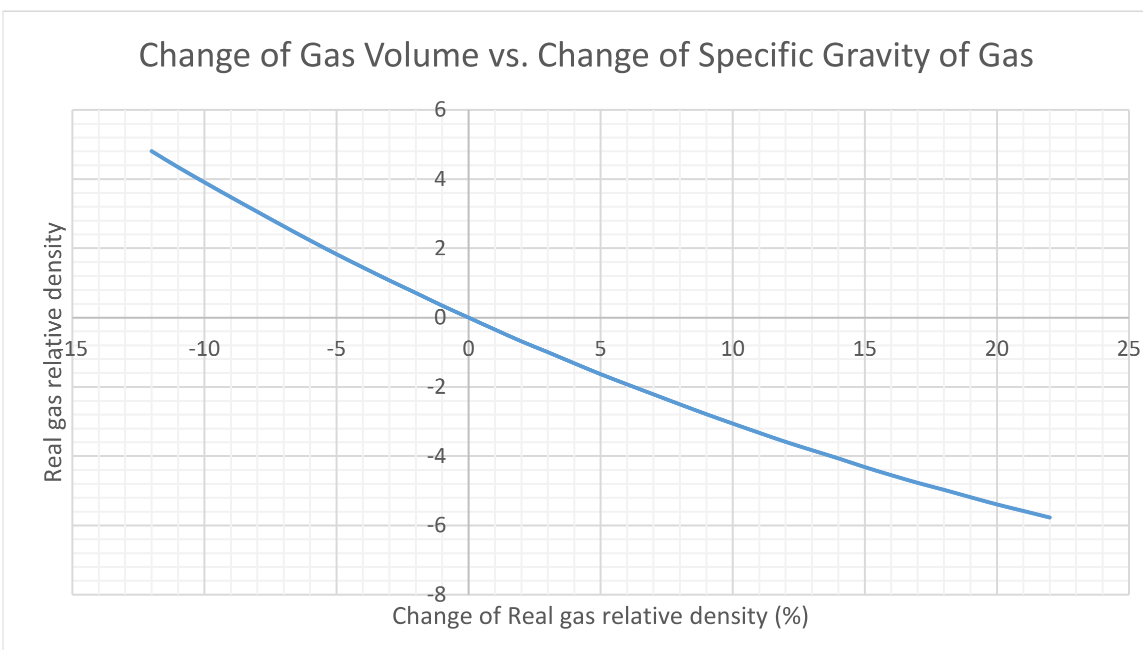

Figure **2-22** Change of Gas Volume vs. Change of Specific Gravity of Gas

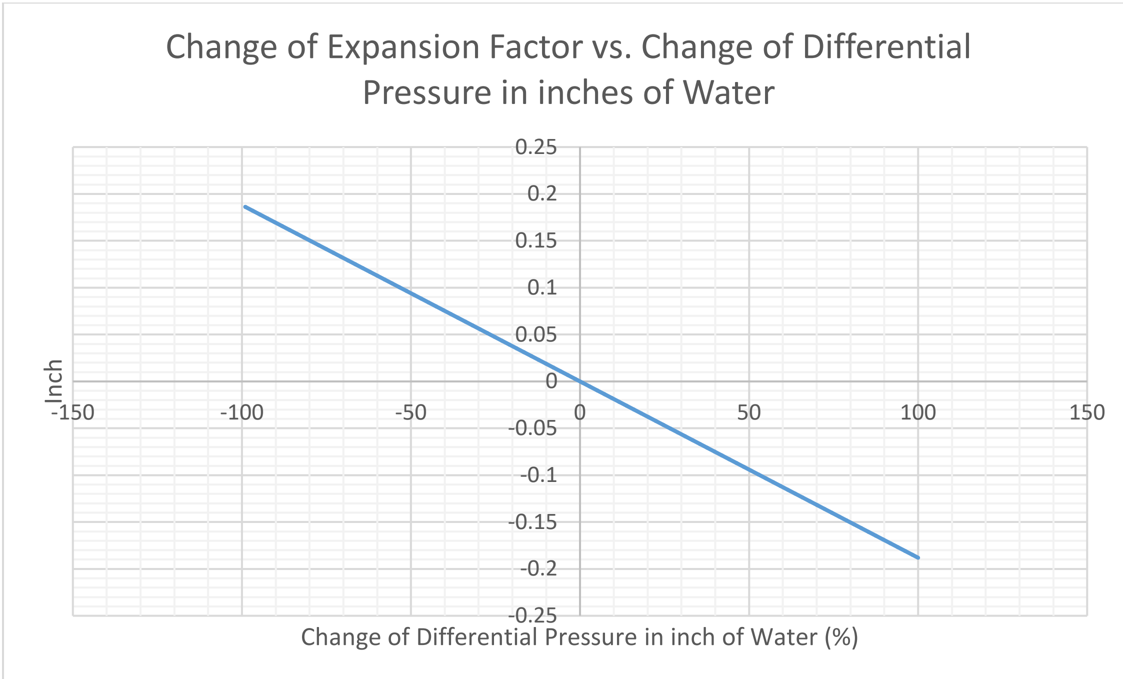

Figure **2-23** Change of Expansion Factor vs. Change of Differential Pressure

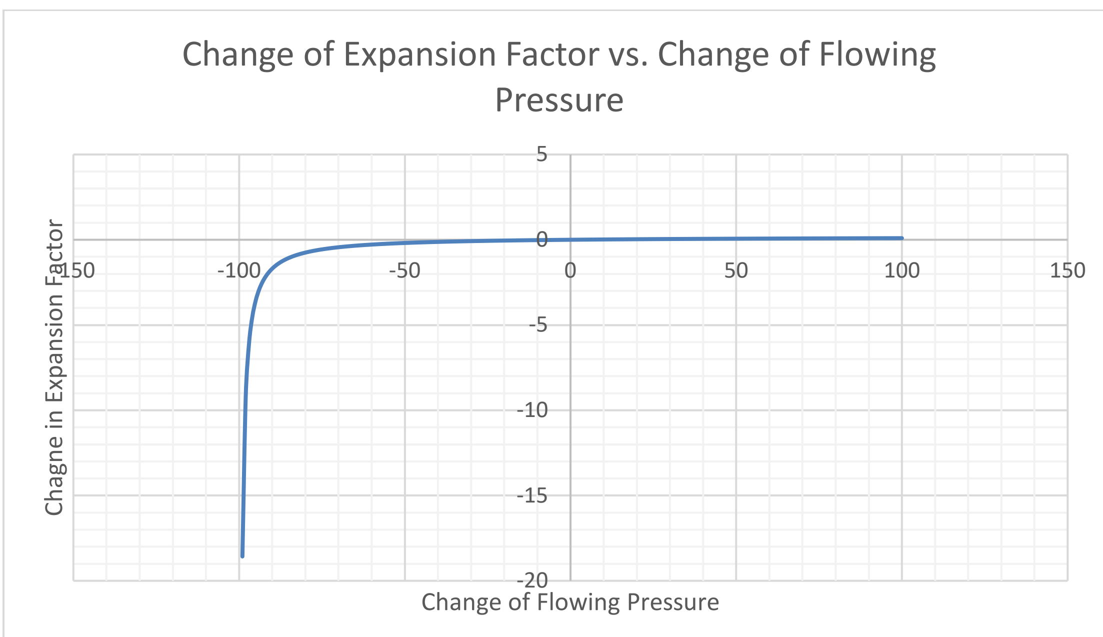

Figure **2-24** Change of Expansion Factor vs. Change of Flowing Pressure

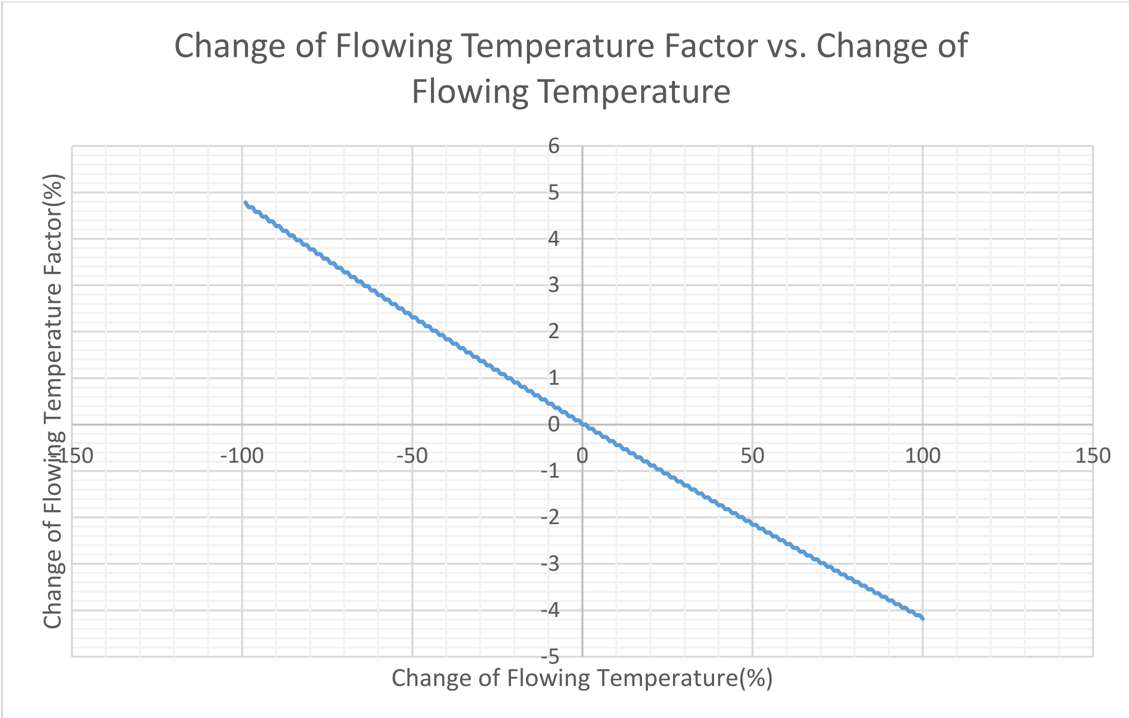

Figure **2-25** Change of Flowing Temperature Factor vs. Change of Flowing Temperature

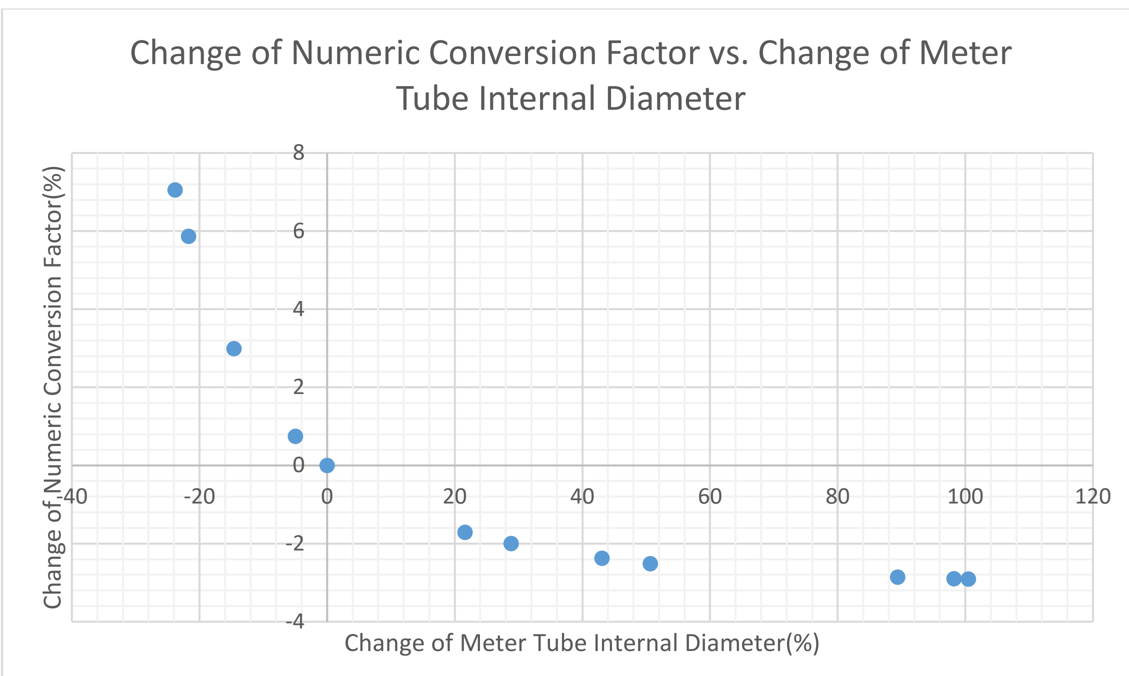

Figure **2-26** Change of Numeric Conversion Factor vs. Change of Meter Tube Internal Diameter

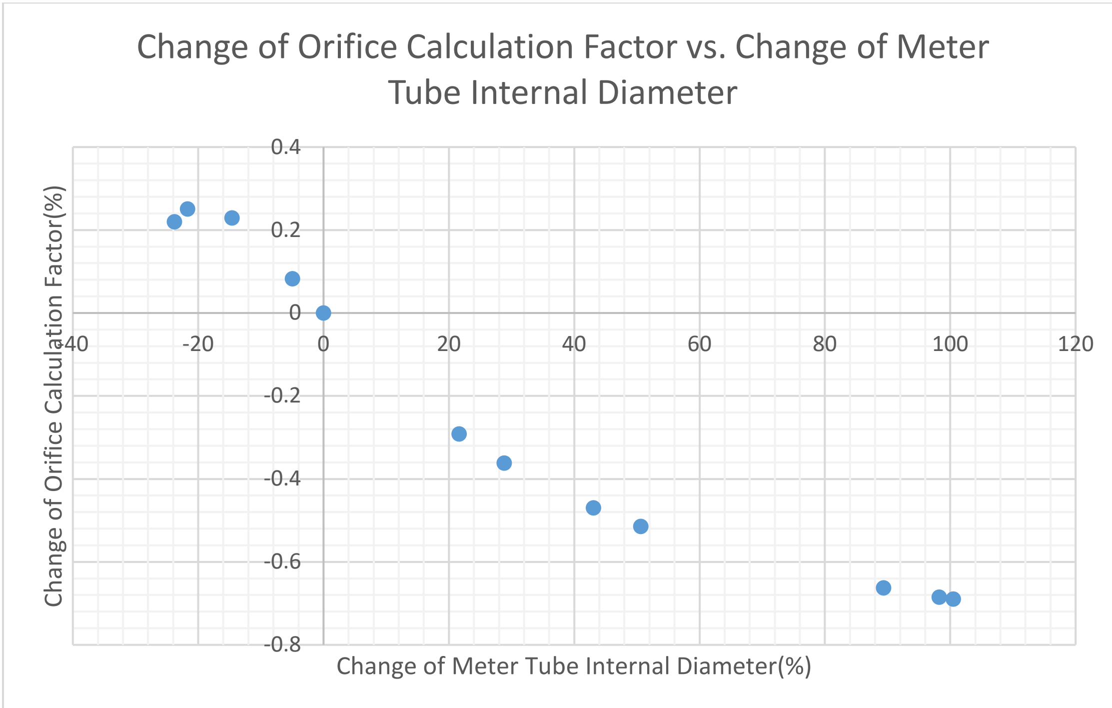

Figure **2-27** Change of Orifice Calculation Factor vs. Change of Meter Tube Internal Diameter

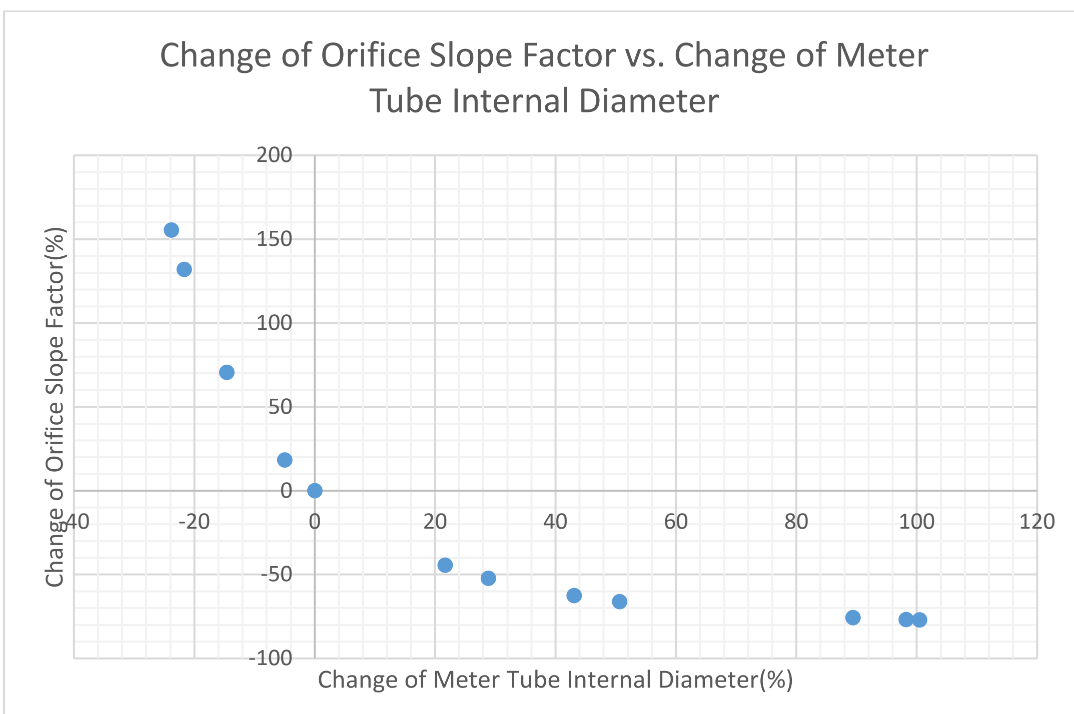

Figure **2-28** Change of Orifice Slope Factor vs. Change of Meter Tube Internal Diameter

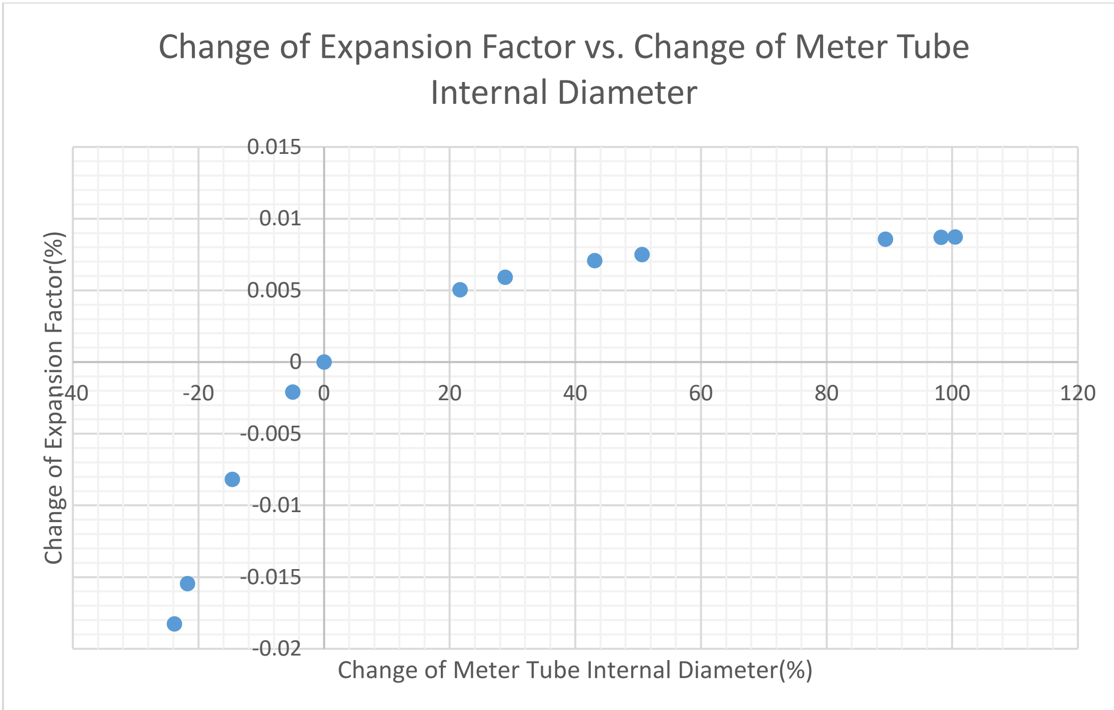

Figure **2-29** Change of Expansion Factor vs. Change of Meter Tube Internal Diameter

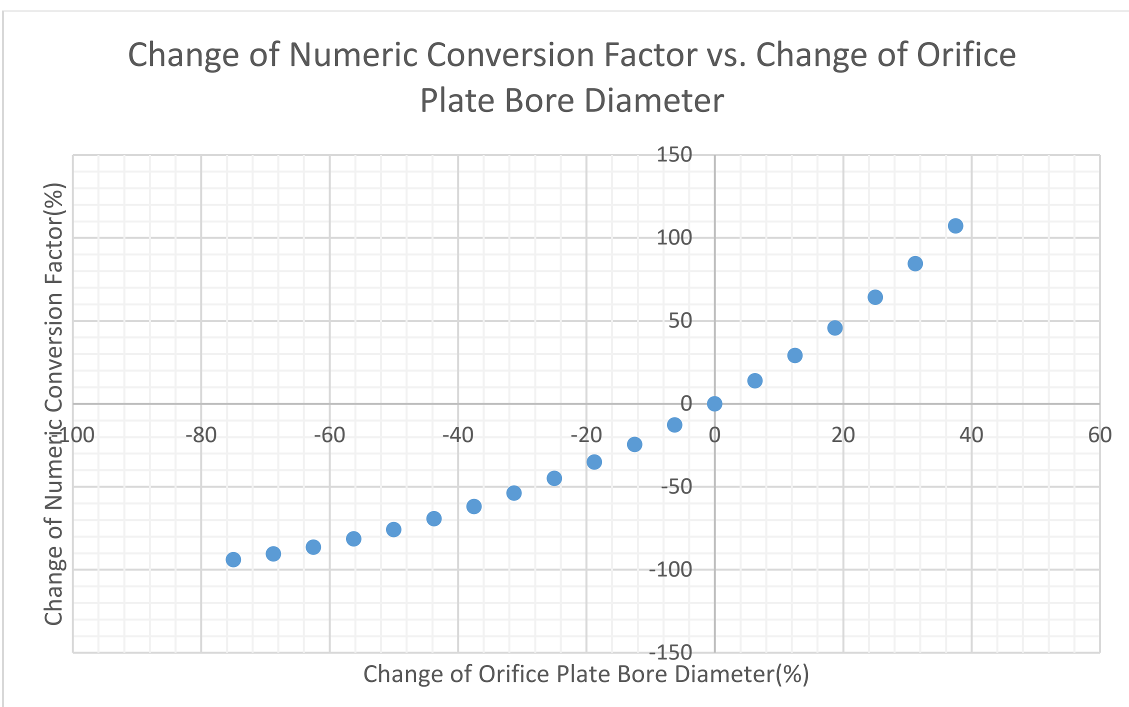

Figure **2-30** Change of Numeric Conversion Factor vs. Change of Orifice Plate Bore Diameter

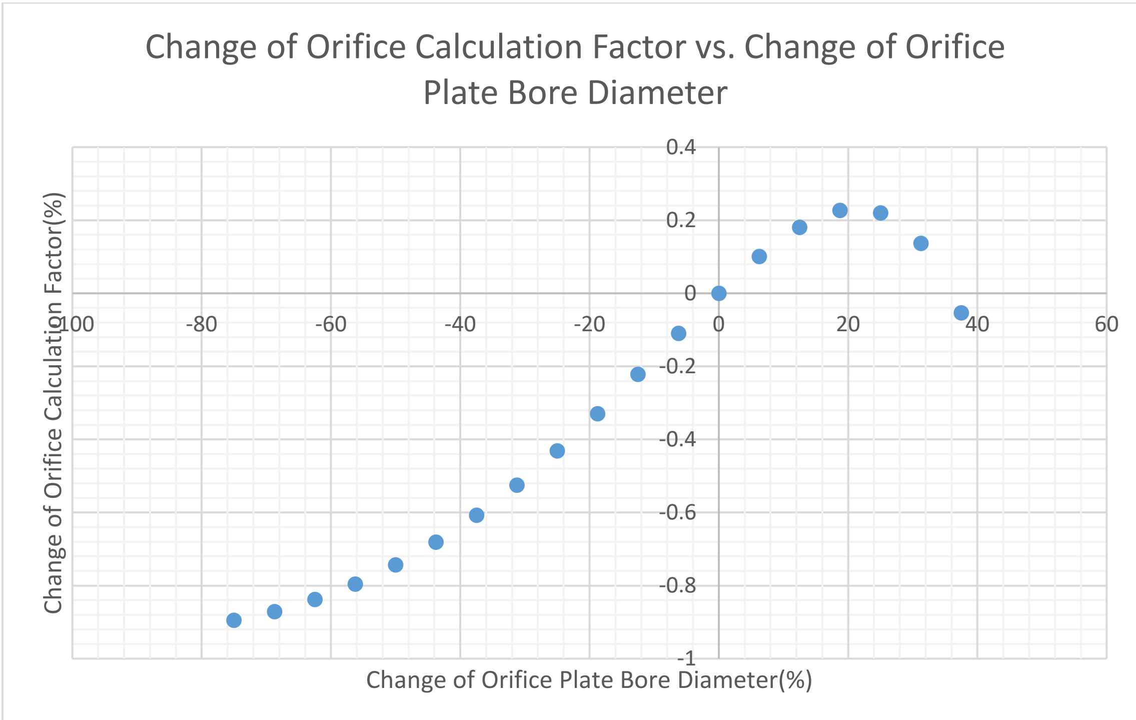

Figure **2-31** Change of Orifice Calculation Factor vs. Change of Orifice Plater Bore Diameter

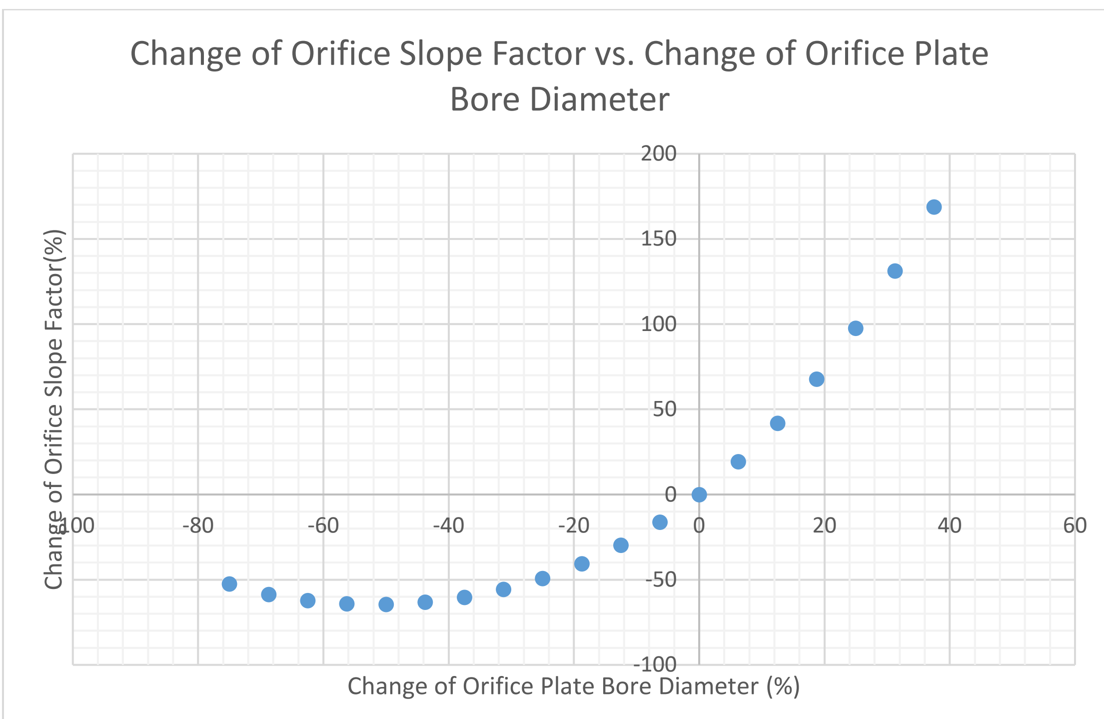

Figure **2-32** Change of Orifice Slope Factor vs. Change of Orifice Plate Bore Diameter

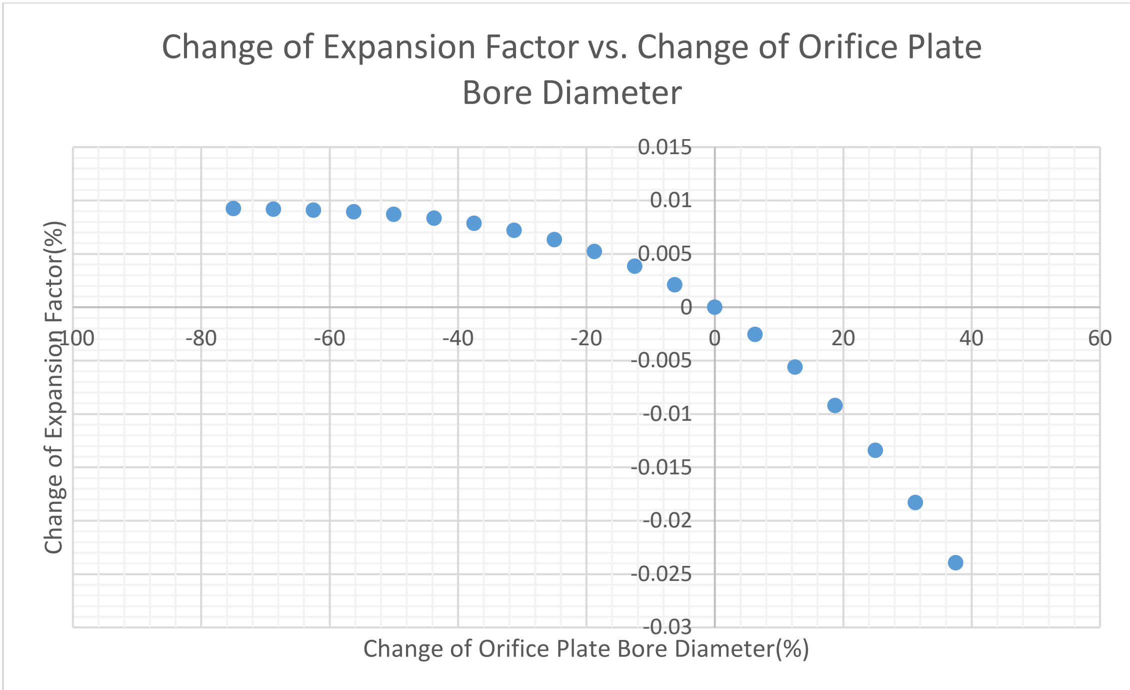

Figure **2-33** Change of Expansion Factor vs. Change of Orifice Plate Bore Diameter

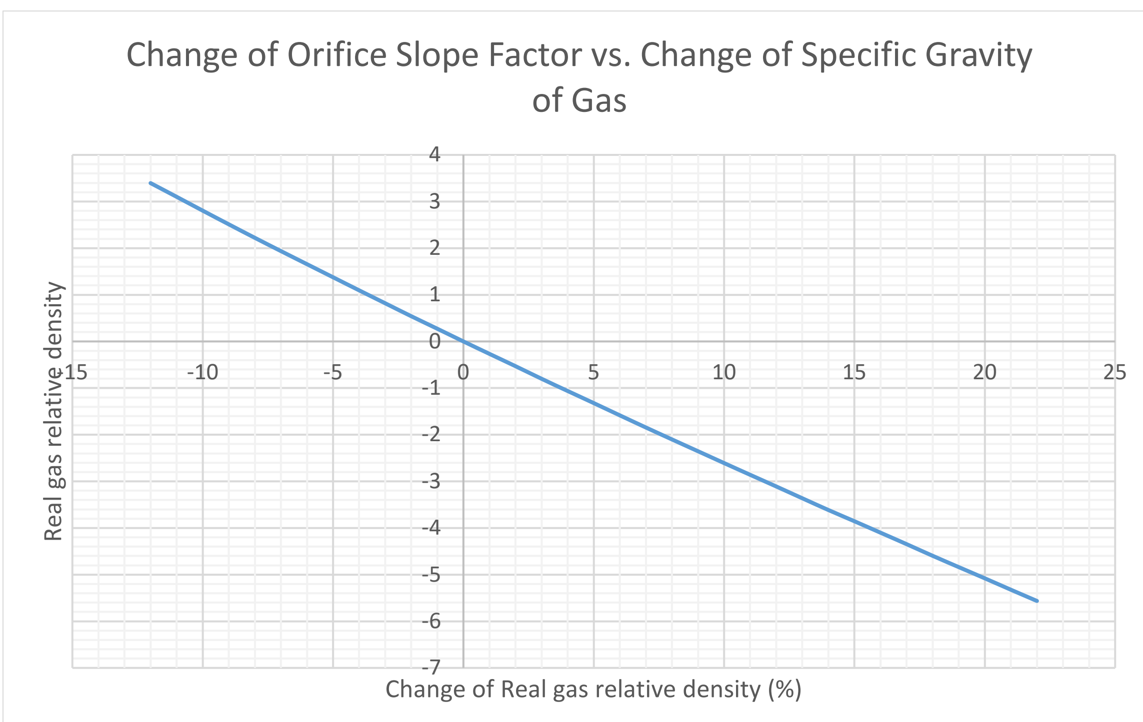

Figure **2-34** Change of Orifice Slope Factor vs. Change of Specific Gravity of Gas

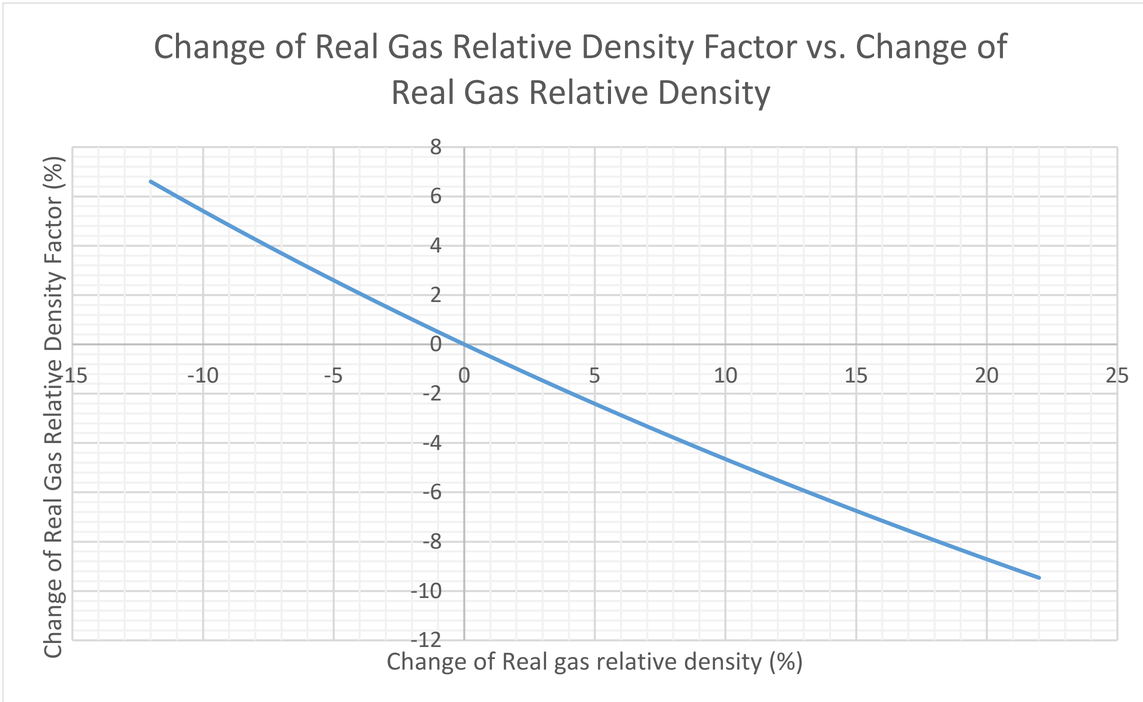

Figure **2-35** Change of Real Gas Relative Density Factor vs. Change of Real Gas Relative Density

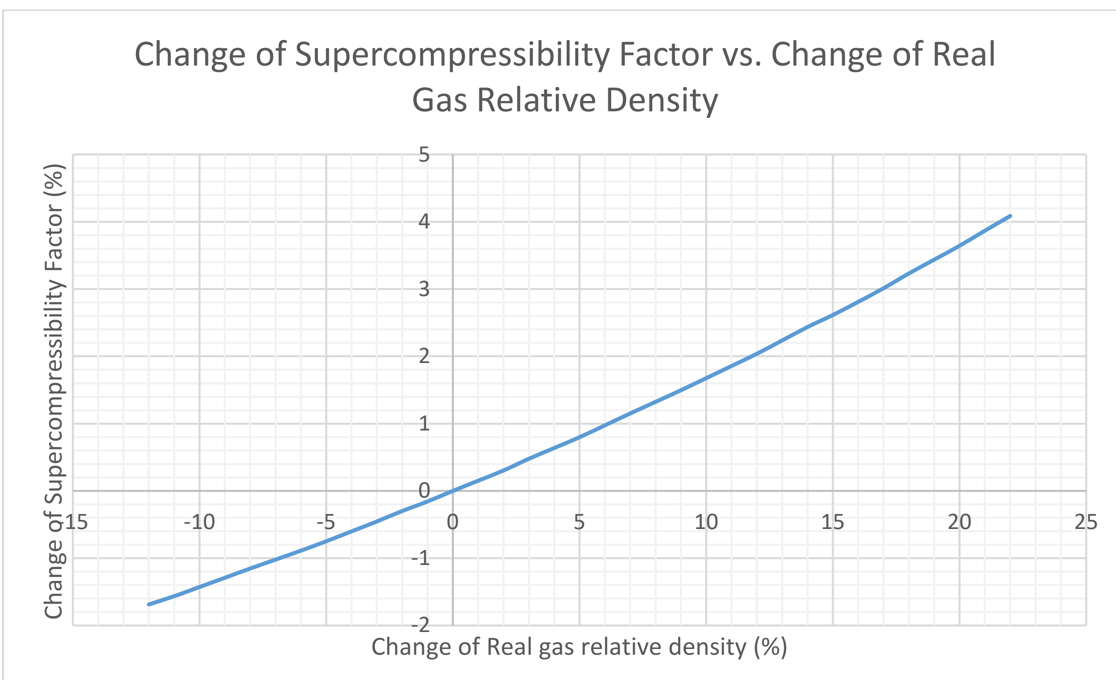

Figure **2-36** Change of Supercompressibility Factor vs. Change of Real Gas Relative Density

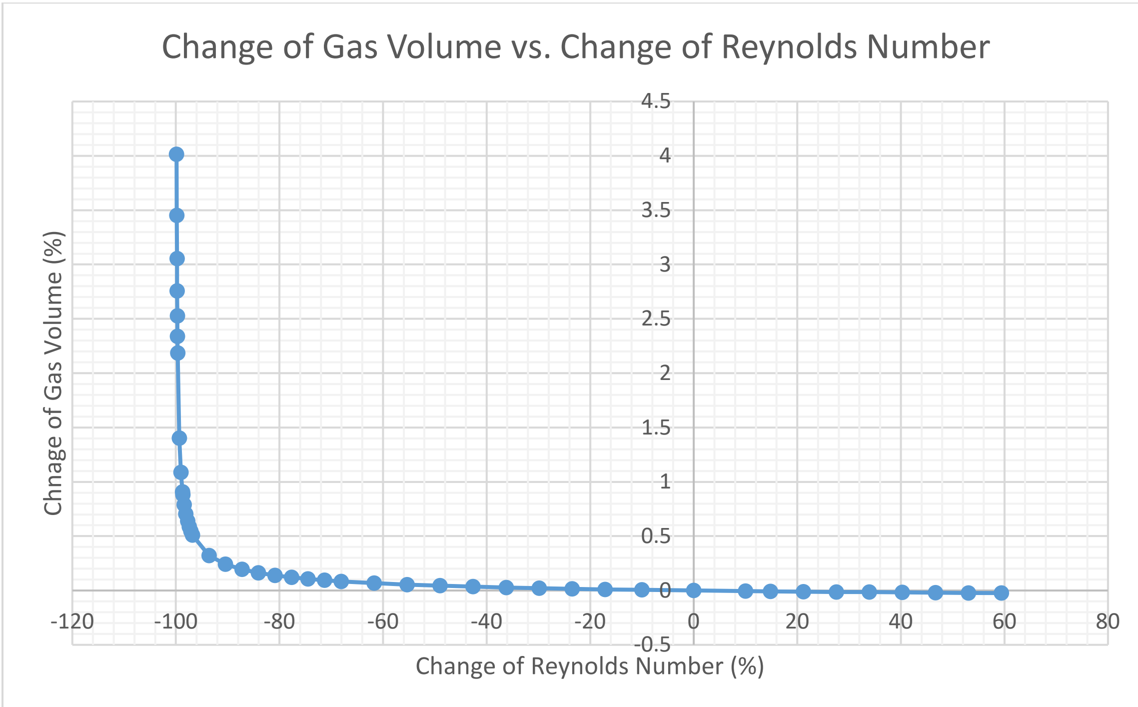

Figure **2-37** Change of Gas Volume vs. Change of Reynolds Number

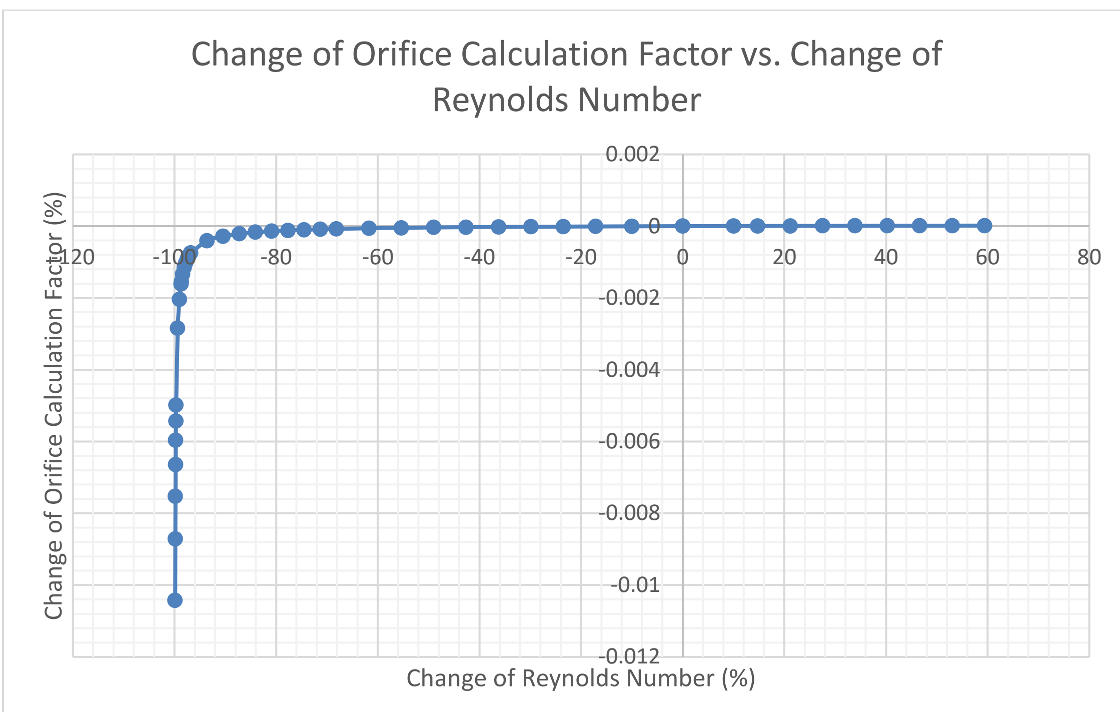

Figure **2-38** Change of Orifice Calculation Factor vs. Change of Reynolds Number

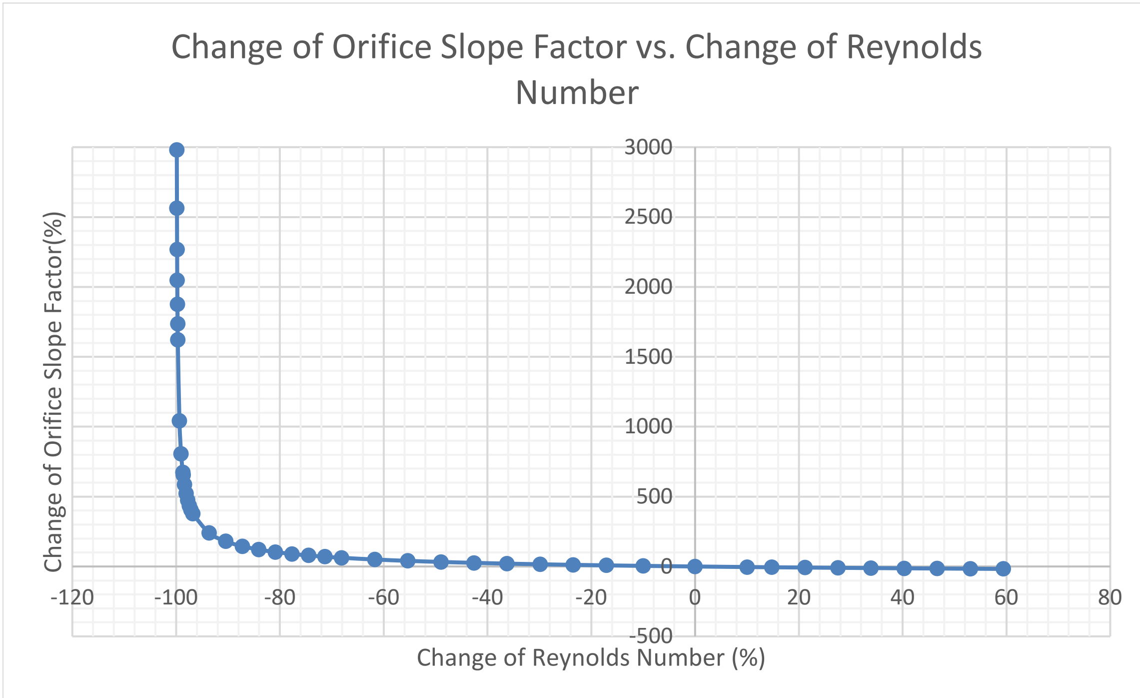

Figure **2-39** Change of Orifice Slope Factor vs. Change of Reynolds Number

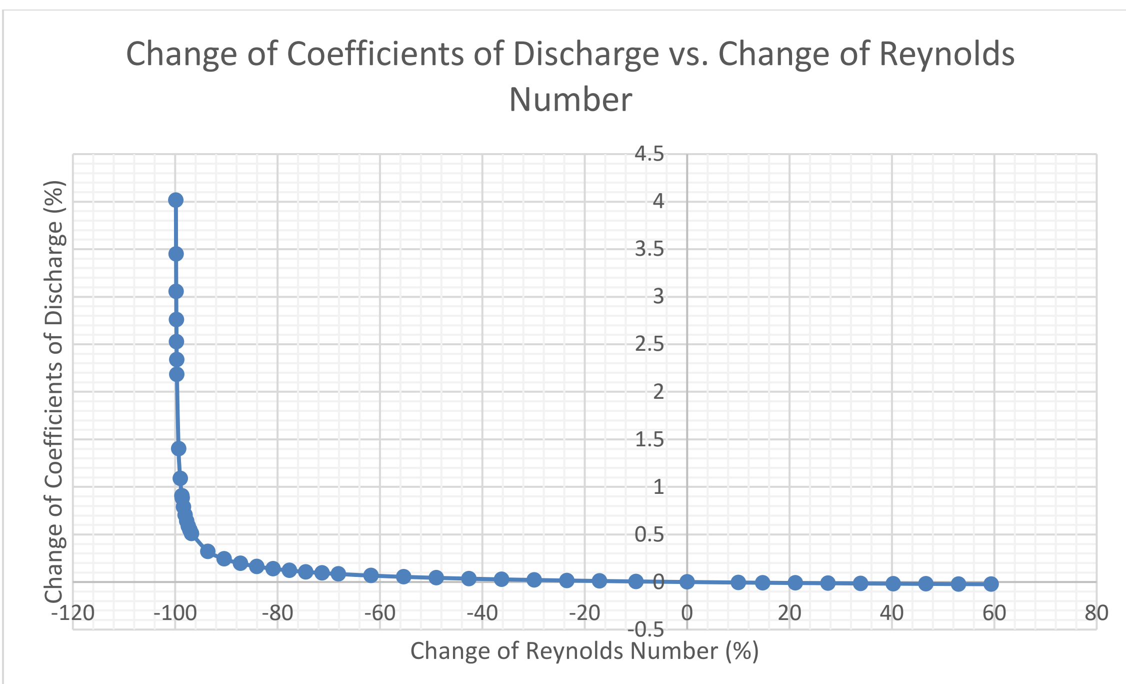

Figure **2-40** Change of Coefficients of Discharge vs. Change of Reynolds Number

2.5 Conclusion

To meet the needs for shale gas development and accurate measurement of high-volume gas wells, this paper provides a comprehensive and in-depth review and analysis of applicable metering and gas volume measurement technologies, including Coriolis, turbine, v-cone, and orifice meters. Conclusions include:

- For accurate orifice metering, one needs to understand and calibrate meters to eliminate effects of installation, swirl, chemical and organic contamination, physical deformation, etc.
- Out of the factors affecting Orifice metering and measurement, orifice bore diameter, flowing pressure, differential pressure, and gas composition affect measurement the most (in order of high to low impact). Flowing time is critical especially when gas flow is not continuous, such as when a plunger lift is installed.

We observed that in dry gas Marcellus and Utica gas region, most wells, with the except of one operator and twelve wells out of hundreds and thousands of wells, were equipped with orifice metering and measurement for its low cost, accuracy, and ease of calibration and maintenance. As gas flow rates drop and Reynolds number decreases, one could and should change Orifice plate size and calibrate the meter to maintain accuracy of measurement.

This article provides one with up-to-date understanding of physics and practices needed in natural gas metering and volume measurement. Meter design and measurement could be improved if the following factors could be considered: variable flow rates during the life of a shale gas well, compositional change of shale gas, and potential storage and measurement of CO_2, H_2, and CH_4.

Reference

American Gas Association, Report No. 1, 1930: Gas Measurement Manuals - Part 1: General.

American Gas Association, Report No. 3, 1955: Orifice Metering of Natural Gas and Other Related Hydrocarbon Fluids, 1st Edition.

American Gas Association, Report No. 3, 1985a: Orifice Metering of Natural Gas and Other Related Hydrocarbon Fluids, 2nd Edition.

American Gas Association, Report No. 8, 1985b: Compressibility Factors of Natural Gas and Other Related Hydrocarbon Gases, 1st Edition.

American Gas Association, Report No. 3, 1992: Orifice Metering of Natural Gas and Other Related Hydrocarbon Fluids, 3rd Edition.

American Gas Association, Report No. 11, 2001: Coriolis Flow Measurement for Natural Gas Applications. Washington, D.C.: American Gas Association, 2001. Print.

American Gas Association, Report No. 7, 2006: Measurement of Natural Gas by Turbine Meters, 2006 Edition.

American Gas Association, Report No. 3, 2012: Orifice Metering of Natural Gas and Other Related Hydrocarbon Fluids, 4th Edition.

American Petroleum Institute, 2002: Manual of Petroleum Measurement Standards Chapter 5 – metering, Section 6 – measurement of liquid hydrocarbons by Coriolis meters (API MPMS Chapter 5.6, R2008); 2002.

Anklin, Martin, et al., 2006: “Coriolis Mass Flowmeters: Overview of the Current State of the Art and Latest Research.” *Flow Measurement and Instrumentation*, vol. 17, no. 6, pp. 317–323., doi:10.1016/j.flowmeasinst.2006.07.004.

Baker, R.C., 1991: “Turbine and Related Flowmeters: I. Industrial Practice.” *Flow Measurement and Instrumentation*, vol. 2, no. 3, pp. 147–161., doi:10.1016/0955-5986(91)90027-o.

Baker, R. C., 2016: Flow Measurement Handbook: Industrial Designs, Operating Principles, Performance, and Applications. Cambridge, UK: Cambridge UP, 2016, Second Edition.

Bean, H.S., 1935: “Values of Discharge Coefficients of Square-Edged Orifices: Comparison of Results Obtained by Tests Using Gases with Those Obtained by Tests Using Water,” American Gas Association Monthly, Vol 17, p. 259.

Beitler, S.R., 1935: “The Flow of water Through Orifices” (Bulletin 89), Engineering Experiment Station, Ohio State University, Columbus.

Benedict, R.P., Wyler, J.S., Brandt, G.B., 1974: The effect of edge sharpness on the discharge coefficient of an orifice. Trans ASME J. Eng. Power: paper No 72-WA/FM-4

Blumenthal, I., 1984: Improving productivity through mass flow measurement and control. Enhancing Productivity, Proc. Pacific Cascade Instrumentation ’84 Exhib. Symp. ISA: 163-8.

Bobovnik, G., et al., 2005: “Coupled Finite-Volume/Finite-Element Modelling of the Straight-Tube Coriolis Flowmeter.” *Journal of Fluids and Structures*, vol. 20, no. 6, pp. 785–800., doi:10.1016/j.jfluidstructs.2005.04.008.

Bobovnik, G., et al., 2013: “Numerical Analysis of Installation Effects in Coriolis Flowmeters: A Case Study of a Short Straight Tube Full-Bore Design.” *Flow Measurement and Instrumentation*, vol. 34, pp. 142–150., doi:10.1016/j.flowmeasinst.2013.10.004.

Bobovnik, G., et al., 2015: “Numerical Analysis of Installation Effects in Coriolis Flowmeters: Single and Twin Tube Configurations.” *Flow Measurement and Instrumentation*, vol. 44, pp. 71–78., doi:10.1016/j.flowmeasinst.2014.10.001.

Brain, T.J.S., Reid, J., 1973: Measurement of orifice plate edge sharpness. Meas Control 6:377–384

Buckingham, E., 1932: “Notes on the Orifice Meter: The Expansion Factor for Gases,” National Bureau of Standards Journal of Research, Vol 9, RP 459, p. 61.

Cheesewright, R, et al., 2000: “The Identification of External Factors Which Influence the Calibration of Coriolis Massflow Meters.” *Flow Measurement and Instrumentation*, vol. 11, no. 1, pp. 1–10., doi:10.1016/s0955-5986(99)00023-0.

Crocket, K.A., Upp, E.L., 1973: The measurement and effects of edge sharpness on the flow coefficients of standard orifices. Trans ASME J Fluids Eng (June): 271–275

DeOtte R.E., Morrison G.L., Panak D.L., Nail G.H., 1991: 3-D Laser Doppler Anemometry Measurements of the Axisymmetric Flow Field near an Orifice Plate. Flow Meas Instrum 2(2):115–123.

Dranchuk, P. M., H. Abou-Kassem, 1975: “Calculation of Z Factors for Natural Gases Using Equations of State.” *Journal of Canadian Petroleum Technology*, vol. 14, no. 03, doi:10.2118/75-03-03.

Durst, F., Founti, M. and Wang, A.B., 1988: Experimental investigation of the flow through an axisymmetric constriction. Turbulent Shear Flows, 6, Springer-Verlag, 338-350.

Durst, F., and A. B. Wang, 1989: Experimental and Numerical Investigations of the Axisymmetric, Turbulent Pipe Flow Over a Wall Mounted Thin Obstacle.

Emerson, 2017: *Daniel Orifice Plates and Plate Sealing Units*, Daniel Measurement and Control, Inc., Houston, TX.

Emerson, 2021a: *Micro Motion Technical Overview and Specification Summary*, Micro Motion, Boulder, CO, 2021.

Emerson, Rosemount, 2021b: *Rosemount TM DP Flow Meters and Primary Elements*. September 2021.

Griffiths, A. and J. Newcombe, 1970: Large-volume gas measurement, 36th Autumn Research Meeting of the Institution of Gas Engineers.

Grimley, T.A., 2002: Installation effects testing of Coriolis flow meters with natural gas. In: The fifth international symposium of fluid flow measurement. Arlington, VA, USA

Hodgson, J.L., 1917: The commercial metering of air, gas and steam. Minutes Proc Inst Civ Eng CCIV 108–193

Jepson, P., and R. Chipchase, 1975: “Effect of Plate Buckling on Orifice Meter Accuracy.” Journal of Mechanical Engineering Science, vol. 17, no. 6, pp. 330–337, doi:10.1243/JMES_JOUR_1975_017_047_02.

ISO Standard 5167, 1980: Measurement of Fluid Flow by Means of Orifice Plates, Nozzles and Venturi Tubes Inserted in Circular Cross-Section Conduits Running Full, ISO 5167-1980(E), Geneva.

ISO Standard 5167-5, 2016: Measurement of Fluid Flow by Means of Pressure Differential Devices Inserted in Circular Cross-section Conduits Running Full – Part 5: Cone Meters, ISO 5167-5:2016(E), Geneva.

Kolahi, K., et al., 1994: "Coriolis Mass Flow Measurement of Gas under Normal Conditions." *Flow Measurement and Instrumentation*, vol. 5, no. 4, pp. 275–283., doi:10.1016/0955-5986(94)90031-0.

Koudal, O., Brunner, M., Wenger, A., Sorokin, S.V., 1998: High frequency Coriolis meter performance under pulsating flow conditions, *Proceedings of the 9th International Conference on Flow Measurement*, Sweden, Lund, pp. 239-242.

Kutin, J., et al., 2006: "Velocity Profile Effects in Coriolis Mass Flowmeters: Recent Findings and Open Questions." *Flow Measurement and Instrumentation*, vol. 17, no. 6, pp. 349–358., doi:10.1016/j.flowmeasinst.2006.07.005.

Liu, Weiguang, et al., 2015: "Performance Measurement Analysis of Various Cone Flow Meters with Various Beta Edge Types and Flow Field Parameters." *Flow Measurement and Instrumentation*, vol. 45, pp. 331–340., doi:10.1016/j.flowmeasinst.2015.07.005.

Li, YT, Lee, SY., 1953: A fast-response true-mass-rate flowmeter. Trans ASME, 75:835-841.

Li et al., 2013: “Malfunction diagnosis of sludge deposition in standard orifice plate flowmeter.” *Proceedings of 2013 2nd International Conference on Measurement, Information and Control* 02: 1319-1323.

McCrometer, 2013: *Installation & Maintenance Instructions V-Cone*. McCrometer.

McCrometer, 2013: *VH Wafer Style Specification Sheet*, McCrometer, Hemet, CA

McCrometer, 2018:. *Proven Flow Measurement Solutions for the Oil and Gas Industry*, McCrometer, Hemet, CA

Miller, R. W., 1979: “The Stolz and ASME-AGA Orifice Equation Compared to Laboratory Data,” J. Fluids Eng., vol. 101, no. 4, p. 483-490.

Mole, N., et al., 2008: “An Improved Three-Dimensional Coupled Fluid–Structure Model for Coriolis Flowmeters.” *Journal of Fluids and Structures*, vol. 24, no. 4, pp. 559–575., doi:10.1016/j.jfluidstructs.2007.10.004.

Morrison, GL, et al, 1990: "the Flow Field inside an Orifice Flow Meter." CHEMICAL ENGINEERING PROGRESS, vol. 86, no. 7, pp. 7580.

Morrison, Gerald L., Robert E. DeOtte, and Eric J. Beam, 1992: "Installation Effects upon Orifice Flowmeters." Flow Measurement and Instrumentation, vol. 3, no. 2, pp. 8993doi:10.1016/09555986(92)90005P.

Morrison, G.L., DeOtte Jr., R.E., Nail, G.H., Panak, D.L., 1993: Mean Velocity and Turbulence Fields inside a β=0.50 Orifice Flowmeter. AIChE J. 39, 745-756.

Morrison, G. L., J. Hauglie, and R. E. DeOtte, 1995: "Beta Ratio, Axisymmetric Flow Distortion and Swirl Effects upon Orifice Flow Meters." Flow Measurement and Instrumentation, vol. 6, no. 3, pp. 207216doi:10.1016/0955 5986(95)00009B.

Morrow, T. B., et al., 1991: “Effects of Orifice Meter Installation Condition on Orifice Coefficient Accuracy.” *SPE Gas Technology Symposium*, p. SPE-21509-MS, doi:10.2118/21509-MS.

Nemitallah, M. A., et al., 2014: “Solid Particle Erosion Downstream of an Orifice.” *Journal of Fluids Engineering*, vol. 137, no. 2, doi:10.1115/1.4028283.

Norman, R.S., G.E. Mattingly, S.E. McFaddin, 1989: The Decay of Swirl in Pipes, presented at 1989 International Gas Research Conference, Tokyo, Japan

O'banion, Micro Motion, Inc., Tom, 2013: "Coriolis: The Direct Approach to Mass Flow Measurement." CEP Magazine.

Ouazzane, A. K., and R. Benhadj, 2002: “Flow Conditioners Design and Their Effects in Reducing Flow Metering Errors.” *Sensor Review*, vol. 22, no. 3, MCB UP Ltd, pp. 223–31, doi:10.1108/02602280210433061.

Pope, Jodie G., and John D. Wright., 2014: “Performance of Coriolis Meters in Transient Gas Flows.” *Flow Measurement and Instrumentation*, vol. 37, 2014, pp. 42–53., doi:10.1016/j.flowmeasinst.2014.02.003.

Reader-Harris, M. J., and J. A. Sattary, 1990: "The Orifice Plate Discharge Coefficient Equation." Flow Measurement and Instrumentation, vol. 1, no. 2, pp. 67-76doi:10.1016/09555986(90)900312.

Reader-Harris, M. J., 1994: "The Decay of Swirl in a Pipe." International Journal of Heat and Fluid Flow, vol. 15, no. 3, pp. 212217doi:10.1016/0142727X(94)90040X.

Reader-Harris, M. J., J. A. Sattary, and E. P. Spearman, 1995: "The Orifice Plate Discharge Coefficient Equation — further Work." Flow Measurement and Instrumentation, vol. 6, no. 2, 1995, pp. 101114doi:10.1016/09555986(94)00001O.

Reader-Harris, M., N. Barton, and D. Hodges, 2012: "The Effect of Contaminated Orifice Plates on the Discharge Coefficient." FLOW MEASUREMENT AND INSTRUMENTATION, vol. 25, pp. 2 7doi:10.1016/j.flowmeasinst.2011.11.003.

Reader-Harris, Michael, and SpringerLink, 2015: Orifice Plates and Venturi Tubes, Springer International Publishing, Cham, doi:10.1007/978-3-319-16880-7.

Shan, Feng, et al., 2016: “Effects of the Orifice to Pipe Diameter Ratio on Orifice Flows.” *Chemical Engineering Science*, vol. 152, pp. 497–506, doi:https://doi.org/10.1016/j.ces.2016.06.050.

Sheikholeslami, M. Z., and B. R. Patel, 1988: Numerical Modeling of Flow through Orifice Meters. Topical Report, July 1986 August 1987, United States.

Shen, J. J. S., 1991: Characterization of Swirling Flow and its Effects on Orifice Metering.doi:10.2118/22865MS.

Singh, S.N., et al., 2006: “Effect of Upstream Flow Disturbances on the Performance Characteristics of a V-Cone Flowmeter.” *Flow Measurement and Instrumentation*, vol. 17, no. 5, pp. 291–297., doi:10.1016/j.flowmeasinst.2006.08.003.

SmartMeasurement, 2019: *ALCM-MB Micro-Bend Coriolis Mass Flowmeter Model ALCM Series*, SmartMeasurement, Milwaukee, WI

Stappert, Karl, 2013: FUNDAMENTALS OF CORIOLIS METERS AGA REPORT NO. 11

Stewart, D.G., 2002: Performance of Coriolis meters in gas flow. In: The fifth international symposium of fluid flow measurement (ISFFM)

Stolz, J., 1978: “A Universal Equation for the Calculation of Discharge Coefficient of Orifice Plates,” Flow Measurement of Fluids, North-Holland, Amsterdam.

Szabo, J.L., Winarski, C.P., Hypnar, P. R., 1992: A Review of the V-Cone Meter for Natural Gas Flows, Omae Calgary, Alberta

Tek-Trol, 2021: *Tek-Cor 1100A Coriolis Mass Flow Meter Instruction Manual*, Tek-Trol, Crystal Lake, IL

Trifilieff, Olivier, and Thomas Wines, 2009: "Black Powder Removal from Transmission Pipelines: Diagnostics and Solutions." PALL.

Tsochatzidis, Nikolaos A., 2008: "Study Addresses Black Powder's Effects on Metering Equipment." *Oil & Gas Journal*, vol. 106, no. 12, pp. 56-58, 60-61.

Upp, E.L., 2016: "Fundamentals of Orifice Meter Measurement". Emerson Process Management. N.p.

Wang, Tao, and Roger Baker, 2014: “Coriolis Flowmeters: a Review of Developments over the Past 20 Years, and an Assessment of the State of the Art and Likely Future Directions.” *Flow Measurement and Instrumentation*, vol. 40, pp. 99–123., doi:10.1016/j.flowmeasinst.2014.08.015.

Whetstone JR, Cleveland WG, Bateman BR, Sindt CF, 1988: Measurements of Coefficients of Discharge for Concentric, Flange-tapped, Square-Edged Orifice Meters in Natural Gas over a Reynolds Number Range of 25,000-16,000,000. NIST Technical Note TN-1264. NIST, Washington D.C.

Weymouth, Thomas R., 1912: “Measurement of Natural Gas,” Trans. ASME, vol. 34, p. 1091.

Chapter 3

Numerical Analysis of Orifice Uncertainties via Computational Fluid Dynamics (CFD) Modeling

Abstract

Flange-tapped concentric orifice meters are commonly used in measurement of shale gas production volumes due to their low cost, accuracy, and ease of maintenance compared to other types of meters. Computational Fluid Dynamics (CFD) models were established to numerically analyze the flow field for an orifice meter and its associated uncertainties, including chemical and organic contamination and solid particle erosion. The base model for the orifice was implemented and validated against experimental data and the same methodology is used to perform parametric studies on the uncertainty effects.

The effect of chemical and organic contamination layer on the orifice plate is studied by changing the length and width of the layer from the upstream or the downstream side of the plate. The results showed the most changes of discharge coefficient occur when the layer is half of the plate length. The results also showed the changes of discharge coefficient increase with the increase in width of the layer.

For the solid particle erosion on the orifice plate, we observed smaller particle sizes would lead to an increase in maximum erosion on the orifice plate while and increase of gas flow rate would also lead to an increase in maximum erosion on the orifice plate. However, the solid particles entering with the measuring fluid will cause minimal erosion to the orifice plate as the erosion rate are negligible.

3.1 Introduction

Orifice meter is one of the most widely used measuring devices for natural gas flow measurements. The most common type of orifice meters uses the flange taps square-edged concentric plates, guided by the AGA Report No. 3. However, the standard equations for orifice measurements were developed implicitly assumes that the velocity profile in the upstream of the orifice is fully developed, symmetric, swirl-free, and turbulent for the orifice meter to measure accurately. It is not always the case as factors such as installation effects, swirl, flow conditioners, chemical and organic contamination, and physical deformation can also affect the discharge coefficient of the orifice and the accuracy of the measurement.

Computational fluid dynamics (CFD) has become a useful tool for analyzing orifice plate by providing detailed flow features. Durst et al. (1989) demonstrated good agreement between their numerical and experimental results for flow through an axisymmetric orifice. Davis and Mattingly (1977) modeled orifice plates with beta ratios ranging from 0.4 to 0.7 and with Reynolds numbers ranging from 10^4 to 10^6. They found good agreement between their computed and experimental discharge coefficient and concluded that CFD have to be considered a feasible complement to theoretical and experimental analyses.

Solid particles erosion has been one of the serious problems in many oil and natural gas applications, as produced oil and natural gas streams typically carry a significant amount of sand along with the flow. Pipe fittings and equipment such as orifice plates, chokes, valves, and sudden contraction/expansions rapidly discharge the fluid resulting in much faster fluid velocities. These types of flow regimes can cause rapid erosion on the equipment as well as the pipe walls, thus lead to inaccurate measurements and safety concerns.

Orifice plate in a pipe can be viewed as flows through restrictions, as thin orifice plate, thick orifice plate, and sudden contraction/expansion are differentiate based on the plate thickness to the plate diameter ratio. Ward-Smith (1979) defines a thin orifice plate with a plate thickness to plate diameter ratio of less than 0.75, whereas a thick orifice plate is in the range of 0.75 to 7. For a restriction with a plate thickness to plate diameter ratio larger than 7, it is considered a sudden contraction/expansion.

The Erosion/Corrosion Research Center (E/CRC) at the University of Tulsa has studied extensively on erosion measurement and its effect in various oil and natural gas applications. They have developed the McLaury's erosion model and also added modifications to improve their erosion models through CFD modeling. Eslinger (2004) focused on understanding and simulating high speed flows through restrictions via CFD modeling. He established CFD models for flows through orifice, flows through sudden expansion/contraction, and flows through safety valves while validated his models with experimental results.

Nemitallah et al. (2014) performed CFD simulations to study the effect of solid particle erosion on the downstream of an orifice using 2% solid particle concentration with water as the particle carrying fluid for carbon steel and aluminum pipes. The rate of erosion and the erosion pattern for the downstream of orifice plate due to the solid particles are investigated through the effect of flow velocity and sand particle size. The results display two erosion peaks in the downstream side of the orifice plat with the first peak occurs in the separation zone right after the vena contracta and the second peak forming in the reattachment region. Increase in the inlet flow velocity will cause an increase in the total erosion rate whereas an increase in particle size would result in a decrease of the total erosion rate.

Araoye (2015) investigated the erosion and flow characteristics for a single orifice plate and double-orifice plate in a serial arrangement with different diameter ratios and orifice spacing. The erosion due to sand particles carried by water is studied through numerical simulations and compared with experimental results. The results showed erosion rates increases as inlet velocity increases; erosion rates also increases when orifice diameter ratio decreases or the sizes of the solid particles decrease.

This study first introduced the methods used to set up and study the orifice plate and its uncertainty factors via CFD modeling. After the models are validated, the first objective is to study the effects of chemical and organic contaminations on the orifice plate. The second objective for this study is to examine the erosion due to these sand particles would affect the orifice plate and its measurement accuracy.

3.2 Methodology

3.2.1 Flow Modeling

The continuous phase of the flow domain is governed by the Reynolds Averaged Navier-Stokes equations (RANS) with the continuity equation (**Equation 3-1**) and the momentum equation (**Equation 3-2**). Since the flow domain is assumed to be isothermal, the energy equation is not taken into consideration.

$$\frac{\partial \rho}{\partial t} + \frac{\partial}{\partial x_i}(\rho \overline{U_i}) = 0 \tag{3-1}$$

$$\frac{\partial}{\partial t}(\rho \overline{U_i}) + \frac{\partial}{\partial x_j}(\rho \overline{U_i}\,\overline{U_j}) = -\frac{\partial p}{\partial x_i} + \frac{\partial}{\partial x_j}\left(\mu \frac{\partial \overline{U_i}}{\partial x_j}\right) - \frac{\partial}{\partial x_j}(\rho \overline{u_i}\,\overline{u_j}) \tag{3-2}$$

The RANS equations comply with the law of conservation of mass and momentum in terms of local-average variables. The left-hand side of the momentum equation represents the change in mean momentum of fluid element and this change is balanced by the isotropic stress due to the mean pressure field, the viscous stresses, the apparent stress due to the fluctuating velocity field, the Reynolds stress. This additional term, the Reynolds stress, which arises from the Reynolds averaging process, is the product of two fluctuating velocity components averaged, then taking the divergent of that term and is unknown for the RANS equations.

To close the equations, Reynolds stress need to be expressed in terms of quantities that are known or modelled. Based on the Boussinesq hypothesis, the Reynolds stress can be related to the mean velocity of gradients of the flow as shown in **Equation 3-3**. The turbulent viscosity or the eddy viscosity, μ_T, is the coefficient of proportionality between the Reynolds stress and the rate of shear. μ_T may be expressed as proportional to the velocity scale (v_o), length scale (l_o), and time scale of turbulence (T_o), where μ_T α $v_o{*}l_o$ or μ_T α l_o^2/T_o.

$$-\rho \overline{u_i}\,\overline{u_j} = \left[\mu_T\left(\frac{\partial \overline{U_i}}{\partial x_j} + \frac{\partial \overline{U_j}}{\partial x_i}\right)\right] - \frac{2}{3}\rho k \delta_{ij} \tag{3-3}$$

Jones and Launder (1972) developed a semi-empirical method of solving for the Reynolds stresses. The Jones and Launder proposed a two-equation model, the standard *k*-*ε* turbulence model, for solving the Reynolds stresses. The turbulent kinetic energy, *k*, and the turbulence dissipation rate, *ε*, are solved by using transport equations for *k* (**Equation 3-4**) and ε (**Equation 3-5**), thus allow μ_T to be solved and close the RANS equations.

$$\frac{\partial(\rho k)}{\partial t} + \frac{\partial(\rho U_j k)}{\partial x_j} = \frac{\partial}{\partial x_j}\left[\left(\mu + \frac{\mu_T}{\sigma_k}\right)\frac{\partial k}{\partial x_j}\right] + P_k - \rho\varepsilon \tag{3-4}$$

$$\frac{\partial(\rho \varepsilon)}{\partial t} + \frac{\partial(\rho U_j \epsilon)}{\partial x_j} = \frac{\partial}{\partial x_j}\left[\left(\mu + \frac{\mu_T}{\sigma_\varepsilon}\right)\frac{\partial \varepsilon}{\partial x_j}\right] + C_{\varepsilon 1}\frac{\varepsilon}{k}P_k - C_{\varepsilon 2}\rho\frac{\varepsilon^2}{k} \tag{3-5}$$

Equation 3-4 has a time derivative and a convection of the turbulent kinetic energy on the left-hand side. On the right-hand side, it has a diffusion term, sources term, and sinks term for the turbulent kinetic energy. The production term, P_k, is the production due to mean velocity shear and is expressed in **Equation 3-6**. The "-*ε*" term shows the equation for *ε* is actually acting to dissipate the turbulent kinetic energy in the flow.

$$P_k = -\rho\overline{u_i u_j}\frac{\partial U_i}{\partial x_j} \tag{3-6}$$

Equation 3-5 is very similar to **Equation 3-4**, as it has a time derivative and a convection term on the left-hand side. On the right-hand side, it also has a diffusion term, sources term, and sinks term. The sources and sinks terms have some empirical constant coefficients, $C_{\varepsilon 1}$ and $C_{\varepsilon 2}$. The constants σ_k and σ_ε are the turbulent Prandtl numbers for *k* and *ε*, respectively. Once the transport equations are solved, can be calculated (**Equation 3-7**), put back, and solve for the Reynolds stress and close the system. C_μ is another empirical constant coefficient. The model constants for the standard k- equations have the values of $C_{\varepsilon 1}$ = 1.44, $C_{\varepsilon 2}$ = 1.92, C_μ = 0.09, σ_k = 1.0, and σ_ε = 1.3.

$$\mu_T = \rho C_\mu \frac{k^2}{\varepsilon} \tag{3-7}$$

3.2.2 Particle Tracking Discrete Phase Model (DPM)

The second step in CFD based erosion modeling is the tracking of the simulated particles. In discrete phase model (DPM) simulations, the continuous phase for the flow field is modeled by the Eulerian method while a second discrete phase for the particle phase is modeled by the Lagrangian method. A fundamental assumption for DPM is that the dispersed second phase occupies a low volume fraction (less than 10-12%).

After the continuous flow field converges, the discrete phase is solved by tracking a large number of particles. In this Eulerian-Lagrangian approach, the discrete and continuous phases are coupled via sources terms in the governing equations. If the particles effect on the fluid is not taken into consideration, the flow analysis is considered to be one-way coupled, as it is a common approach for low particle concentrated slurry flows. The motion equation for the discrete phase particle is solved by the Newton's equation of motion (**Equation 3-8**). The forces acting on the particle in fluid are the drag force (**Equation 3-9**), gravity/buoyancy (**Equation 3-10**), and other forces including virtual mass force, pressure gradient force, Brownian force, and Saffman's lift force.

$$\frac{dV_p}{dt} = F_D + F_G + F_{other} \tag{3-8}$$

$$F_D = \left(\frac{18\mu}{\rho_p d_p^2}\right)\left(\frac{C_D Re_p}{24}\right)\left(U_f - U_p\right) \tag{3-9}$$

$$F_G = g\,\frac{(\rho_p - \rho)}{\rho_p} \tag{3-10}$$

where:

U_p: Particle velocity

U_f: Fluid velocity

F_D: Drag Force

μ: Fluid viscosity

ρ: Fluid density

ρ_p: Particle density

d_p: Particle diameter

C_D: Drag coefficient

Re_p: Particle Reynolds number

The major component of the forces acting on the particle is the drag for that is exerted on the particle by the fluid, as it depends primarily on the local relative velocity between the particle and the fluid. The gravity/buoyancy force is needed when the particles and fluid have significantly different densities and when inclusion for gravitational effects are incorporated.

The virtual mass force accounts for the inertia of the fluid surrounding the particle. It refers to when relative motion between the particles and carrier fluid occurs, fluid in the immediate vicinity of the particle must also move, as a result in resistive force acting on the particle. It is important when $\rho_f > \rho_p$ and is neglected in this research since the particles we are simulating are denser than the carrier fluid. The pressure gradient force is the force due to the pressure gradient of the fluid surrounding the particle due to the acceleration of the fluid. It is typically small and negligible when small pressure gradient prevails in the flow field. The Brownian force is mainly for sub-micron particles, which is also neglected in this research since none of our particles are within the sub-micron range. The Saffman's lift force is the lift due to shear. It is negligible compared to the drag force when the carrier fluid is water or waterlike.

The concept of parcels is also utilized to simulate the particle motion in the flow field, as it is almost impossible to track every single particle within reasonable computational cost and time when the number of particles is quite large. The concept was introduced by Dukowicz (1980), as each parcel are simulated as it contains particles with same properties such as diameter, particle velocity, particle position, and others. The number of particles in each parcel can be viewed as a fractional number to the entire parcel and the behavior of each parcel is determined by the behavior of the particles inside. The application of parcels as clusters of particles can save computational costs tremendously.

3.2.3 Erosion Modeling

After the particles are tracked and solved, particle properties such as particle impingement location, particle impact velocity, and particle impact angle can be then utilized by erosion models to compute the erosion ratio. The erosion ratio is the mass loss of the pipe wall divided by the mass of particles impacting the wall, as it depends on the particle and pipe material properties and impingement information. McLaury (1996) developed a semi-empirical model through his erosion studies focusing on oilfield geometries. His model depends primarily on the particle impact velocity and particle impact angle as shown in **Equation 3-11** where A is based on the target material and its

Brinell Hardness as shown in **Equation 3-12**. **Equation 3-13** and **Equation 3-14** are based on the particle impact angle as *f(α)* represents the impact angle function.

$$ER = AU^n f(\alpha)\dot{m} \quad (3\text{-}11)$$

$$A = F(B_h)^{-0.59} \quad (3\text{-}12)$$

$$f(\alpha) = b\alpha^2 + c\alpha\ ,\ \alpha \leq \alpha_{lim} \quad (3\text{-}13)$$

$$f(\alpha) = x\cos^2(\alpha)\sin(w\alpha) + y\sin^2(\alpha) + z\ ,\ \alpha > \alpha_{lim} \quad (3\text{-}14)$$

where:

$\dot{m}$: Mass flow rate of the particles

f(α): Impact angle function

α: Impact angle

U: Particle impact velocity

A: Empirical constant based on material properties

B_h: Brinell Hardness

n: Velocity exponent (1.73)

n is an empirical constant for the velocity and has been determined through many sets of experimental data that an *n* value of 1.73 provides accurate results for a large variety of materials including steel. *b*, *c*, *w*, *x*, *y*, and *z* are constants for the impact angle function which depends on the materials being eroded. **Table 3-1** provides the empirical constants for carbon steel and aluminum.

Table **3-1** Empirical Constants for Erosion Equations (McLaury 1996)

Material	Carbon Steel	Aluminum
A	$1559\text{x}BH^{-0.59}$	$2.388\text{x}10^{-7}$

α	15 degrees	10 degrees
b	-3.84×10^{-8}	-34.79
c	2.27×10^{-8}	12.3
w	1.0	5.205
x	3.147×10^{-9}	0.147
y	3.609×10^{-10}	-0.745
z	2.532×10^{-9}	1.0

3.2.4 Model Validations

Orifice CFD Model Validations

To validate our orifice models, we compared the results from our CFD models with the experimental works done by DeOtte et al. (1991) and Morrison et al. (1993) in **Figure 3-1**, **Figure 3-2**, and **Figure 3-3**.

As we plotted our results from the 2-D asymmetrical and 3-D models versus DeOtte's experimental results, they are in good agreements for most of the data points along the centerline of the pipe. However, the region after the vena contracta and before the velocity profiles finally reattached to the pipe wall shows large disagreements (up to 33% differences), as the reattachment region ranges from z/R=1 to z/R=8.5. The k-epsilon model as previously studied by Durst and Wang (1989) for Orifice meter modeling does not match the experimental results (1988) perfectly as it tends to overshoot the velocity, especially in the downstream plate after the vena contracta as the flow is in the process of reattaching to the pipe wall. In addition, because we are using a RANS instead of the true

Navier-Stokes equations for turbulent flows, which also introduces the discrepancy between the numerical models and the laboratory works.

The comparison between our 2D and 3D models clearly showed the 3D model being more accurate in terms of velocity profiles prediction as compared with the experimental results, especially in the reattachment region. This improvement in accuracy was expected, as the 3D model should capture more defined profiles for numerical simulations. However, the computational time for running the 3D model is much more expansive the 2D model.

The next sets of data we compared are the pressure distributions for the 3D model with DeOtte's (**Figure 3-2**) and Morrison's (1993) (**Figure 3-3**) experimental results. The results for both pressure distributions showed good agreements with the experimental results as shown in the plots.

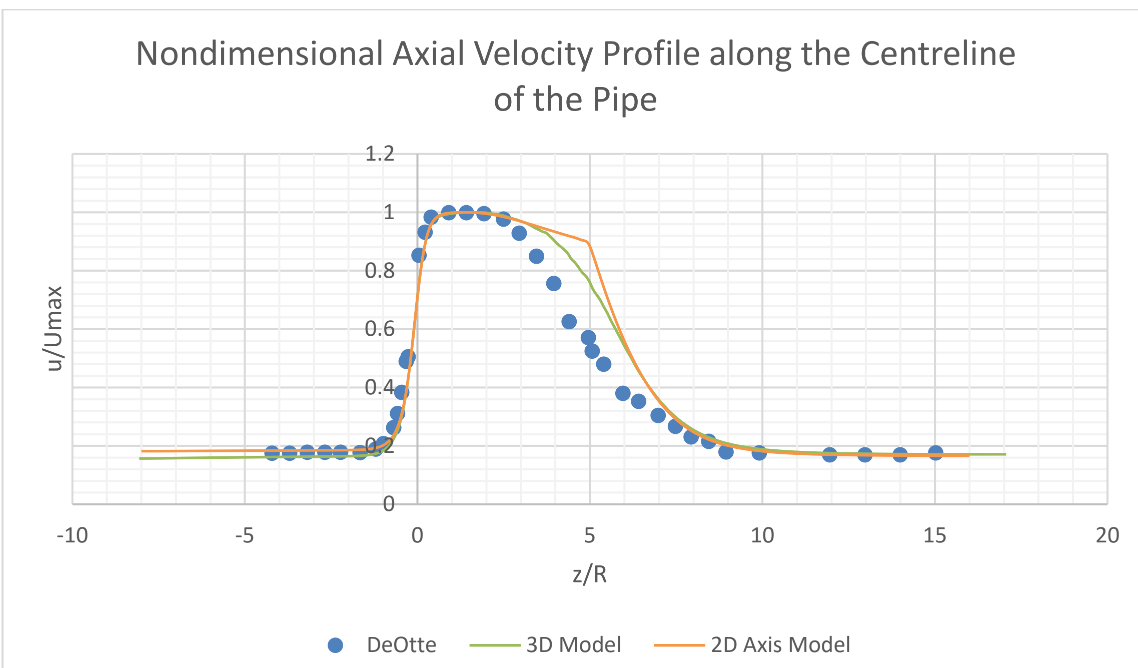

Figure **3-1** Nondimensional Axial Velocity Profiles

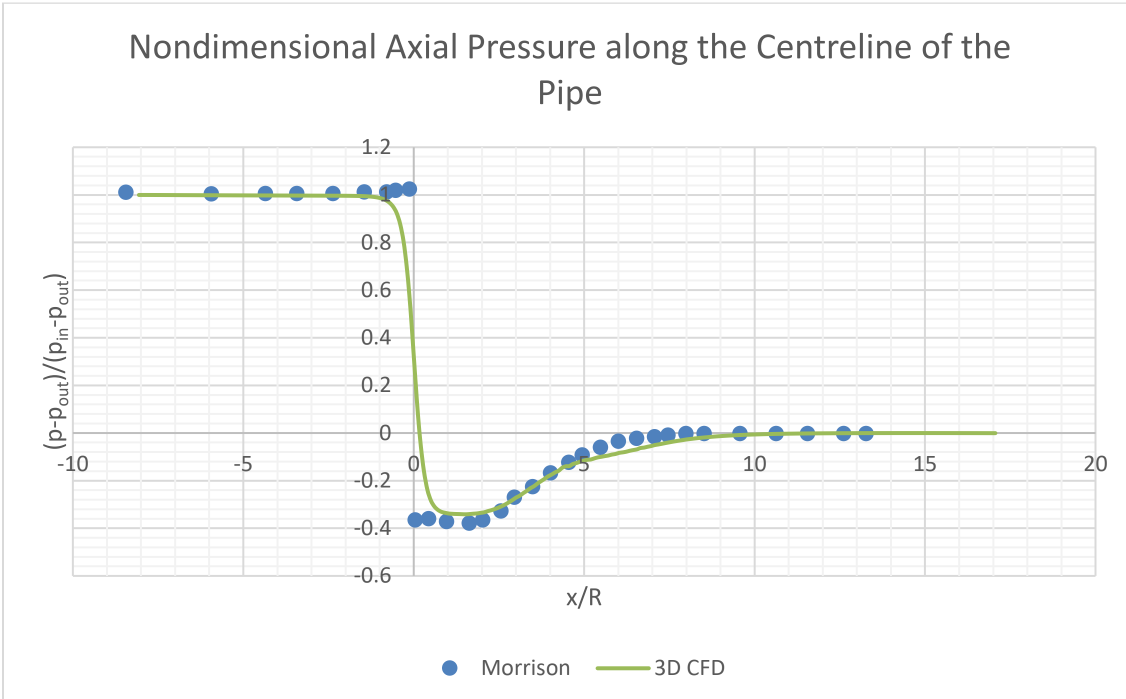

Figure **3-2** Nondimensionalized Axial Pressure Distribution

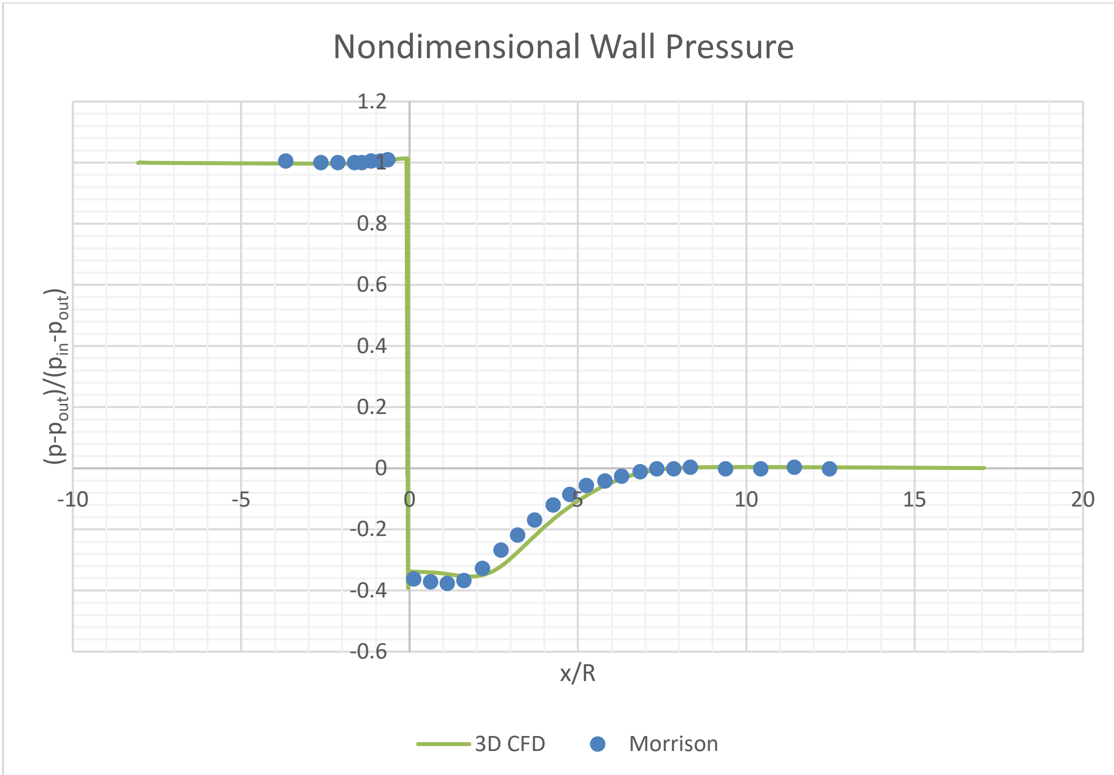

Figure **3-3** Nondimensionalized Wall Pressure Distribution

We have also compared the radial profiles of the axial velocities (**Figure 3-4**) and the radial profiles of the radial velocities (**Figure 3-5**) with DeOtte's experimental results. We plotted the radial profiles from different radial locations from both the upstream and downstream of the orifice. Overall, the numerical results displayed good agreements with the experimental data. However, the results for both pressure distributions showed good agreements with the experimental results as shown in the plots.

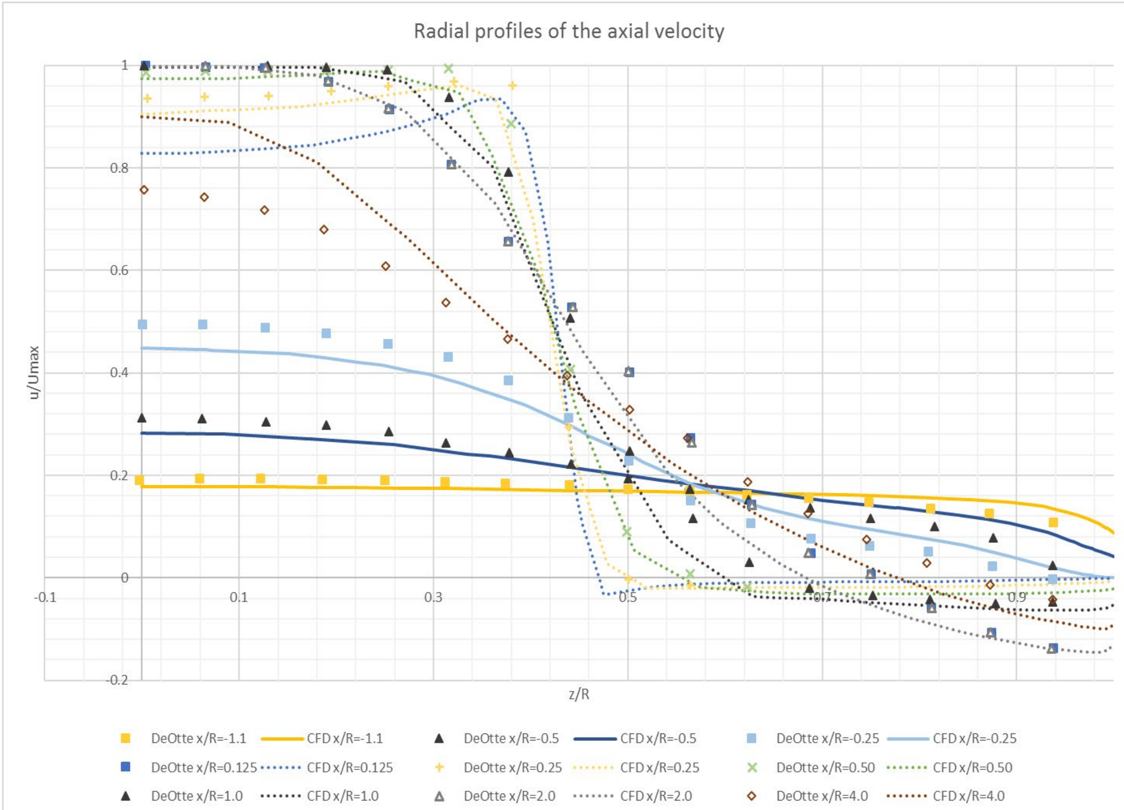

Figure **3-4** Nondimensionalized Radial Profiles of the Axial Velocity

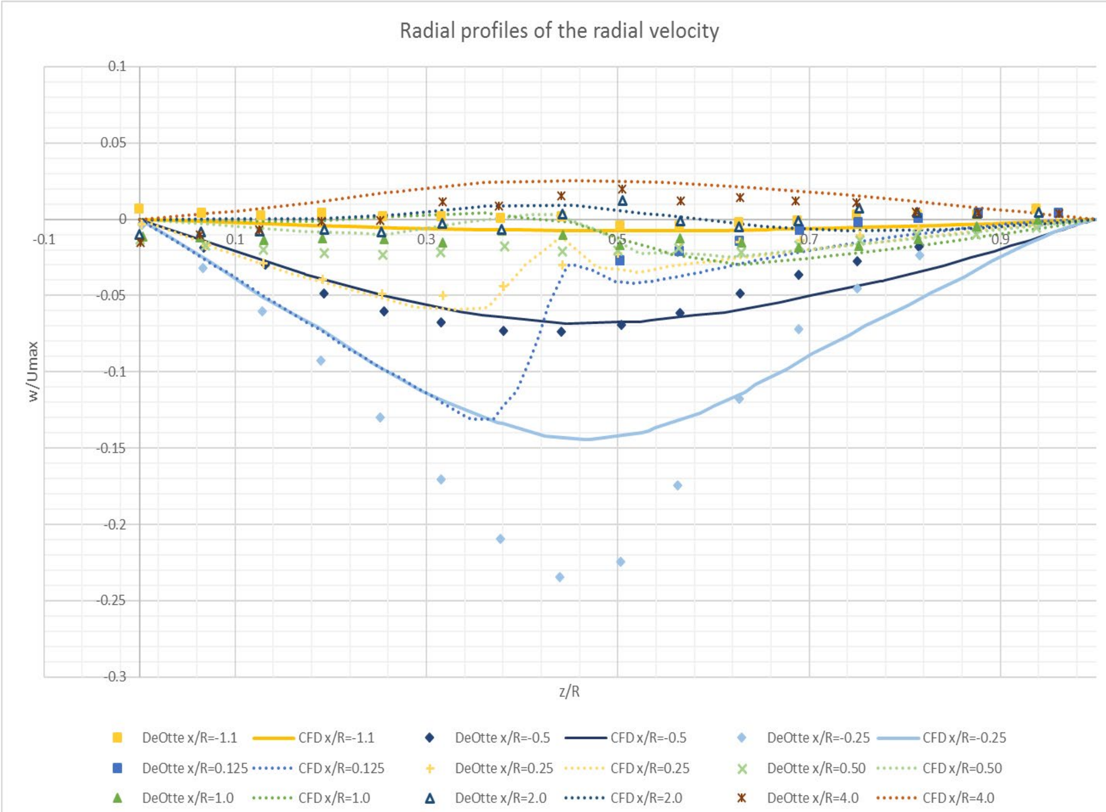

Figure **3-5** Nondimensionalized Radial Profiles of the Radial Velocity

The final step for the validation of our models is to produce the discharge coefficients of our models and compare with the discharge coefficients, C_d, provided by the ANSI from experimental works done by Whetstone et al. (1988) and the discharge coefficient equations developed empirically by Reader-Harris. **Table 3-2** provides the results and comparison of the C_d values from ANSI standard versus the experimental and numerical simulation results from Nail (1991), and also our numerical simulation results. Both of the experimental and numerical results from Nail underpredicts the C_d value by quite a margin, whereas our model provides a more accurate result of the C_d value as shown.

Table **3-2**: Discharge Coefficient Values

	ANSI Standard	Experiment (Nail, 1991)	FLUENT (Nail, 1991)	COMSOL (Zhang, 2017)
C_d	0.611	0.565	0.548	0.6209
Percent Difference	-	-7.53%	-10.3%	1.62%

Overall, we can conclude the validation of our CFD models as they are able to match the results from experimental studies using the same setups. We can proceed and implement the models using our base model dimension.

Erosion CFD Model Validations

Single-phase flow in sudden expansion type of flow geometries were considered in order to ensure the accuracy of the CFD erosion prediction for a single-phase flow. Two experimental data works were considered in this research.

Blatt et al. (1989) performed their experimental erosion study of flow in a sudden pipe contraction with 0.5 diameter ratio. The sand particles in their study have diameter of 400 μm with a concentration of 0.1% by volume while the carrier fluid was water at 60°C. The diameter of the contraction is 25 *mm* with a length of 100 *mm*. The length of the upstream pipe is 500 *mm* and the length of the downstream pipe is 350 *mm*. The local penetration rate in *mm/year* was plotted and compared with our CFD model's results using the same setup as shown in **Figure 3-6** over different inlet velocities of 1 *m/s*, 2.5 *m/s*, 3.5 *m/s*, 4.5 *m/s*, and 5.7 *m/s*. The figure shows good agreements over the entire velocity range.

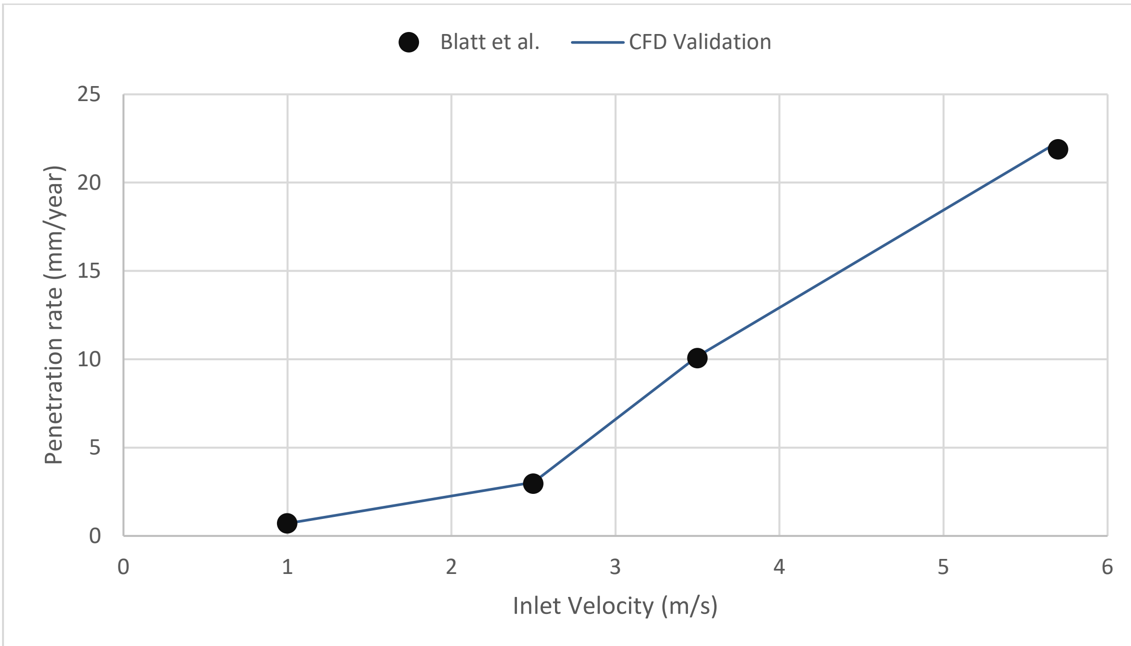

Figure **3-6** Comparison between CFD erosion model results and the experimental data of Blatt et al. (1989)

Zhang et al. (2016) performed their experimental study for a sudden contraction/expansion flow geometry using water to carry sharp silica flour with average diameter of 25 μm. They used wafers with thickness of 0.25 *inch* to setup as their pipes and measured the local mass loss after the experiments. The water has a flow rate of 26 *GPM* (average inlet velocity of 10.24 *m/s* and throat velocity of 23.05 *m/s*) with testing time of 150 *hours* while maintain a silica sands concentration of 1% (about 0.016 *kg/s* sand flow rate). The diameter of the upstream and downstream pipe is 0.5625 *inch* while the contraction diameter is 0.375 *inch*. The length of the upstream is 5.75 *inch* and 15 *inch*, respectively, while the contraction throat length is 7.5 *inch*. Comparison between their experimental data and our CFD model using the same setup are plotted and displayed in **Figure 3-7**. Overall, the figure shows good agreements throughout the sections of the flow geometry and ensure the accuracy of the CFD model for erosion predictions.

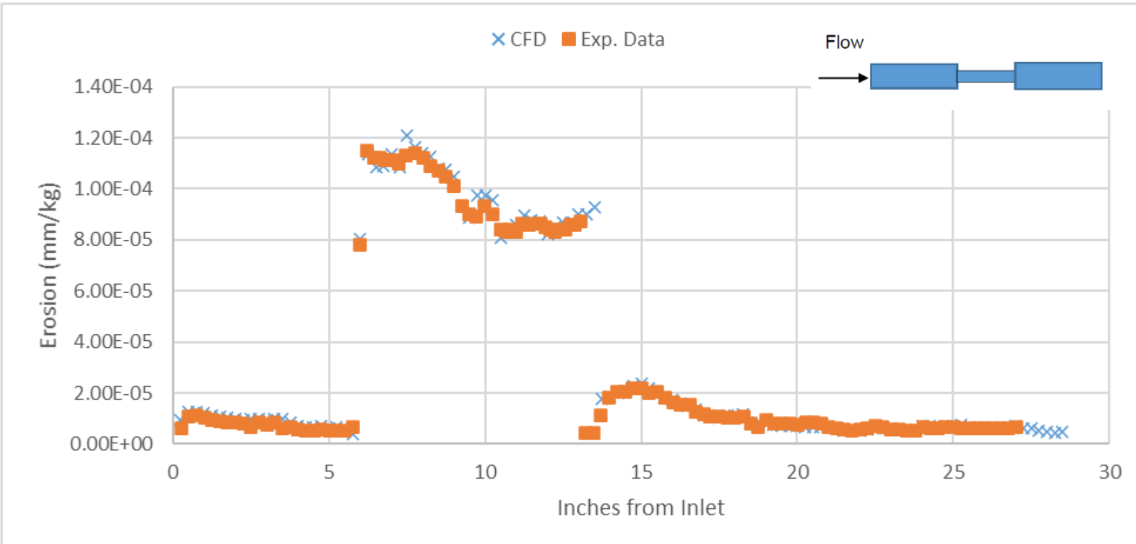

Figure **3-7** Comparison between CFD erosion model results and the experimental data of Zhang et al. (2016)

3.2.5 CFD Models Setup for Orifice Numerical Analysis

The orifice meter CFD model will start out as a 2-D axisymmetric model. The dimension of our model is a cylindrical pipe with an Orifice plate's center point set at the origin of the axis with upstream in the negative *z* direction and downstream in the positive z direction. The inner diameter of the pipe is 2 *in* and the diameter of the Orifice plate is 1 inch, which gives a beta ratio of 0.5. The thickness of the Orifice plate is 0.126 *in* with a

45° bevel. The flowing fluid is air at 110°*F* with a Reynolds numbers of 54,700. The inlet velocity profile is fully developed in that the radial velocity was zero without any swirl. The upstream pipe length is set at 4*D* and the downstream pipe length is set at 8*D*. The meshes are created using free triangular consist of 45,553 number of elements. The total number of degrees of freedom to solve for is 125,255. The parameters for the base model are summarized in **Table 3-3**.

Table **3-3** Data for Base Case (100712472)

Differential Pressure in inch of Water (*in*)	144.36
Flowing Pressure (*psia*)	1,197.03
Flow Temperature (°*F*)	68.31
Flow Hours (*hr*)	24
Meter Tube Internal Diameter (*in*)	4.026
Orifice Plate Bore Diameter (*in*)	2
Real Gas Relative Density	0.5701
Gas Density (lb_m/ft^3)	4.0882
Gas Density (lb_m/gal)	0.5465
Gas Viscosity (*cp*)	0.0132
Reynolds Number	3,136,516.29
Gas Volume (*Mcf/hr*)	496.43
Gas Volume (*Mcf/Day*)	11,914.37

We will be studying a stationary model since the flow is steady state without any swirl. **Figure 3-8** provides the velocity profile from upstream to downstream in the *r-z* plane in 2-D. **Figure 3-9** provides the velocity profiles for the cylindrical axisymmetric model in 3-D view. **Figure 3-10** provides the map for the velocity streamlines.

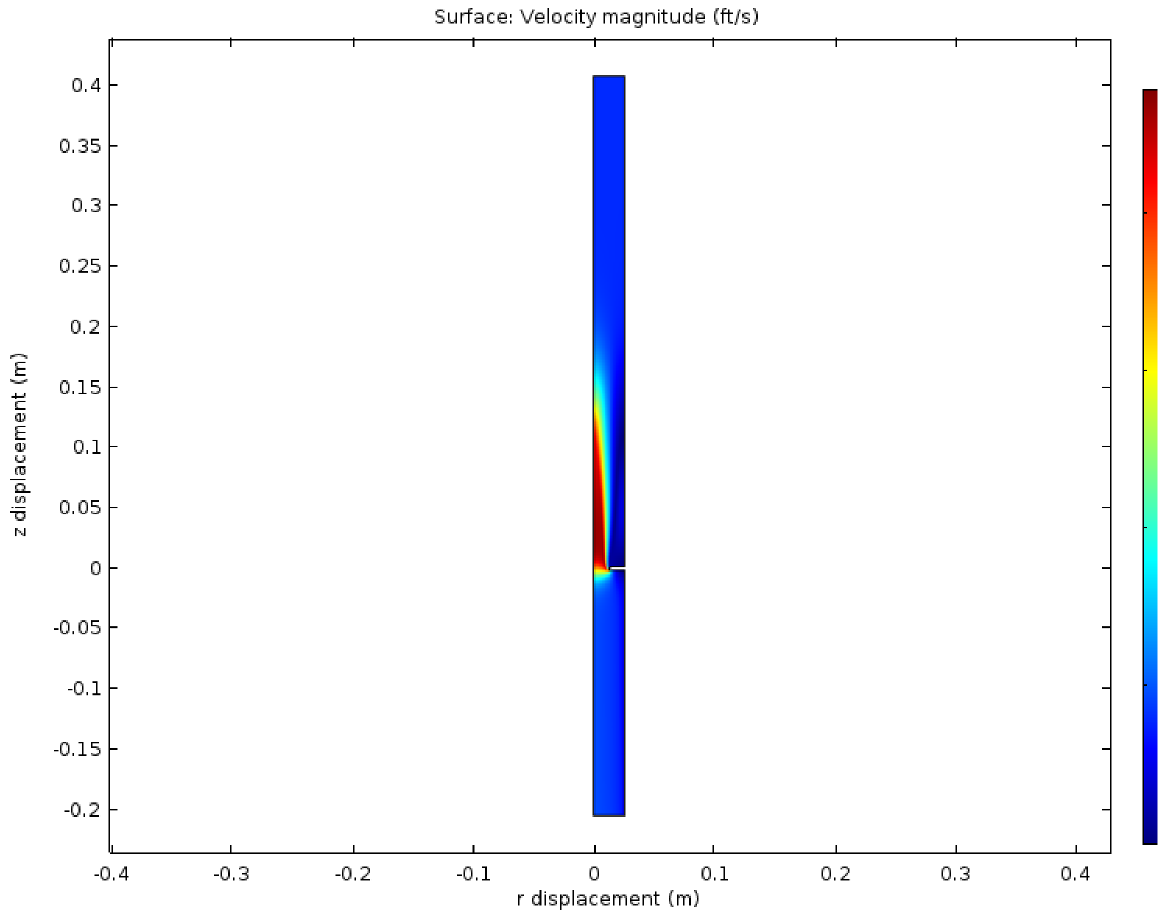

Figure **3-8** Velocity surface profile

Figure 3-8 displays the velocity map in the *r-z* plane. Since the model is axisymmetric, in the cut plane view in 2-D, the other half of the velocity map (not shown) is symmetrical in the *r*-direction. From the velocity map, we can observe that the velocity picks up rapidly as the fluid approaches the Orifice plate with the velocity along the centerline of the pipe reaches its maximum of 233.77 *ft/s* at z/R=1.0, z is the displacement along the z direction and R is the inner radius of the pipe. The velocity eventually settles back down and reattach to the wall of the pipe at z/R=9.0. The location of the vena contracta, which is where the velocity reaches its maximum, is in agreement with the experimental work done by DeOtte et. al. (1991) using the same setup as the model.

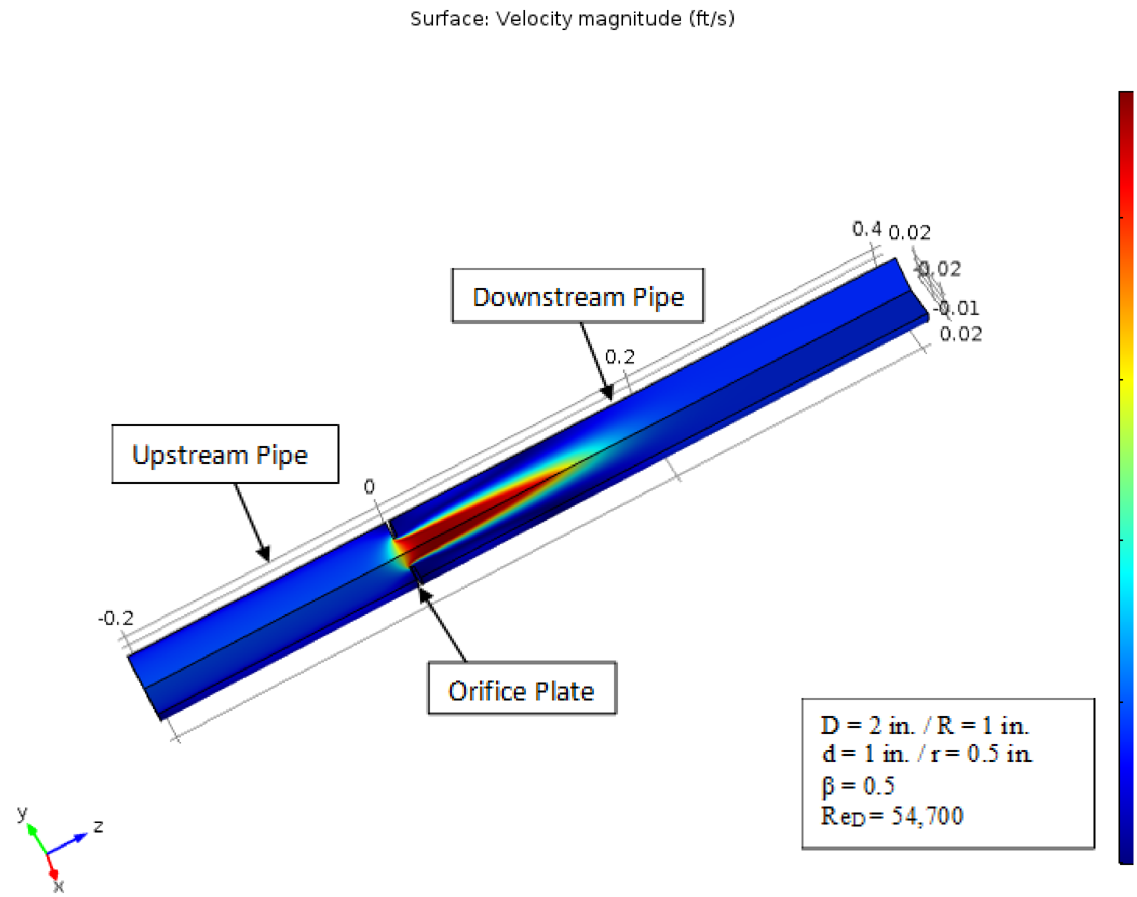

Figure **3-9** 3-D Velocity profile

Figure 3-9 provides the 3-D view of the velocity map for the pipe and the Orifice plate, with the identifications of the upstream pipe, the downstream pipe, and the Orifice plate set at the origin of the axis. Due to the assumptions of the fluids entering the pipe, which is steady state, turbulent, and incompressible flow without any swirls, the velocity profile is axisymmetric along the centerline of the pipe as indicated in this 3-D view.

The CFD model can provide us with further analysis of Orifice metering as we change the dimensions of the geometry, the properties of the fluids, as well as the boundary conditions (inlet velocity and wall functions). We can also analyze key features that would influence the flow measurement, including erosion, wax precipitation, bending of the plate, swirl, composition of gas, eccentricity of the plate, etc. These analyses will give us a better understanding of the orifice metering system, such as providing insights on how to account for particular effects affecting the flowing conditions.

We have also developed a 3-D finite element model using the same dimensions (**Figure 3-12**) as the previous 2-D asymmetrical model. The turbulence gas flow is simulated using air by incorporating the Reynolds-averaged Navier-Stokes equations (RANS) with the k-epsilon turbulence model. Since the flow is without any disturbance for our base case, we can further simplify the 3-D model to a 3-D asymmetrical model as shown in **Figure 3-11**. The inner tube diameter of the pipe is 2 *in* and the bore diameter of the orifice plate is 1 *in*, thus give a beta ratio of 0.5. The thickness of the orifice plate is 0.126 *in* with the upstream pipe length of 8 *in* and the downstream pipe length of 17 *inch* A pipe Reynolds number of 54,700 defines the inlet flow of the air at a temperature of 110°*F*.

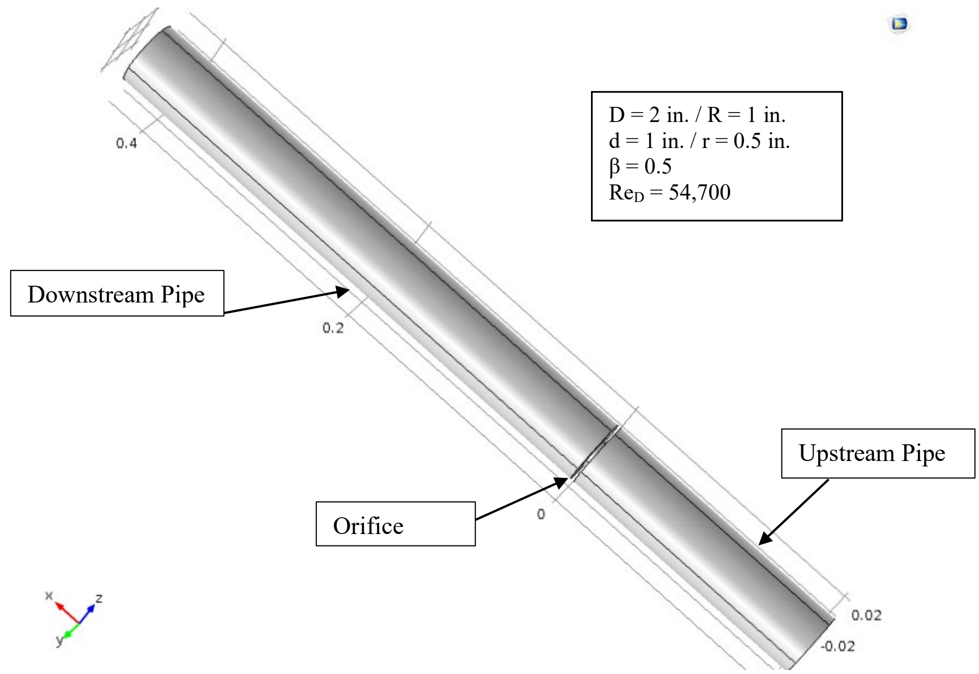

Figure **3-10** Geometry of the 3-D Orifice Model

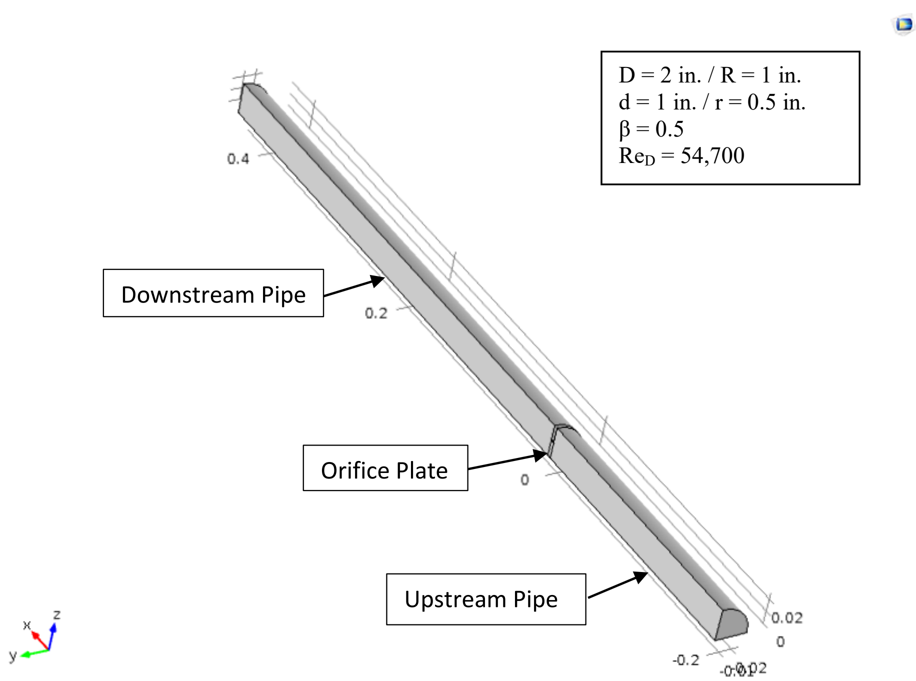

Figure **3-11** Geometry of the 3-D Asymmetrical Orifice Model

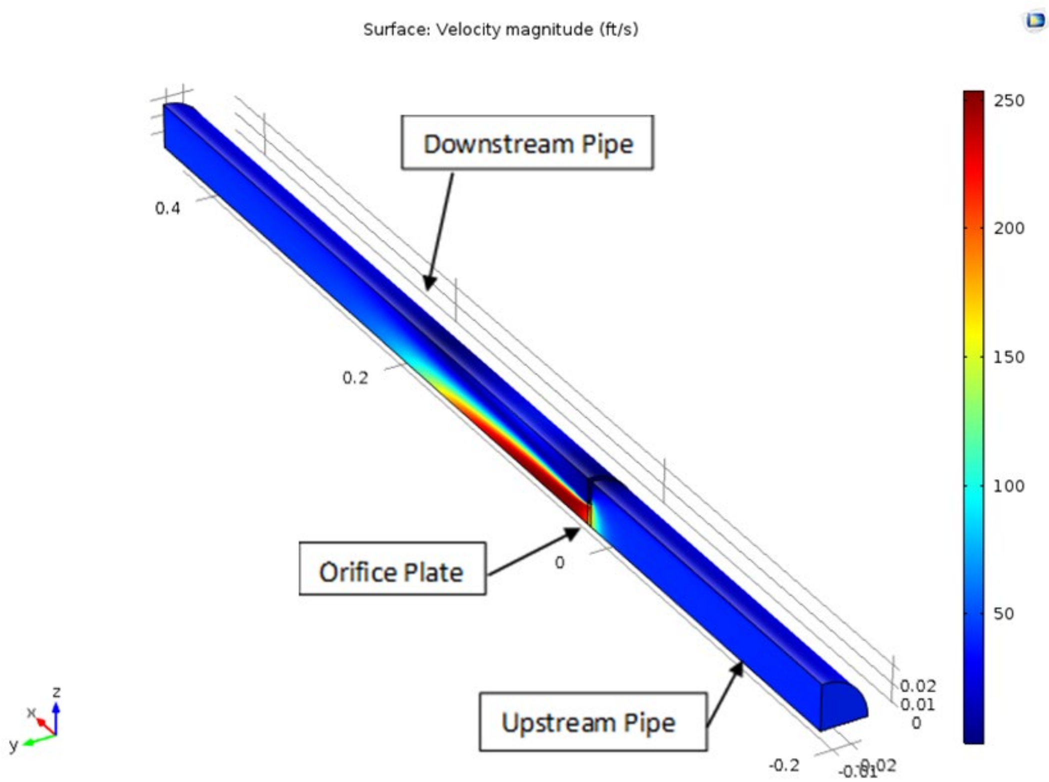

Figure **3-12** Orifice 3-D Velocity Profile

3.3 Parametric Studies

The AGA-3 equation and the Reader-Harris/Gallagher equation were developed implicitly assumes that the velocity profile in the upstream of the orifice is fully developed, symmetric, swirl-free, and turbulent for the orifice meter to measure accurately. However, this is not always the case for the field measurement as different factors can affect the flow profile and the “pureness” of the flowing gas, which could possibly affect the accuracy of the orifice measurement. Extensive numerical studies via CFD modeling on different factors are analyzed in each of following sections as how each factor would affect the discharge coefficient.

3.3.1 Numerical Analysis of Chemical and Organic Contamination

The flowing fluids, such as oil, grease, pipeline sludge or other liquids or solids, can contaminate orifice plates. The accumulation of such contaminates can also build up flow restrictions inside the pipe and on the orifice plate, which would create additional pressure drop for the flowing fluid.

Model Setup

To simulate the effects of contamination to the orifice plate, we setup our orifice CFD model with an additional layer with two parameters of deposition height and deposition width with their lengths based on percentage of the orifice plate diameter, d, and orifice plate thickness, t_p, respectively. The deposition layer on the orifice plate due to contamination can be simulated either from the upstream side (**Figure 3-11**) or the downstream side (**Figure 3-12**) of the orifice plate and its setup.

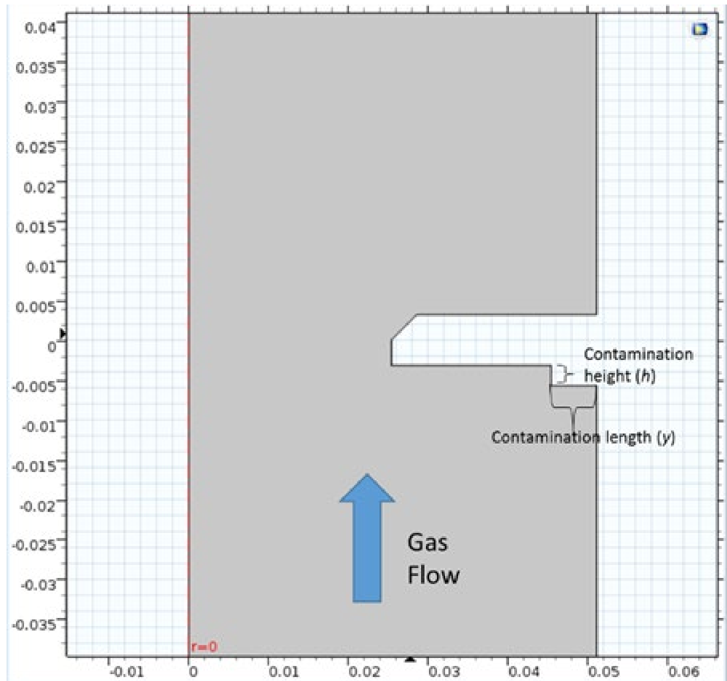

Figure **3-11** Contamination of the orifice plate from the upstream side.

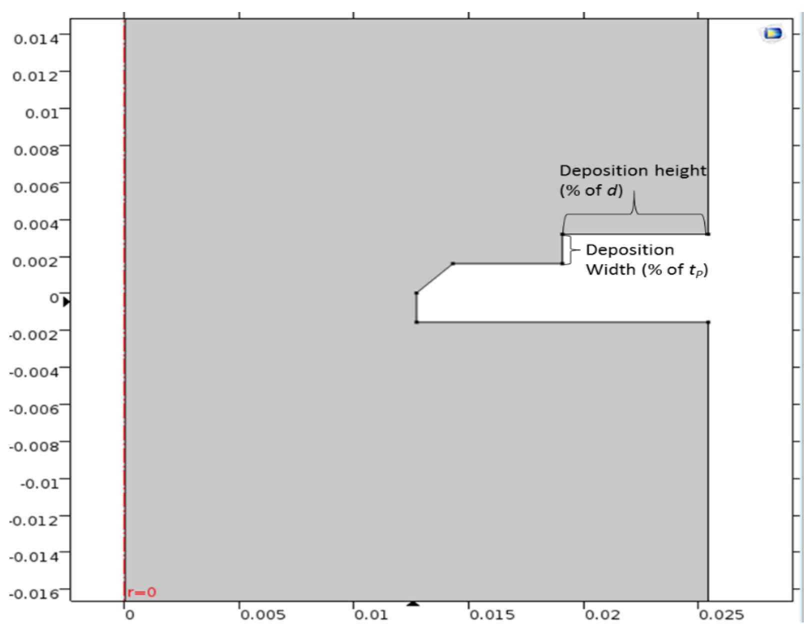

Figure **3-12** Contamination of the orifice plate from the downstream side.

Results and Discussion

Parametric studies based on the change of the length of the deposition layer and the change of the width of the deposition layer are performed and compared with the base model (no deposition layer). We kept the width of the layer constant while changing the length to 10%, 25%, and 50% of d. Similarly, we kept the length of the layer constant while changing the width to 10%, 50%, 100%, 200%, and 300% of t_p. Also keep in mind these simulations are ran in axisymmetric settings, implying that the other half of the orifice plate would have the exact same deposition layer from contamination.

We extracted the results based on different settings of the deposition layer and compared the C_d with the base model's C_d. The results are shown in **Table 3-4** for upstream deposition and **Table 3-5** for downstream deposition.

Table **3-4**: Coefficients of Discharge for Upstream Contamination

Upstream Contamination	C_d	**% Change in** C_d
No Contamination	0.6161	
10% d, 10% t_P	0.6156	-0.08%
25% d, 10% t_P	0.616	-0.02%
50% d, 10% t_P	0.6151	-0.16%
10% d, 50% t_P	0.6157	-0.06%
25% d, 50% t_P	0.6186	0.41%
50% d, 50% t_P	0.6174	0.21%
10% d, 100% t_P	0.6161	0.00%
25% d, 100% t_P	0.6266	1.70%
50% d, 100% t_P	0.6209	0.78%

10% d, 200% t_P	0.6192	0.50%
10% d, 300% t_P	0.6246	1.38%

Table **3-5**: Coefficients of Discharge for Downstream Contamination

Downstream Contamination	C_d	**% Change in** C_d
No Contamination	0.6161	
10% d, 10% t_P	0.6157	-0.06%
25% d, 10% t_P	0.616	-0.02%
50% d, 10% t_P	0.6159	-0.03%
10% d, 50% t_P	0.6156	-0.08%
25% d, 50% t_P	0.6155	-0.10%
50% d, 50% t_P	0.6159	-0.03%
10% d, 100% t_P	0.6159	-0.03%
25% d, 100% t_P	0.6162	0.02%
50% d, 100% t_P	0.6166	0.08%
10% d, 200% t_P	0.6161	0.00%
10% d, 300% t_P	0.6161	0.00%

As we can see from the results, contamination to the upstream side of the orifice plate has more effect to the C_d as compared to the downstream contamination. We observed that as width of the deposition layer increases, the magnitude of the change in C_d increases, thus leads to a larger error in terms of measurement accuracy. We also observed for the changes in length of the deposition layer, 25% of d has the most magnitude of change in C_d, followed by 50% of d while 10% d has much less of an effect until the width of the layer doubles (200%) or triples (300%). Visually, 25% of d implies that the contamination layer is covering half the orifice plate while 50% of *d* implies that the contamination layer is covering the whole orifice plate.

3.3.2 Analysis of Orifice Erosion via CFD Modeling

Even with most of the sand of the gas stream being filtered out, there still is the possibility of fine sand particles that leaked through the filters while carried by the sand streams entering the orifice section.

Model Setup

To investigate the effects of "leaked" sand particles carried by the produced gas, we set up our orifice erosion model with data from operating gas well in Marcellus shales. The "leaked" sand particles simply imply the few particles that did not get filtered and carried by the clean gas to the next stage, since it is almost impossible to filter every sand particle from the produced gas. **Figure 3-13** shows the geometry of the model while the data for the model is presented in **Table 3-6**.

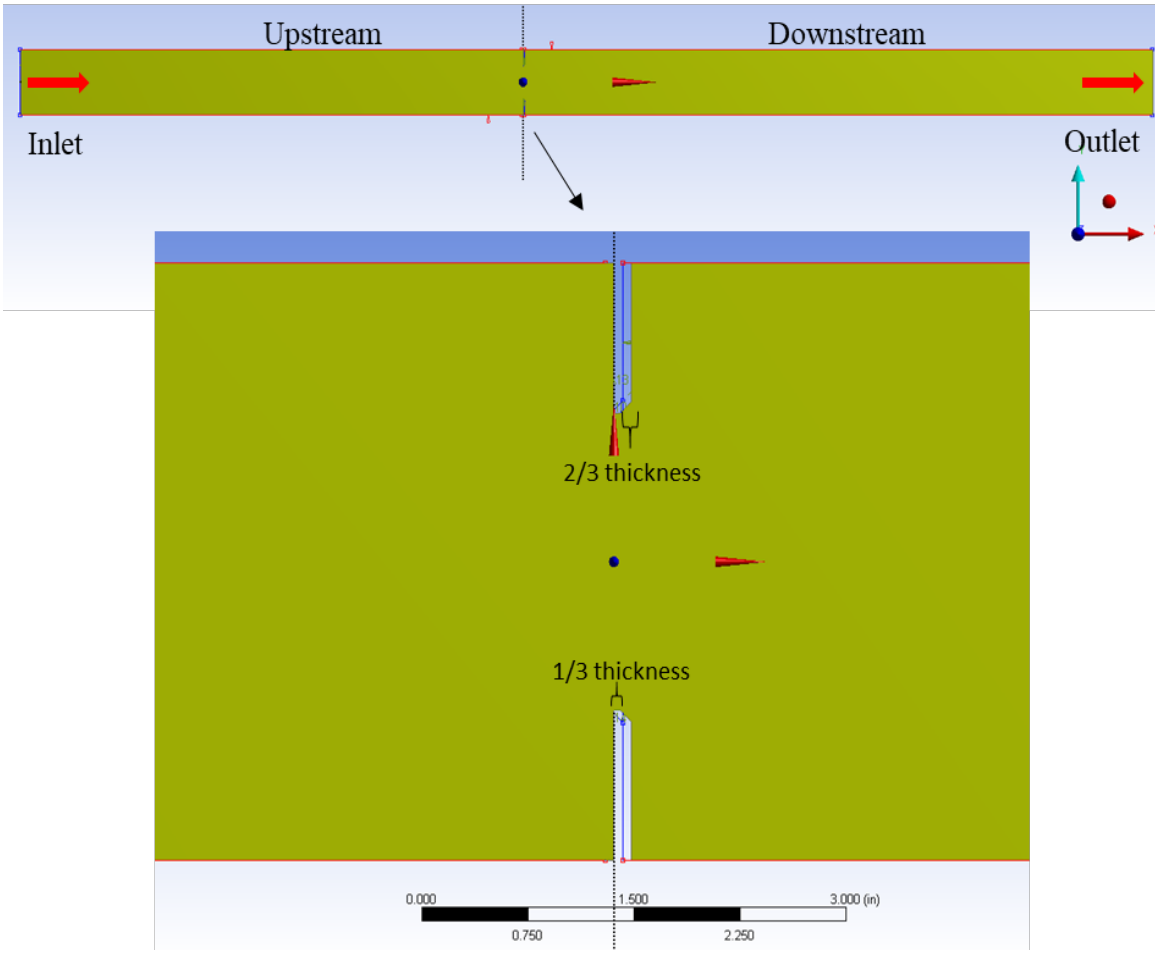

Figure **3-13** Orifice Erosion CFD Model Setup.

Table **3-6** Data for Base Case (100712472)

Differential Pressure in inch of Water (*in*)	144.36
Flowing Pressure (*psia*)	1,197.03
Flow Temperature (°*F*)	68.31
Flow Hours (*hr*)	24
Meter Tube Internal Diameter (*in*)	4.026
Orifice Plate Bore Diameter (*in*)	2
Orifice Plate thickness (*in*)	0.125

Real Gas Relative Density	0.5701
Gas Density (lb_m/ft^3)	4.0882
Gas Density (lb_m/gal)	0.5465
Gas Viscosity (*cp*)	0.0132
Reynolds Number	3,136,516.29
Gas Volume (*Mcf/hr*)	496.43
Gas Volume (*Mcf/Day*)	11,914.37
Inlet Velocity (*ft/s*)	78.74
Particles	Silica Sand
Particles Density (lb_m/ft^3)	165
Number of Particles	100
Particles Size (*Mesh*)	100

The clean gas is flowing through the pipe with an orifice meter after the produced gas are filtered. The meter tube internal diameter is 4.026 *in* and the orifice plate bore diameter is 2 *in*, thus gives a 0.497β. The orifice plate is setup with a sharp-edged while having a plate thickness of 0.125 *inch* The sharp edge section of the plate is one-third of the plate thickness while the bevel section of the plate is the other two-third of the plate thickness in a 45° angle. For the orifice meter tube set up, the upstream pipe length is 8*D* while the downstream pipe length is 10*D*. We simulated 100 sand particles and injected them throughout the inlet section of the orifice meter.

For the base case, the gas flowing rate is 496.43 *Mcf/hr* with a density of 4.0882 lb_m/ft^3 and a viscosity of 0.0132 *cp*. The flowing pressure is 1,197.03 *psia* and the flowing temperature is 68.31°*F*. The Reynolds number of the flowing fluid is 3,136,516.29. The sand particles are silica sand with density of 165 lb_m/ft^3. The total simulation time is set as 24 *hr*.

The particles interactions for the pipe wall boundary are set as *reflect* and *escape* for the outlets. The model is simulated with standard *k*-*ε* model as the turbulence model while Lagrangian DPM tracking method is utilized to track the particles and calculate the particle impingement information. The erosion ratios are calculated using the McLaury's erosion model. Gravity is neglected for this model.

Results and Discussion

After the model is validated, we performed parametric studies to examine the erosion effects of sand particle sizes. The base model has 100 silica sand particles of 100*M* carried by the clean gas with a flowing rate of 496.34 *Mcf/hr*. Maximum erosion rate on the orifice bore diameter from the upstream side will be closely examined.

Particle Size

We first performed parametric study to examine the erosion effects of particle mesh size on the orifice bore plate. We changed the mesh size of the particles from the base case to 20*M*, 40*M*, and 70*M* while keeping other parameters the same. We plotted the maximum erosion rate on the orifice bore plate relative to the mesh sizes as shown in **Figure 3-14**.

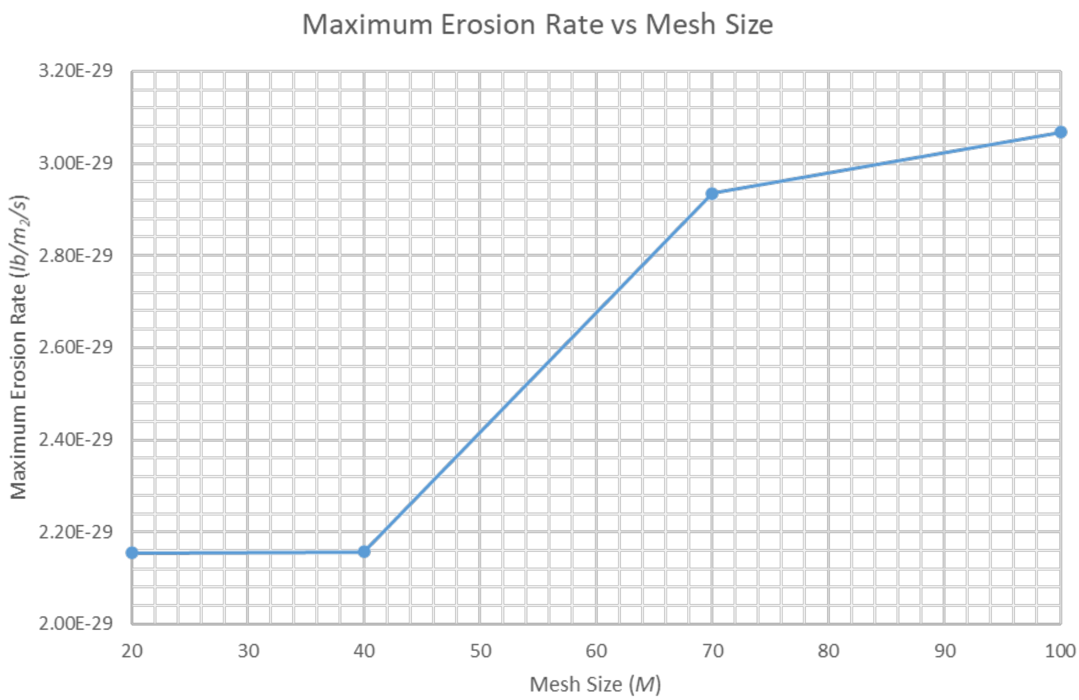

Figure **3-14** Effects of Mesh Size

We expect the effects of particle size to be that an increase in particle size would result a decrease in erosion rate. From **Figure 3-14**, we observed that the higher the mesh size would lead to a larger maximum erosion rate on the orifice bore diameter which agrees with what we expected. Since the particle concentration is the same while average number of particles per unit volume of fluid is much higher in the case for smaller particles. For smaller size particles, the number of impacts at a given location is significantly larger than larger size particles. The larger number of impacts causes higher erosion rate. Small size particles also have large surface area per unit mass, which will make their motion more influenced by the fluid motion. However, the magnitude of the maximum erosion rate is negligible for all mesh sizes.

Gas Flow Rate

We performed parametric study to examine the erosion effects of gas flowrate on the orifice bore plate. We changed the gas flowrate to a low flowrate case of 500 *Mcf/day* and a medium flowrate case of 1,000 *Mcf/day*, whereas our base case has a high flowrate case of 11,914 *Mcf/day*. For this parametric study however, we examined the effects of gas flowrates for different particle sizes of 1 μm, 10 μm, 100 μm, and 300 μm. We plotted the maximum erosion rate on the orifice bore plate relative to the gas flowrate as shown in **Figure 3-15** for 1 μm, **Figure 3-16** for 10 μm, **Figure 3-17** for 100 μm, and **Figure 3-18** for 300 μm.

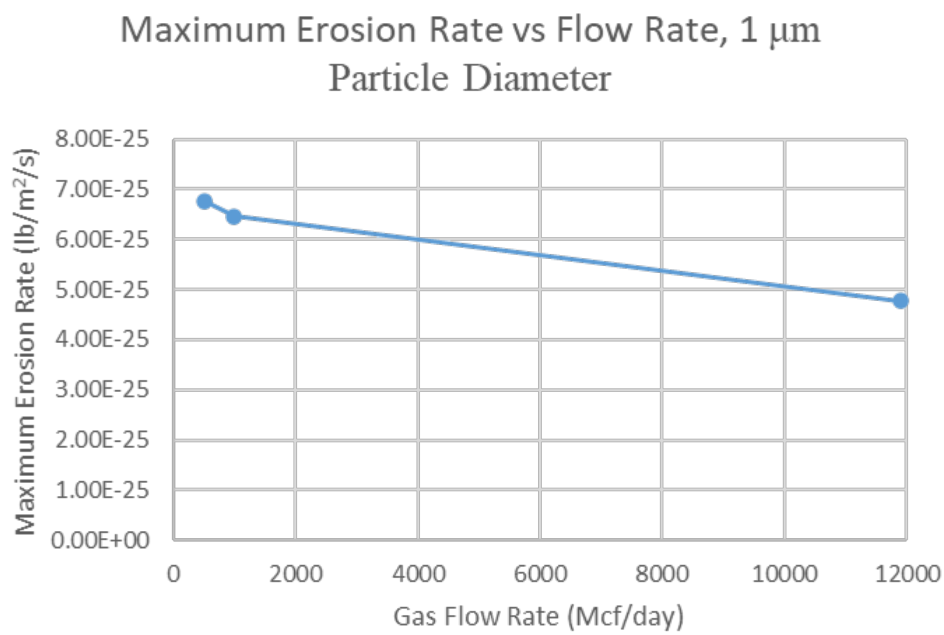

Figure **3-15** Effects of Gas Flow Rate for 1 μm Sand Particles

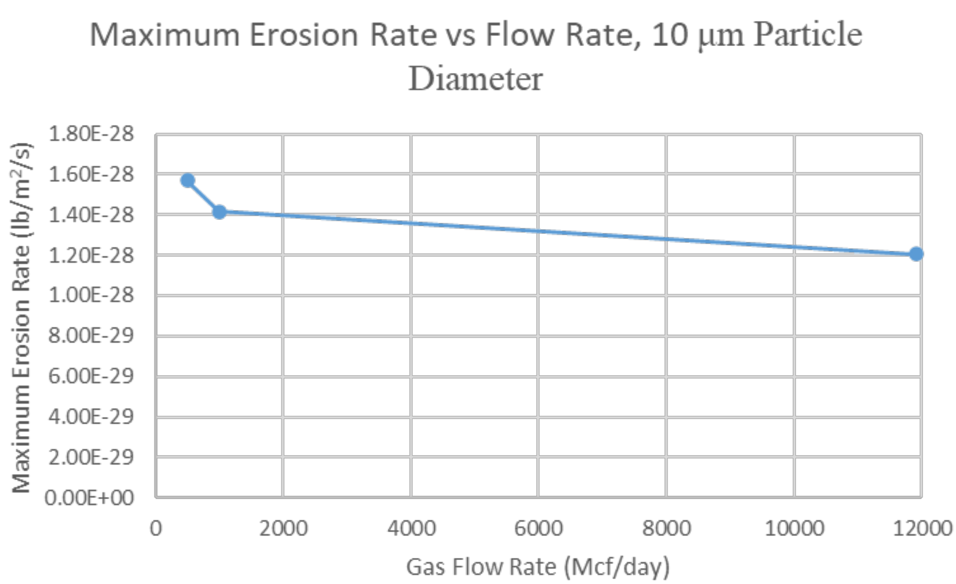

Figure **3-16** Effects of Gas Flow Rate for 10 μm Sand Particles

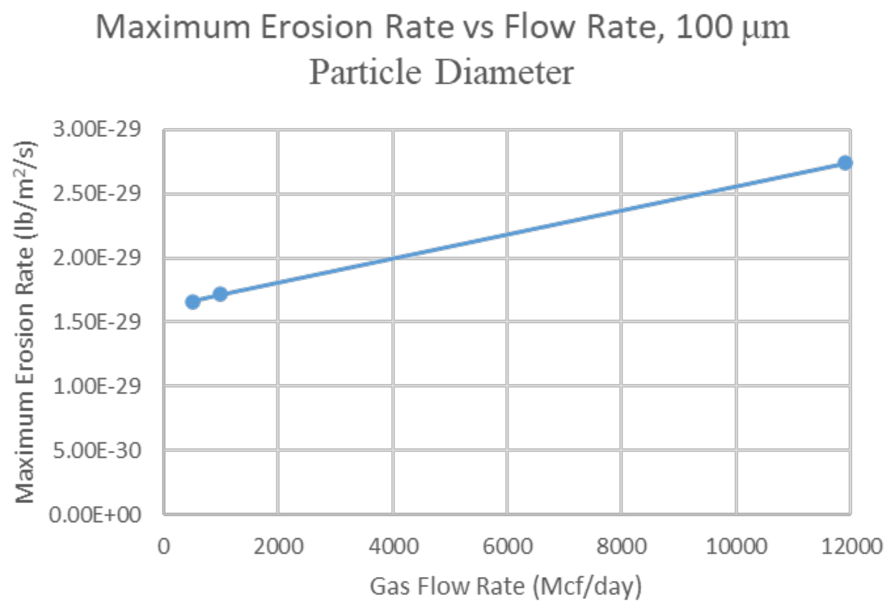

Figure **3-17** Effects of Gas Flow Rate for 100 μm Sand Particles

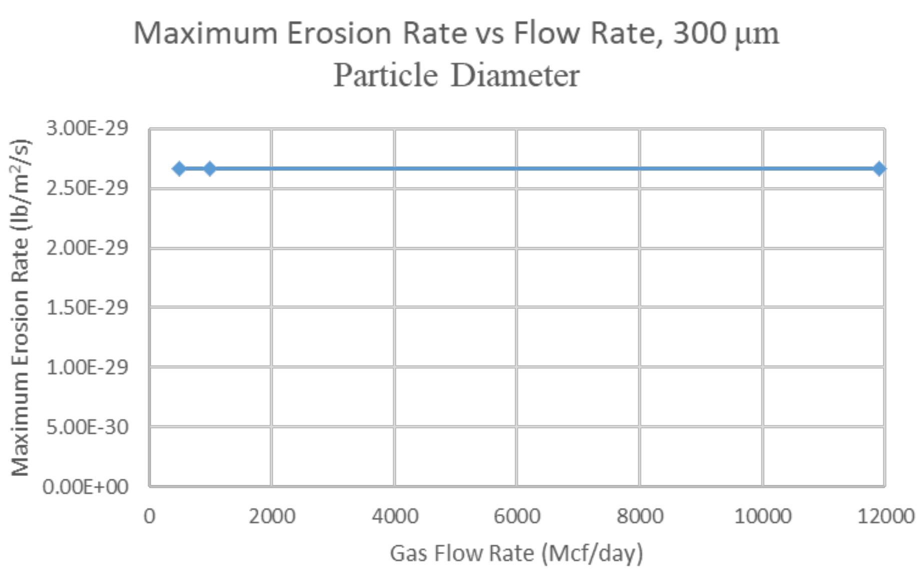

Figure **3-18** Effects of Gas Flow Rate for 300 μm Sand Particles

We should expect that the higher gas flow rate would lead to a higher erosion to the orifice bore plate. However, the only cases that follow the expected trend are the 100 μm case and the 300 μm case, with the latter having a minimal difference between the different flow rates. The much smaller sizes of particles, 1 μm and 10 μm, experienced the opposite trends as higher gas flow rates lead to a decrease in terms of maximum erosion rates. This can be explained as particles get much smaller, they will follow the streamlines more closely, especially as the velocity of the carrier fluid increases. We also observed that the smaller particle size would lead to a larger maximum erosion rate on the orifice bore diameter as well, with 100 μm and 300 μm having the same magnitude of maximum erosion rate. Again, the magnitudes of the maximum erosion rate for all cases are small enough to be neglected.

3.3 Conclusion

From parametric studies of the chemical and organic contamination on the orifice bore plate, we observed contamination layer will affect the measurement accuracy of the orifice meter, as it would change the discharge coefficient. We observed the wider contamination layer would cause an increase in changes of the discharge coefficient. We also observed the most magnitude changes occurs when the length of the layer covers half of the orifice plate.

From parametric studies of the effects of erosion rate on the orifice bore plate through different particle sizes and gas flow rates, we observed the following trends:

- As particle sizes get smaller, we observed an increase in terms of maximum erosion on the orifice bore plate.
- As gas flow rates increase, we observed an increase of maximum erosion rate on the orifice bore plate for larger sized particles (100 μm and 300 μm). However, for the smaller sized particles (1 μm and 10 μm), we observed the opposite trend where an increase in gas flow rate would lead to a decrease in maximum erosion rate on the orifice bore plate.

We also observed that the magnitude of the erosion rate is quite small for all cases, to the point that it can be neglected as it would cause minimal changes to the orifice bore plate for a period of operation time since our studies are conducted based on 24 hours of flowing time. Since most of the sand particles will be filtered out before entering the orifice metering tube, we can conclude that the unfiltered sand particles carried by the flowing gas would have a negligible effect to the orifice bore plate. If the orifice bore plate was damaged due to particle erosion before the recommended plate changing schedule, it would most likely due to a dysfunction of the filters or other effects such as chemical and organic contamination, physical deformation, or some other uncertainty effects.

Reference

Araoye, Abdulrazaq Adeniyi, 2015: “Investigation of Flow and Erosion Characteristics through a Set of Restricting Orifices.” Master’s Thesis, King Fahd University of Petroleum & Minerals.

Blatt, W., et al. “The Influence of Hydrodynamics on Erosion-Corrosion in Two-Phase Liquid-Particle Flow.” *CORROSION*, vol. 45, no. 10, 1989, pp. 793–804., doi:10.5006/1.3584985.

Davis, R.W., and Mattingly, G.E. (1977). “Numerical Modelling of Turbulent Flow Through Thin Orifice Plates”, Proceedings of the Semp. on Flow in Open Channels and Closed Conduits Held at NBS, pp. 23-25.

DeOtte R.E., Morrison G.L., Panak D.L., Nail G.H., 1991: 3-D Laser Doppler Anemometry Measurements of the Axisymmetric Flow Field near an Orifice Plate. Flow Meas Instrum 2(2):115–123.

Dukowicz, John K. “A Particle-Fluid Numerical Model for Liquid Sprays.” *Journal of Computational Physics*, vol. 35, no. 2, 1980, pp. 229–253., doi:10.1016/0021-9991(80)90087-x.

Durst, F., Founti, M. and Wang, A.B., 1988: Experimental investigation of the flow through an axisymmetric constriction. Turbulent Shear Flows, 6, Springer-Verlag, 338-350.

Durst, F., and A. B. Wang, 1989: Experimental and Numerical Investigations of the Axisymmetric, Turbulent Pipe Flow Over a Wall Mounted Thin Obstacle.

Eslinger, Byron Scott, 2004: “Computational Fluid Dynamic Simulations of High Speed Flow through Restrictions.” Master’s Thesis, The University of Tulsa.

Jones, W.P, and B.E Launder. “The Prediction of Laminarization with a Two-Equation Model of Turbulence.” *International Journal of Heat and Mass Transfer*, vol. 15, no. 2, 1972, pp. 301–314., doi:10.1016/0017-9310(72)90076-2.

McLaury, B.S., Shadley, J.R., and Rybicki, E.F. “Modeling Erosion in Chokes,” ASME-Fluids Engineering 236, 1 (1996): pp. 773-782.

Morrison, G.L., DeOtte Jr., R.E., Nail, G.H., Panak, D.L., 1993: Mean Velocity and Turbulence Fields inside a β=0.50 Orifice Flowmeter. AIChE J. 39, 745-756.

Nail, G.H., 1991: A Study of 3-Dimensional Flow through Orifice Meters, Ph.D. Dissertation, Texas A&M University.

Nemitallah, M. A., et al. “Solid Particle Erosion Downstream of an Orifice.” *Journal of Fluids Engineering*, vol. 137, no. 2, 2014, doi:10.1115/1.4028283.

Ward-Smith, A.J. “Critical Flowmetering: The Characteristics of Cylindrical Nozzles with Sharp Upstream Edges.” *International Journal of Heat and Fluid Flow*, vol. 1, no. 3, 1979, pp. 123–132., doi:10.1016/0142-727x(79)90028-6.

Whetstone JR, Cleveland WG, Bateman BR, Sindt CF, 1988: Measurements of Coefficients of Discharge for Concentric, Flange-tapped, Square-Edged Orifice Meters in Natural Gas over a Reynolds Number Range of 25,000-16,000,000. NIST Technical Note TN-1264. NIST, Washington D.C.

Zhang, Jun, McLaury, Brenton S., and Siamack A. Shirazi. "Predicting Erosion from Small Particles in Sudden Contraction and Expansion Geometries with Improved

Near Wall Treatment." Paper presented at the CORROSION 2016, Vancouver, British Columbia, Canada, March 2016.

Chapter 4

Analysis of Perforation Erosion Through Computational Fluid Dynamic Modeling (CFD)

Abstract

Field and experimental data have shown that perforation erosion during shale gas stimulation invalidates the assumption of a constant coefficient of discharge. However, perforation erosion is not fully understood yet.

In this work, a perforation erosion model was built using computational fluid dynamics (CFD) and validated against laboratory data. We then conducted parametric studies to investigate the impact of treatment rate, proppant concentration, proppant size, and fluid viscosity on perforation erosion.

Our results demonstrated that higher treatment rate and larger proppant lead to higher erosion to the perforation diameter. Perforation erosion decreased when fluid viscosities increased from 10 *cp* to 100 *cp*, and then increased when the fluid viscosity was increased to 1,000 *cp*. Our new understandings could be applied to improve perforation design in shale wells.

4.1 Introduction

4.1.1 Multistage Fracturing

The limited entry technique was first applied as a cost-effective method to stimulate multiple pay zones in vertical wells with varying stress regimes. “Limited entry” is a term for the practice of limiting the number of perforations in a completion interval to promote fracture propagations during a stimulation treatment. The resulting “choking” effect creates excessive pressure in the casing, allowing the simultaneous entry of fracture fluid into multiple intervals of varying in-situ stresses. Limited entry has been applied in stimulation of shale wells to help propagate multiple fractures and optimize stimulated reservoir volume (SRV). Lagrone & Rasmussen (1963) recommended maintaining perforation friction at a maximum during treatment by continuously increasing injection rate to counteract the loss in differential perforation friction pressures from eroding perforations. The treatment needs to be pumped at maximum allowable pressure by increasing the slurry rate as needed throughout the treatment.

Plug-and-perf completions are one of the most commonly used completion methods for horizontal wells in unconventional reservoirs. The plug-and-perf system stimulates the wells by creating multiple isolated fracturing stages. Each fracturing stage typically involves three to six perforation clusters that are simultaneously stimulated by the injected fluid. The stages are completed with a cemented casing or liners as it combines two common fracturing techniques: limited entry and segmented fracturing. Numerical simulation studies done by Lecampion and Desroches (2015), Cheng et al. (2016), and

Zhao et al. (2016) have shown that the limited-entry can effectively promote the uniform growth of fractures in multi-stage hydraulic fracturing.

Rational design of perforation parameters has remarkably improved the performance of multi-stage hydraulic fracturing in horizontal wells. Through Fiber-Optic diagnostic data, Somanchi et al. (2016) have shown that the perforation clusters in these horizontal wells were successfully cracked and hydraulic fractures were formed. However, some fractures began to propagate at a lower rate or even stopped growing after proppants were pumped. This indicates the proppant-carrying fracturing fluid flowing with high velocity erodes the perforations during fracturing, making the perforations lose their ability of limited entry. As a result, the influx into each fracture becomes non-uniform, leading to reduction of treatment effectiveness.

4.1.2 Perforation Strategies

Optimization of perforations is important for shale stimulation. During fracture stimulation, the perforations should not cause an excessive restriction to flow as it could cause insufficient flow area through the perforations or the possibility of creating multiple competing fractures. The optimal goal for every perforation cluster is to receive equal volumes of stimulation fluid as any perforation that is shot and not opened is essentially a waste. Perforations also need to ensure sufficient flow from the reservoir during the production.

The most prevalent question on designing a completion for horizontal wells is how many perforation clusters should be treated simultaneously. For the ideal situation, a single fracture treatment should be able to treat all the perforation clusters spaced along the lateral at once. In reality, the stimulation treatment most likely only enters a fraction of the available clusters while leaving sections of the lateral unstimulated. To determine the number of perforation clusters to place within a stage, the goal should be to fit as many clusters as possible in a stage while still allowing equal distribution of the stimulation fluid. The effectiveness of cluster count can be evaluated through the use of production logs from the horizontal wells. Miller et al. (2011) analyze through horizontal production logs across several basins and showed that on average approximately one in four perforation clusters are not producing; for Marcellus shale, the number increases to almost 30%. Their study also examines the effect of the number of perforation clusters utilized, as they indicate that the best wells utilize two to six perforation clusters per stage, with fewer clusters per stage leading to better results. The Wasp equation (**Equation 4-1**) (Wasp et al., 1970) can be referred to determine the minimum rate required to transport particle of a specific size. The v_t represents the absolute minimum velocity and does not consider factors such as casing collars, deviations other than horizontal, or the inertial effects of slurry changing directions, all of which could lead to additional settling. Due to the possibilities of such effects, the author recommends that the minimum rate per cluster should exceed three times the v_t obtained from the equation.

$$v_t = F[2g(s-1)D]^{1/2}\left(\frac{d_p}{D}\right)^{1/6} \quad \textbf{(4-1)}$$

where:

v_t – Minimum transport velocity (*ft/s*)

F – Empirical constant that varies between 0.4 and 1.5

D – Pipe diameter (*in*)

d_p – Particle diameter (*in*)

g – Gravity acceleration

s – Ratio of particle and fluid densities

The size of the perforation diameter must be considered for which perforation charges to use for a limited entry style of design. If the perforation diameter is too large, it becomes difficult to build up enough back pressure; if the entrance hole is too small, the proppants may have difficulty entering the perforation. Gruesbeck and Collins (1982) suggested the perforation diameter should be eight to ten times larger than the average proppant diameter in order to prevent bridging of proppant in the near wellbore. Their experimental studies take considerations of factors such as variance between nominal and actual hole sizes, gun positioning, and variation in proppant diameters. Their works provide a lower bound to the perforation size and the perforations should be designed to create a sufficient pressure drop. Perforation friction varies directly with the pumping rate as increasing the rate through one perforation also increases the pressure drop in each perforation, thus diverting stimulating fluid to other perforations that may not have as much velocity going through them. Typical levels of pressure drop range from 500 to 1,000 psi for each perforation (Ketter et al., 2006) and the pressure drop, Δp, can be calculated using **Equation 4-2**.

$$\Delta p = \frac{0.237 \times q^2 \times \rho}{2 \times C_d^2 \times d_{perf}^4 \times n^2} \tag{4-2}$$

where:

q – Flow rate for each perforation (*bbl/min*)

ρ – Fluid density (lb_m/gal)

C_d – Discharge coefficient (*0.6* for the initial perforations if unknown)

d_{perf} – Perforation diameter (*in*)

n – Number of perforations

Through experimental studies, Behrmann and Elbel (1991) indicated that in cased hole environments, fractures initiate at the base of the perforation near the sandface, thus penetration extension beyond four to six inch is not required. However, their tests were conducted in large sandstone blocks with the borehole drilled without applied stresses. In their recent tests, Behrmann (2012) conducted in shale blocks where the borehole was drilled with the rock under stress. The results from these studies suggested a formation penetration of 1 to 1.5 times the wellbore diameter.

The length of the perforation cluster should be dominated by the limited entry design and based on the number of perforations. El Rabaa (1989) recommended to keep perforation cluster length to less than four times the wellbore diameter in order to minimize the creation of multiple fractures. In the more recent experimental studies, Behrmann (2012) suggested that the cluster length should be reduced to two wellbore diameters to minimize the initiation of multiple competing fractures.

Each stage of a plug-and-perf process consists of creating multiple fractures from several clusters of perforations. It has shown in field operations that the most feasible perforation placement for limited entry is 180° phasing perforations. The fracturing fluid will be forced to exit on opposite sides of the pipe through 180° perforating. By design, each perforation in limited entry is desired to be involved in the treatment. However, if there are perforations not involved during the treatment, the allotted perforation pressure drop becomes excessive due to the flow rate per perforation increases, thus leading to a substantial increase in perforation pressure drop. Perforation can also be shot with 60°, 90°, or 120°.

4.1.3 Erosion Modeling

McLaury (1993) developed erosion models particularly for the oilfield geometries as he used elbows and tees for his initial developments for the University of Tulsa's Erosion-Corrosion Research Center (E/CRC). In 1996, McLaury examined and studied erosion in fluid flow through a choke geometry setting. It introduced random impingements resulting from the turbulent fluctuations to his equations and established the foundation of the McLaury's erosion model. Zhang et al. (2006) from E/CRC further built upon the McLaury's erosion model by applying standard wall functions for the near-wall particle tracking and rebounding of the particles at a radius from the wall. Parsi et al. (2014) summarized what has been done so far in terms of solid particle erosion modeling, provided a comprehensive review mainly focusing for erosion in oil, gas wells, and pipelines applications.

4.1.4 Perforation Erosion

Since a perforation is similar to an orifice, research on fluid flow through orifice is helpful in establishing criteria for the analysis of perforation erosion (**Figure 4-1**). At the high Reynolds number flow conditions that exist through perforations in limited entry treatment's (*Re* of 10^4), fluid flows through the perforations behaves similarly as turbulent jets (Cramer, 1987). When proppants pass through a perforation during a treatment, they erode the perforation edge (**Figure 4-2**), leading to simultaneous increase in both C_d and d_{perf}. The increase of either of these parameters will also increase flow capacity of the perforations and creates pressure drop for the perforations. The subsequent rounding at the inlet face of the perforations could conceivably continue until the perforation resembles a nozzle with a total elimination of jet contraction as demonstrated in **Figure 4-3**. According to Long et al. (2017), these geometric changes result in fluid redistribution among different perforation clusters, dimensional changes of hydraulically induced fractures, and even failure of limited-entry treatments that are expected to mitigate the stress-shadow effects. In the unconventional reservoirs, high injection rate is usually applied for multi-stage hydraulic fracturing, resulting in relatively severe perforation erosion.

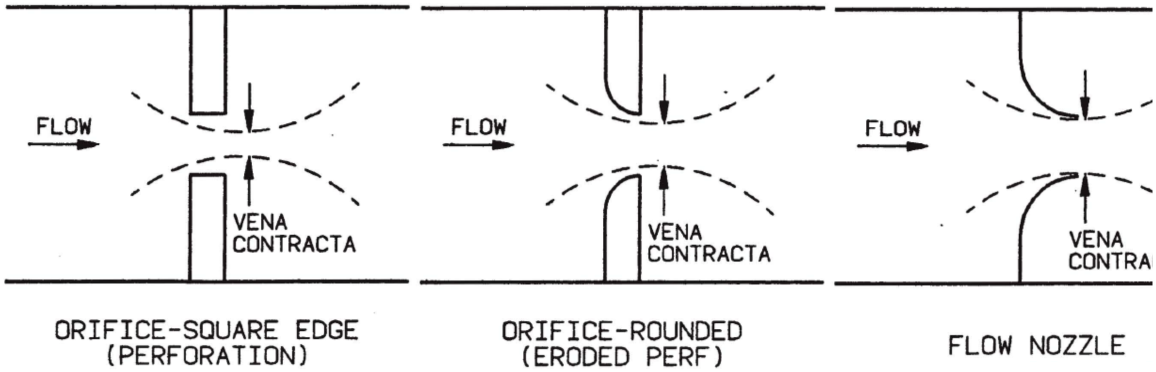

Figure **4-1** Perforation vs. Flow Nozzle (Crump, 1988)

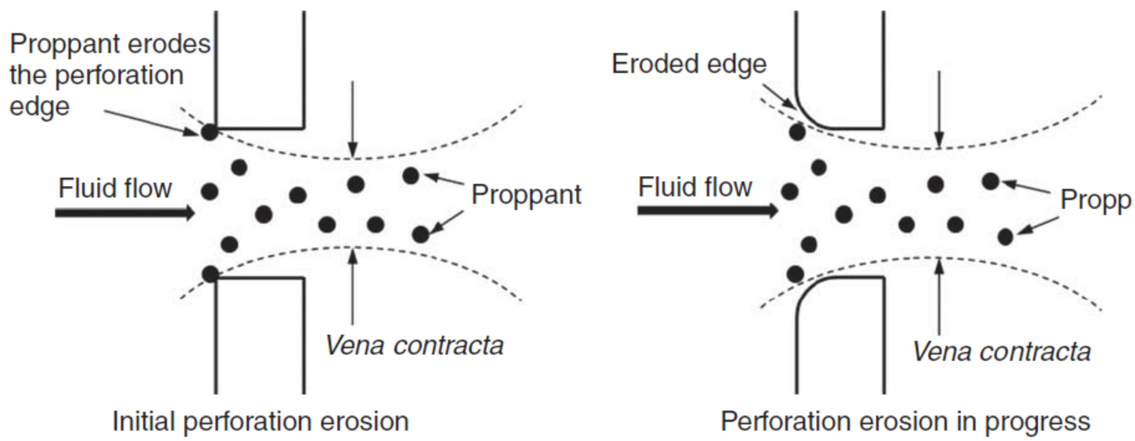

Figure **4-2** Schematic of Perforation Erosion (Long et al., 2017)

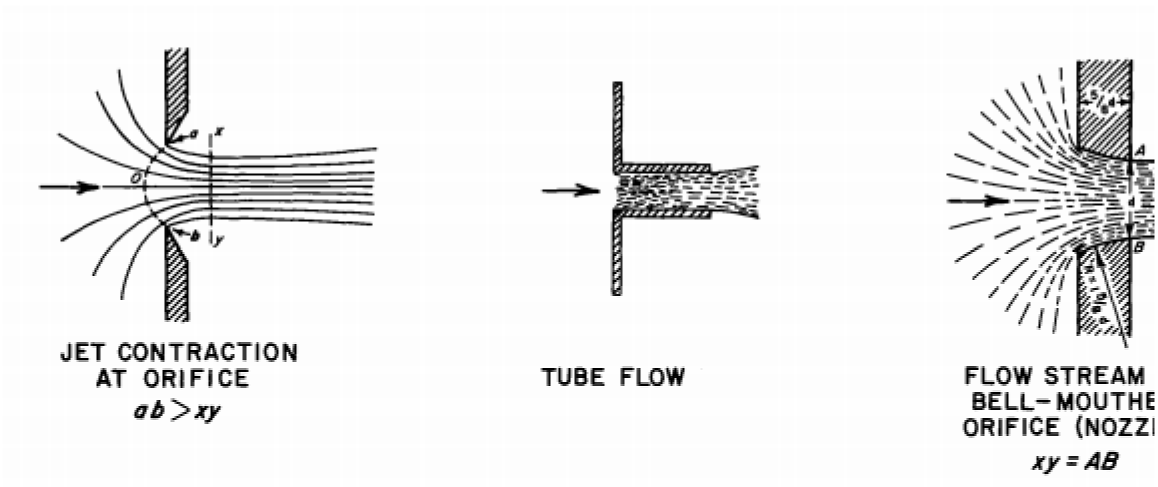

Figure **4-3** Orifice Flow Dynamics (Cramer, 1987)

The experiment conducted by Crump and Conway (1988) shows that the proppants pumped together with injected fluid would bring erosion to the perforations based on two mechanisms. First, the perforation wall will be slowly damaged due to the erosion from the proppant, leading to an increase of perforation diameter, d_{perf}. The proppant will also erode the edge of the perforation entry, resulting in a rapid growth of discharge coefficient, C_d. Their experimental data show C_d of 0.5 to 0.6 for undamaged perforations whereas C_d of 0.95 for completely eroded perforations. In such a case, if the perforation erosion is neglected, the fracture propagation results would greatly deviate from the actual situations.

In order to determine the variation of C_d and d_{perf} with the effects of perforation erosion, a number of researchers have proposed their models and correlations. Willingham et al. (1993) developed an empirical correlation to determine C_d of sand slurries through perforations in field condition while assuming d_{perf} is given. Their assumption of the known

d_{perf} suggests that it is difficult to handle the simultaneous increase of C_d and d_{perf} in real-time base. Their proposed work lumped C_d and d_{perf} together as a new parameter called the hydraulic-perforation diameter, H, as given by **Equation 4-3**, with C_d and d_{perf} simplified by Cramer (1987).

$$H = d_{perf}\sqrt{C_d} \tag{4-3}$$

By using the data from field studies, Cramer (1987) fitted H as a simple linear correlation of the total mass of the proppant pumped through the perforation M after the C_d-dominated stage. Romero et al. (2000) developed their simple linear function of M by empirically fitting C_d based on the work from Crump and Conway (1988) during the C_d-dominated stage. They proposed a new linear equation to fit H but neglected some other parameters that may affect H, such as fluid-injection rate and sand concentration. However, their model cannot reflect the actual simultaneous increases in C_d and d_{perf} and increase them alternatively instead.

Li et al. (2018) coupled the perforation erosion model with fracture growth model as they found that the perforation erosion will significantly deteriorate the non-uniform growth of multiple fractures. Their results showed the initial erosion rates become higher with increasing proppant concentration but the varied concentration does not affect the growth of the hydraulic fractures. They also found that higher treatment rates are beneficial to the limited-entry design as they lead to more uniform growth of fractures. Robinson et al. (2020) provided acoustic imaging of perforation erosion through their examinations of the perforations. They demonstrated the capabilities of the acoustic imaging technology as the results from over 35,000 perforations were able to successfully image the entire length of the cased wellbores and capture the distribution, size, and measured diameter for each perforation in each cluster. Yosenfnejad et al. (2020) investigated the effects of perforation hole size, geometry, and erosion to C_d through their experimental studies. In all of their tests, erosion led to an increase in C_d and they suspect that the effect of erosion also depends on the pressure condition as they found higher increase in C_d for high cavitation numbers. They also found the removal of small corners, edges, irregularities, and inhomogeneities on the perforation tunnel surface can lead to a significant increase of the C_d. Loehken et al. (2020) examined the effect of the perforation hole size by using different charges, the length of the treatment path, the hole geometry, and the effect of burr and cement to C_d through their experimental studies. They found that the C_d values measured for real perforation holes differ significantly and record higher values compared to simple drilled plates. Their investigation also shows that the burrs on both sides of the perforation hole, particularly on the inside of the hole plate, can affect the value of C_d.

Li et al. (2007) investigated the surface of a drilled hole in carbon steels through different imaging analysis and Vickers microhardness tester. They found the hardness of the microstructure is related to the depth of the white etching layer (WEL) formed on the hole surface with thinner WEL consisting of lower hardness value. They also observed the hardness depth profile near the hole surface changes with the cutting speed and matrix hardness with cases displaying hardness continuously decreases with the depth from the hole surface. Xu et al. (2011) conducted tensile and impact tests for K55, N80, and P110 to investigate the fracture mechanisms for each steel casing. They conducted various drilling tests and analyzed their results through different imaging techniques. They found that structural damages are always associated with drilling. Morita and Shiozawa (2014) conducted extension and compression tests on several casings including P110 casing. They found the casings were uniformly deformed after exceeding the yield strength and non-uniform deformation was induced. Koneti and Gokhale (2015) performed metallurgical and imagining analysis on both failed and non-failed P110 casings. They demonstrated the regions near the inclusion content have lower carbon content, which led to lower hardness of the material. Tensile strength correlates to hardness as higher yield strengths generally mean higher tensile strengths. Through regression analysis, Pavlina and Tyne (2008) found hardness correlates with the mechanical properties in steel alloys including the likes of P110 grade material. Volume worn is inversely proportional to hardness (Holm, 1946). Various erosion models use material's hardness as one of the parameters for erosion calculation, including the McLaury's erosion model.

4.2 Methodology

Computational Fluid Dynamics (CFD) based simulations have been widely used for predicting erosion in complex flow domains. For CFD based erosion modeling, it typically consists of three main steps: a flow model, a particle tracking model, and an erosion model.

4.2.1 Flow Modeling

The continuous phase of the flow domain is governed by the Reynolds Averaged Navier-Stokes equations (RANS) with the continuity equation (**Equation 4-1**) and the momentum equation (**Equation 4-2**), with the Reynolds stresses solved by the k-ε turbulence model (**Equation 4-3** and **4-4**). See Chapter 3 Section 3.2.1 Flow Modeling for reference.

$$\frac{\partial \rho}{\partial t} + \frac{\partial}{\partial x_i}(\rho \overline{U_\iota}) = 0 \tag{4-1}$$

$$\frac{\partial}{\partial t}(\rho \overline{U_\iota}) + \frac{\partial}{\partial x_j}\left(\rho \overline{U_\iota}\,\overline{U_J}\right) = -\frac{\partial p}{\partial x_i} + \frac{\partial}{\partial x_j}\left(\mu \frac{\partial \overline{U_\iota}}{\partial x_j}\right) - \frac{\partial}{\partial x_j}\left(\rho \overline{u_\iota}\,\overline{u_J}\right) \tag{4-2}$$

$$\frac{\partial(\rho k)}{\partial t} + \frac{\partial(\rho U_j k)}{\partial x_j} = \frac{\partial}{\partial x_j}\left[\left(\mu + \frac{\mu_T}{\sigma_k}\right)\frac{\partial k}{\partial x_j}\right] + P_k - \rho\varepsilon \tag{4-3}$$

$$\frac{\partial(\rho \varepsilon)}{\partial t} + \frac{\partial(\rho U_j \epsilon)}{\partial x_j} = \frac{\partial}{\partial x_j}\left[\left(\mu + \frac{\mu_T}{\sigma_\varepsilon}\right)\frac{\partial \varepsilon}{\partial x_j}\right] + C_{\varepsilon 1}\frac{\varepsilon}{k}P_k - C_{\varepsilon 2}\rho\frac{\varepsilon^2}{k} \tag{4-4}$$

4.2.2 Particle Tracking Discrete Phase Model (DPM)

The DPM particle tracking is simulated in a Eulerian-Lagrangian approach, with the continuous phase for the flow field is modeled by the Eulerian method while a second discrete phase for the particle phase is modeled by the Lagrangian method. The motion equation for the discrete phase particle is solved by the Newton's equation of motion (**Equation 4-5**) with the drag force (**Equation 4-6**), gravity buoyancy force (**Equation 4-7**), and other forces including virtual mass force, pressure gradient force, Brownian force, and Saffman's lift force. See Chapter 3 Section 3.2.2 for reference.

$$\frac{dV_p}{dt} = F_D + F_G + F_{other} \tag{4-5}$$

$$F_D = \left(\frac{18\mu}{\rho_p d_p^2}\right)\left(\frac{C_D Re_p}{24}\right)\left(U_f - U_p\right) \tag{4-6}$$

$$F_G = g\,\frac{(\rho_p - \rho)}{\rho_p} \tag{4-7}$$

4.2.3 Erosion Model

The McLaury erosion model (**Equation 4-8**) is utilized to solve the erosion properties resulting from the impingements of the particles with **Equation 4-9**, **4-10**, and **4-11** for each of the parameters. See Chapter 3 Section 3.2.3 for reference.

$$ER = AU^n\, f(\alpha)\dot{m} \tag{4-8}$$

$$A = F(B_h)^{-0.59} \tag{4-9}$$

$$f(\alpha) = b\alpha^2 + c\alpha\,,\ \alpha \leq \alpha_{lim} \tag{4-10}$$

$$f(\alpha) = x\cos^2(\alpha)\sin(w\alpha) + y\sin^2(\alpha) + z\,,\ \alpha > \alpha_{lim} \tag{4-11}$$

4.2.4 Model Validations

To ensure the accuracy of the erosion model predictions, two experimental data works were considered in this research with validations for Blatt et al. (1989) shown in **Figure 4-4** and Zhang et al. (2016) shown in **Figure 4-5**. See Chapter 3 Section 3.2.4 for detailed reference.

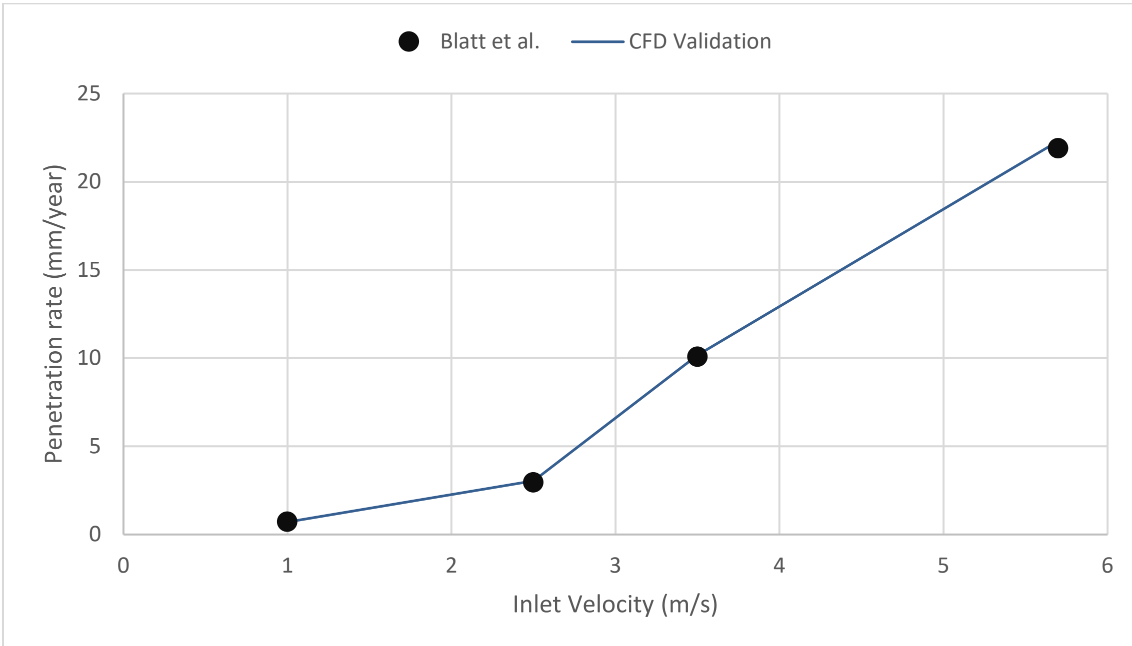

Figure **4-4** Comparison between CFD erosion model results and the experimental data of Blatt et al. (1989)

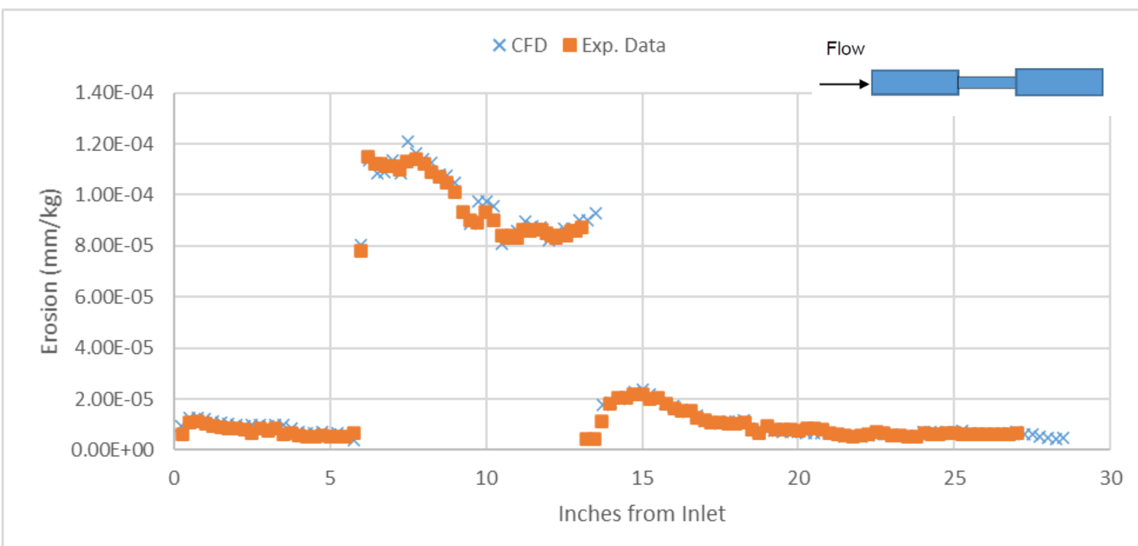

Figure **4-5** Comparison between CFD erosion model results and the experimental data of Zhang et al. (2016)

4.2.5 CFD Model Setup for Perforation Erosion

Smooth Casing and Perforation Entrance

To examine the effects of the injected proppant erosion to the perforations, we setup CFD models to simulate the treatment fluid carrying the proppants within the fractures. We started out our CFD model using a 2-D, single cluster from a six-stage hydraulic fracture with five clusters for each stage. **Figure 4-6** shows a schematic view of the perforation geometry used in the simulation as each cluster is shot with 180° phasing; **Table 4-2** shows the dimensions of our model setup.

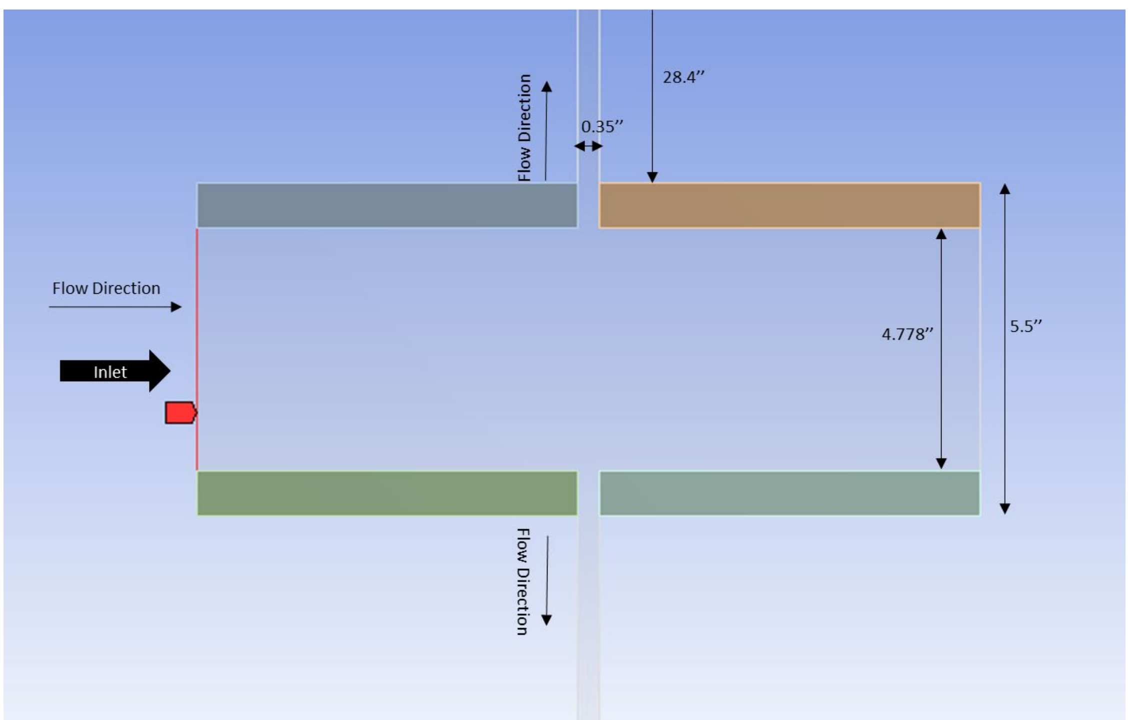

Figure **4-6** Perforation Geometry of the Flow Domain

Table **4-2** Perforation CFD Model Parameters

Casing	P110
Pipe ID	4.778 *inch*
Pipe OD	5.50 *inch*
Pipe Weight	20 lb_m/ft
Pipe Wall Thickness	0.361 *inch*
Cluster Length	12 *inch*
Perforation Density	2 SPF 180° Phasing
Perforation ID	0.35 *inch*
Perforation Length	28.4 *inch*
Treatment Fluid	Water
Proppants	Silica Sand
Proppants Density	165 lb_m/ft^3

Casing with different hardness

We implemented different hardness to the casing from the base model to simulate the effects from gun charges to the perforation entrance through the casing as shown in **Figure 4-7**. Each of the four casing pieces is divided into two regions as there is a thinner layer (one-third inch wide) adjacent to the perforation entrance. The hardness for the longer region for each of the casing pieces are kept as base case value (100%) while the thinner layer's hardness can be changed accordingly.

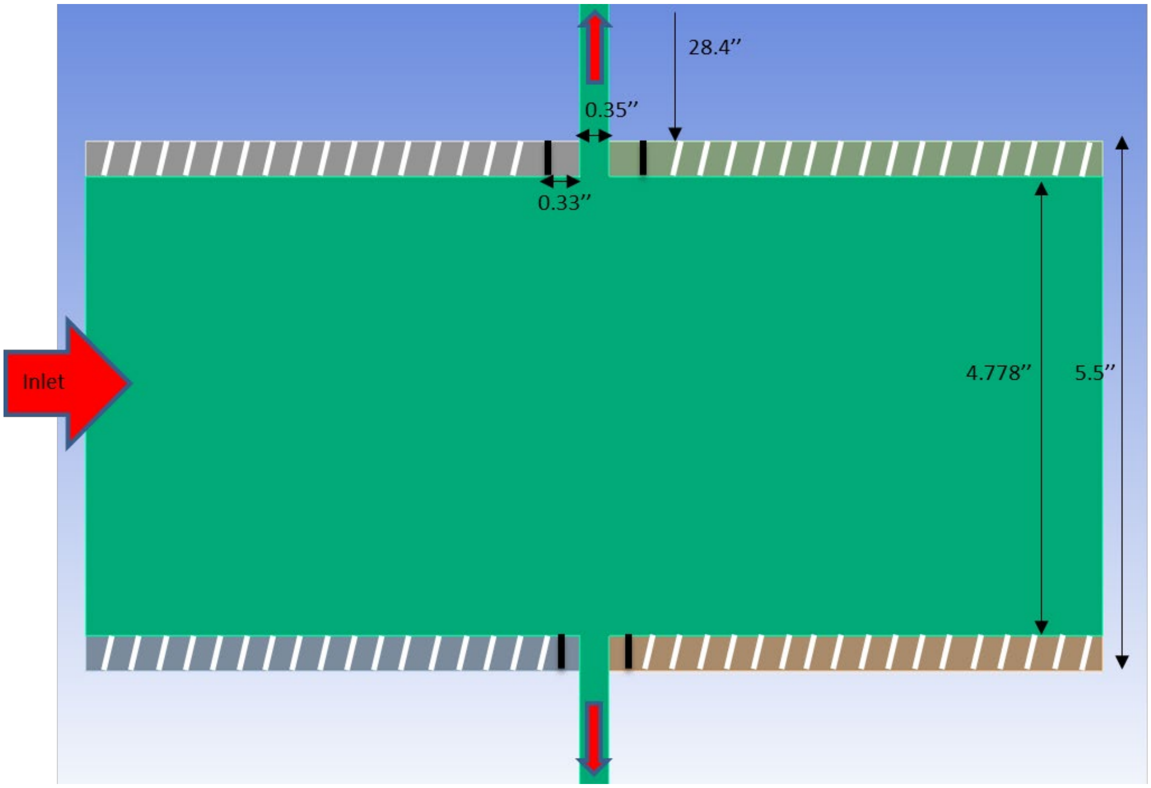

Figure **4-7** Perforation Geometry of the Flow Domain for Different Casing Hardness

Figure 4-8 shows the structured grid mesh generated based on the perforation geometry. The computational domain is meshed with rectangular grids with global size factor of 0.01 for the flow domain and 0.05 for the solid layers adjacent to the perforation entrance. This meshing configuration yields a total of 155,144 cells. The contact between the solid walls and fluid walls has to be created with the harder material (casing) as the target. The walls are then coupled accordingly for the casing sections and this is a necessary step for 2-D models in order to change the hardness for the solid walls. Here we did not account for the cement section and the formation rock section after the casings as we did not create those zones for our model.

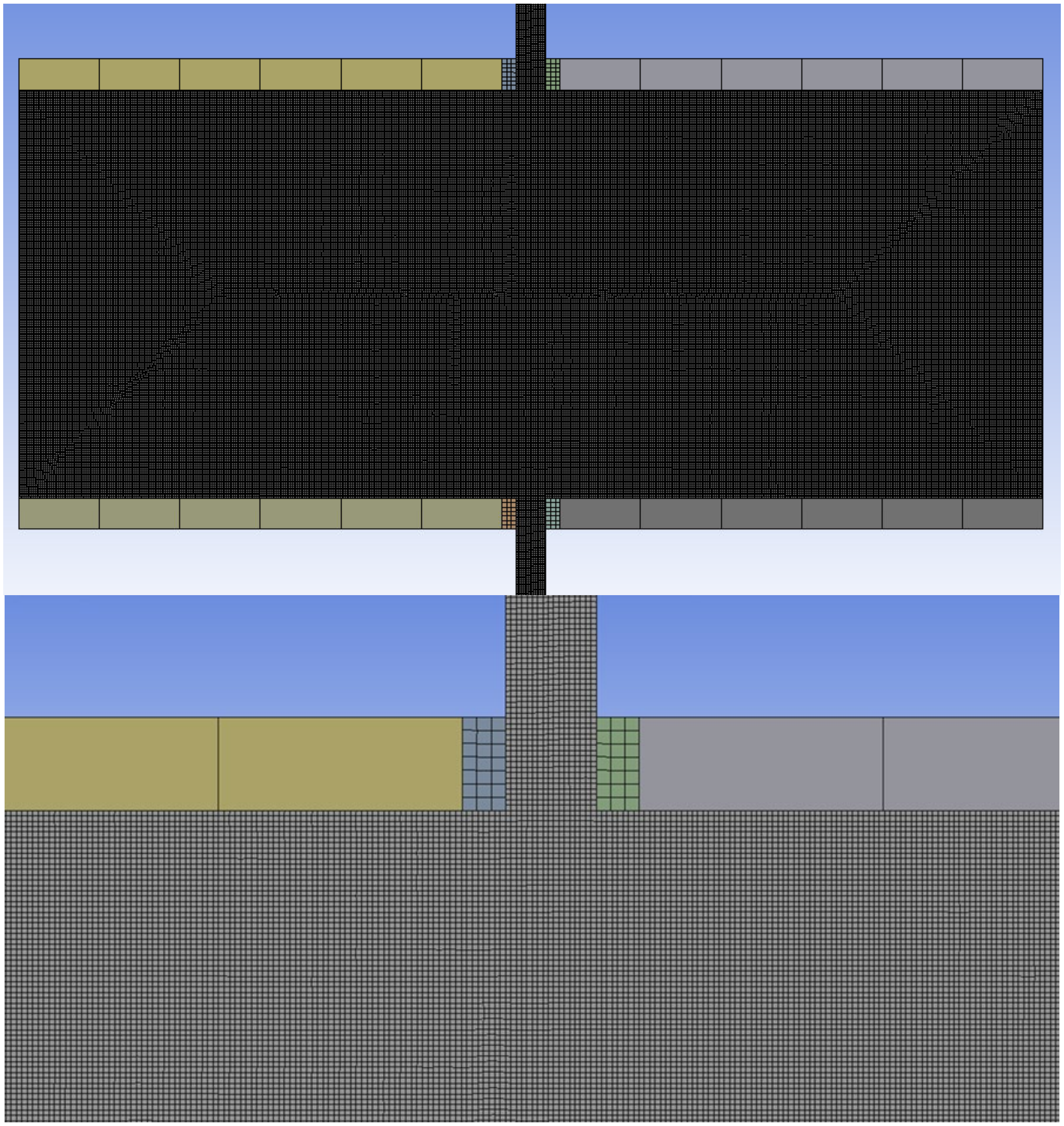

Figure **4-8** Mesh of the Perforation Geometry: Overview (upper), around Perforation Entrance (lower)

The fluids are pumped into the inlet surface while carrying the sand particle proppants. For the base case, the proppant concentration is 2 lb_m/gal while the treatment fluid is pumped with a rate of 90 *bbl/min* (6 *bbl/min* for each cluster). The treatment fluid is water with a viscosity of 1 *cp*. The sand particles for the base case have sizes of 40/70 *mesh* and distributed using a Rosin-Rammler size distribution with mean diameter of 284 μm and a spread parameter of 3.5, as Rosin-Rammler is widely used in the mineral processing industries to describe size distributions of particles such as silica sand. The sand particles are non-spherical with a shape factor of 0.8. The pipe wall is simulated as P110 steel casing pipes with density of 490 lb_m/ft^3 and as no-slip boundary conditions. The total stimulation time is set as one hour.

The stage length is 12 *inch* with two perforation shots at the middle of the stage in 180° phasing. The pipe casings have an inner diameter of 4.778 *inch* and an outer diameter of 5.50 *inch*, thus gives a pipe wall thickness of 0.361 *inch*. The perforations have an inner diameter of 0.35 *inch* while the length of the perforations is 28.4 *inch*. The pressure of the inlet for the flow domain is set at 1160 *psi*. The particles interactions for the pipe wall boundary are set as *reflect* and *escape* for the outlets. The model is simulated with standard k-ε model as the turbulence model while Lagrangian DPM tracking method is utilized to track the particles and calculate the particle impingement information. The erosion ratios are calculated using the McLaury's erosion model. Gravity is neglected for this model as the perforations are shot in horizontal orientation.

4.2.6 Grid-Size Sensitivity Analysis

The sensitivity analysis of the different grid sizes is conducted to ensure our model is optimized before simulating. We refined the flow domain to four different sizes for this analysis, a coarser size, a coarser-medium size, a finer-medium size, and a fine size with their respective number of grids and global size factor shown in **Table 4-3**. A comparison of the variation of normalized velocity magnitude along the perforation centreline is shown in **Figure 4-9**. The comparison of the centreline velocity is a good indicator of how well the model has described the flow domain, as what we should expect a centreline velocity profile should look like for a sudden contraction type of flow geometry.

Table **4-3** Grid Sizes

	Number of Nodes	Number of Elements	Global Size Factor
Coarse Size	20709	20300	0.1
Mid Size	32917	32300	0.05
Mid Size	157539	155144	0.01
Fine Size	426791	422068	0.005

From **Figure 4-9**, we can observe that the coarser size and the coarser-medium size were not able to describe the flow domain accurately especially for the max velocity region. We can eliminate these two grid sizes as their results are still dependent on the size of the grids. The finer-medium size and the fine size were able to describe the flow domain as it accurately captures the profile for the centreline velocity. We also observed that the differences between the finer-medium size and the fine size are minimal, indicating that more mesh refinement will result in negligible changes in the computed results. We can conclude that our model will be optimized by refining the grids using the finer-medium size as it will save computational cost tremendously while having similar level of accuracy compared to the fine size.

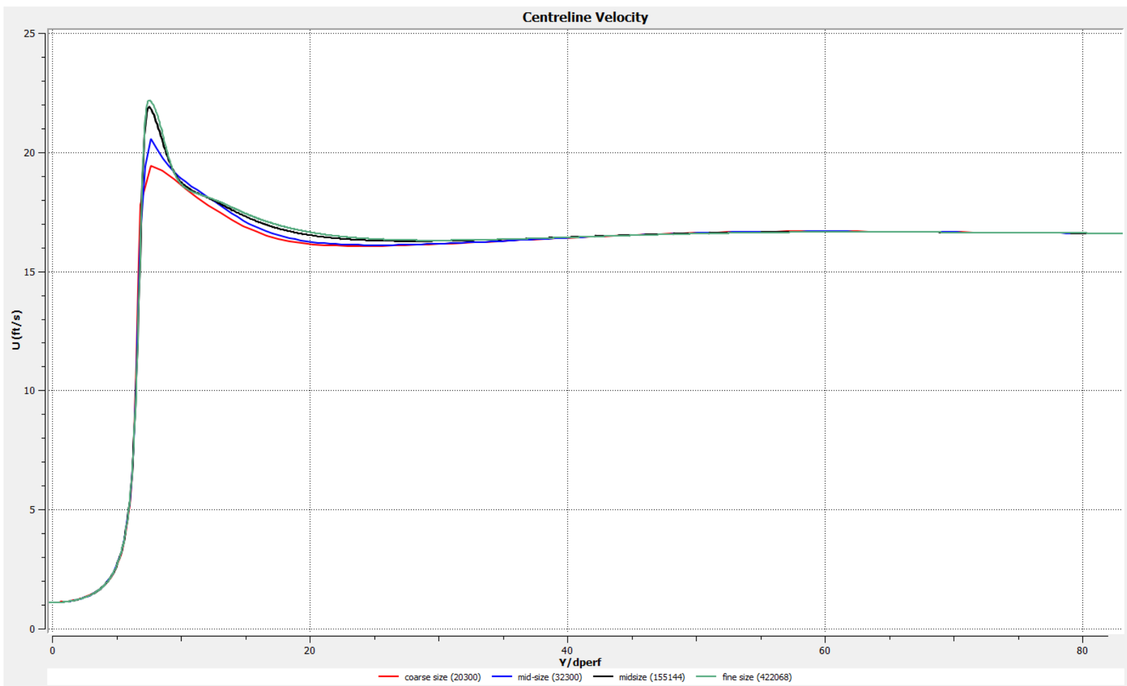

Figure **4-9** Grid Size Sensitivity – Perforation Centreline Velocity

4.3 Parametric Studies

4.3.1 Analysis of the Base Model

After the model is validated, we first examine the erosion effects to the perforation tunnel entrance from the injected proppants using the smooth wall base model with the original hardness of the casing. However, we only observed less than one percent of change in perforation diameter with 15,000 *pounds* of proppants injected. This result disagrees with what we typically experience in field settings as literatures including downhole camera analysis typically observes up to 50% of change in perforation diameter. The large differences are most likely due to how the casing wall is setup around the perforation tunnel entrance, as gun charges would not result in a perfectly smooth wall in field settings. One method to simulate these effects is to change the hardness of the casing around the entrance as the hardness of the casing will decrease drastically from the gun charges.

We dedicated a huge amount of time and effort trying to find what the actual hardness values would be for the casing after they have been drilled. However, we could not find any published literatures to provide actual data for the decreased hardness. Since we do know what the typical percentage change in perforation diameter, we can set up our base model with different hardness for the casing and match the 50% change in perforation diameter. We conducted numerous simulations using hardness ranging from 30% to 0.1%. Based on the results as shown in **Figure 4-10**, we decide to use the 0.2% hardness case as our base model for further parametric studies since it resulted in 50% change in perforation diameter with around 10,000 *pounds* of injected proppants.

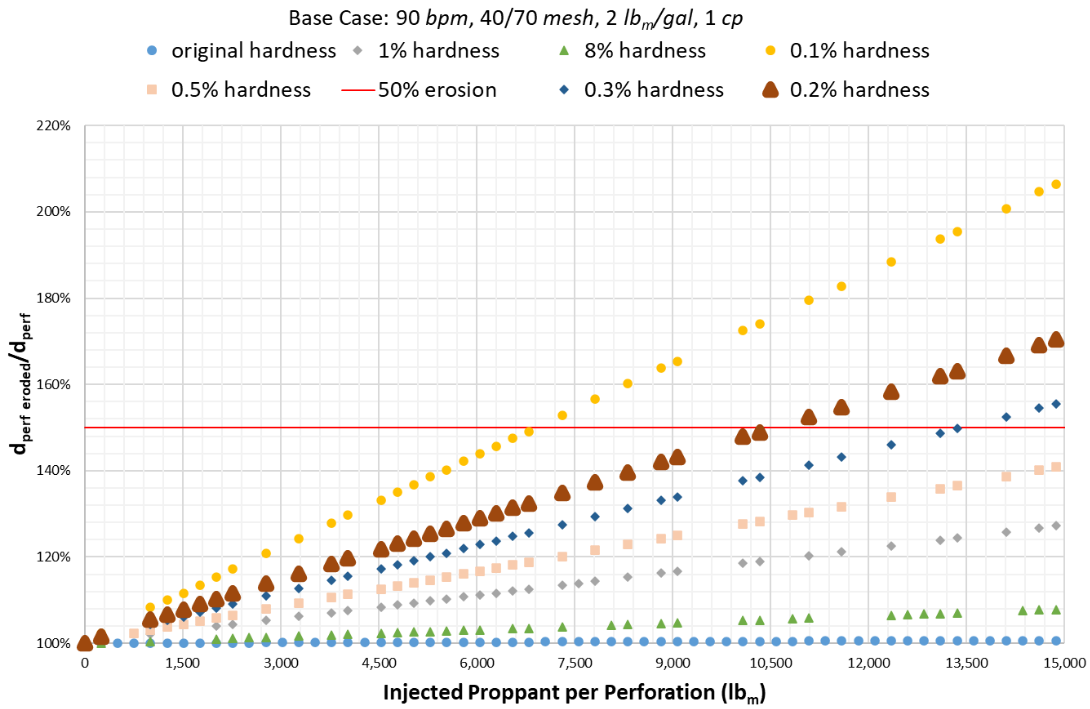

Figure **4-10** Effect of hardness of the casing around the perforation tunnel entrance

The base model has 0.2% hardness of the casing around the perforation tunnel entrance, 15,000 *pounds* of silica sand injected per perforation, with particles size of 40/70 *mesh*, proppant concentration at 2 lb_m/gal, treatment rate at 90 *bpm*, and fracture fluid viscosity of 1 *cp*. We performed parametric studies to examine the erosion effects of treatment rates, proppant concentrations, proppant sizes, and fluid viscosities. For the base case, the fluid velocity for the inlet is 4.5 *ft/s* (3.07 *mph*) with shearing rate of 90.41 per *s* and Reynolds number in the range of 10^5. The fluid velocity for the perforation entrance is 32.08 *ft/s* (21.87 *mph*) with shearing rate of 8,800 per *s* and Reynolds number in the range of 10^6.

Erosion rate of the perforation diameter at the perforation entrance will be closely examined. A new parameter for the perforation diameter, $d_{perf\ eroded}$, will be calculated based on how much penetration to the entrance of the perforation diameter, d_{perf}, from the eroding particles. $d_{perf\ eroded}$ is the sum of d_{perf} and the penetration to both sides of the walls at the perforation entrance. The results will be plotted with the x-axis defined as injected proppant per perforation in units of pounds, while the y-axis is defined as percentage change in perforation diameter, $d_{perf\ eroded}/d_{perf}$.

4.3.2 Treatment Rate

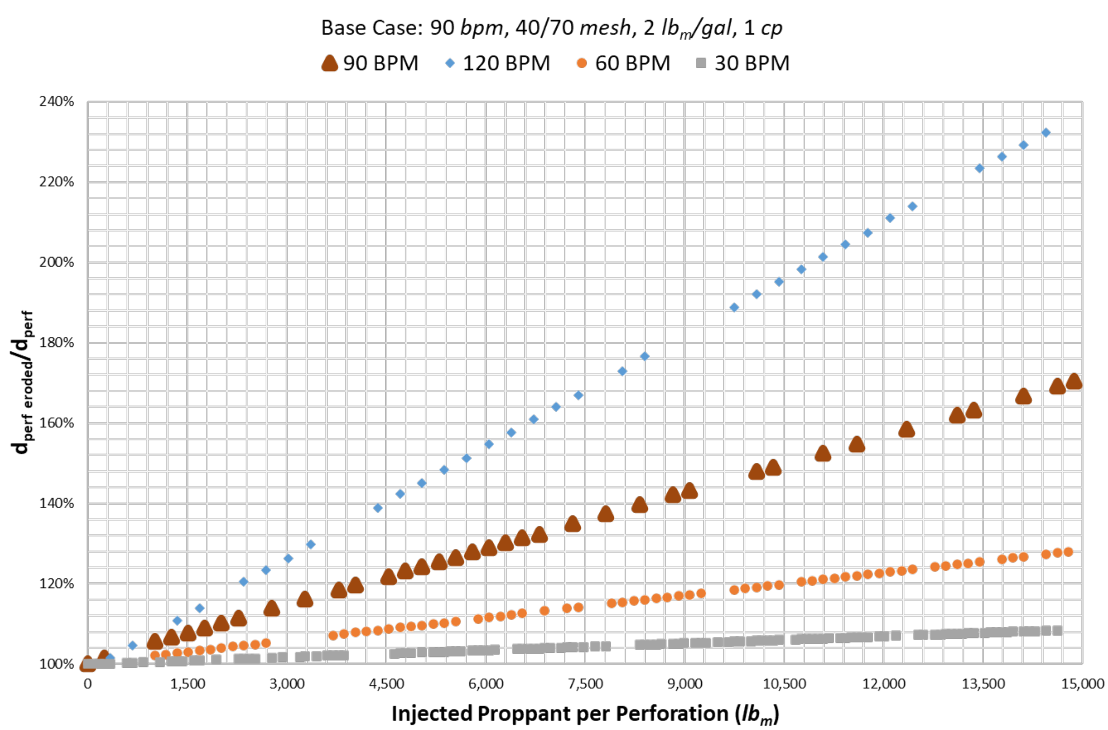

Figure **4-11** Effect of Treatment Rate

Figure 4-11 shows the ratio of eroded d_{perf} to the original d_{perf} vs. *pounds* of proppants for treatment rates of 30 *bpm*, 60 *bpm*, 90 *bpm*, and 120 *bpm* proppant concentration is 2 lb_m/gal, proppant size is 40/70 *mesh*, and fracture fluid viscosity is 1 *cp*. The overall trend shows erosion increases with increased pounds of proppants and treatment rates. The 90 *bpm* case has more than double the penetrations to the d_{perf} compared to the 60 *bpm* case, similarly for the 120 *bpm* case compared to the 90 *bpm* case. The 30 *bpm* case exhibits minimal erosion (less than 10%) to the d_{perf}, but it would take much more treatment time to achieve the desired amount of injected proppants. Since the flows are converging into the perforations, another expectation would be such that a higher treatment rate will direct more proppants toward the back end of the perforation as they are entering. This can be further validated by examining how much penetration took place to the front wall of the perforations and also the back wall of the perforations. We should expect much higher erosion taking place on the back wall compared to the front wall of the perforations as treatment rate increases.

4.3.3 Proppant Concentration

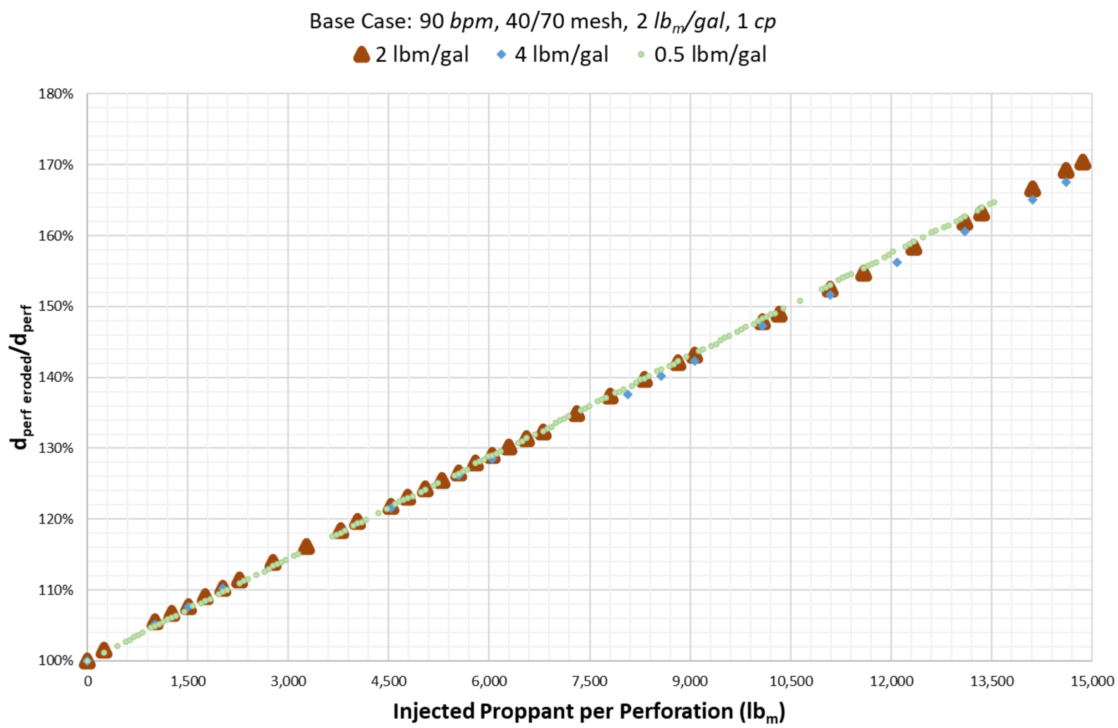

Figure **4-12** Effect of Proppant Concentration

Figure 4-12 shows the ratio of eroded d_{perf} to the original d_{perf} vs. *pounds* of proppants for proppant concentrations of 0.5 lb_m/gal, 2 lb_m/gal, and 4 lb_m/gal where treatment rate is 90 *bpm*, proppant size is 40/70 *mesh*, and fracture fluid viscosity is 1 *cp*. The overall trend shows erosion increases with increased pounds of proppants. However, the differences between the proppant concentrations are negligible. One factor to keep in mind is the treatment time as it would take eight times the amount of time to achieve the same injected proppants for a 0.5 lb_m/gal compared to a 4 lb_m/gal. The base case of 2 lb_m/gal should be preferred simulation wise as 4 lb_m/gal is more concentrated for the slurry and it could require a more computationally intensive simulation via discrete element method (DEM) if the concentration is denser than the DPM concentration ideal threshold of 10-12%.

4.3.4 Proppant Size

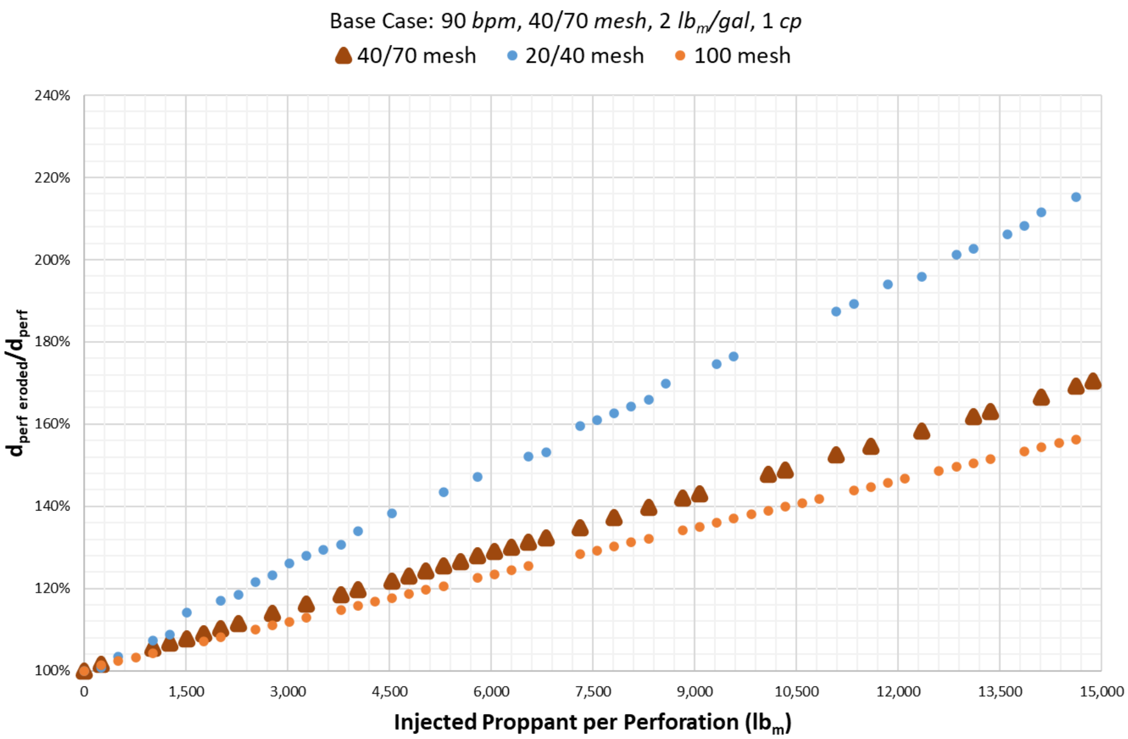

Figure **4-13** Effect of Proppant Size

Figure 4-13 shows the ratio of eroded d_{perf} to the original d_{perf} vs. *pounds* of proppants for proppant sizes of 20/40 *mesh*, 40/70 *mesh*, and 100 *mesh* where treatment rate is 90 *bpm*, proppant concentration is 2 lb_m/gal, and fracture fluid viscosity is 1 *cp*. All three size distributions are distributed using Rosin-Rammler distribution with a spread parameter of 3.5. The 20/40 *mesh* distribution has a mean diameter of 558 μm. The 40/70 *mesh* distribution has a mean diameter of 284 μm. The 100 *mesh* is the distribution of 70/140 *mesh* with a mean diameter of 180 μm. The overall trend shows erosion increases with increased pounds of proppants. The results show the erosion increases with increasing proppant sizes and larger proppant. The larger particles will carry more momentum as they impinge the wall, thus leading to a higher erosion rate. The smaller particles are easier for the fluid to carry as they converge into a perforation, whereas the larger particles would have a higher probability to impinge the perforation entrance edges and the walls.

4.3.5 Fracture Fluid Viscosity

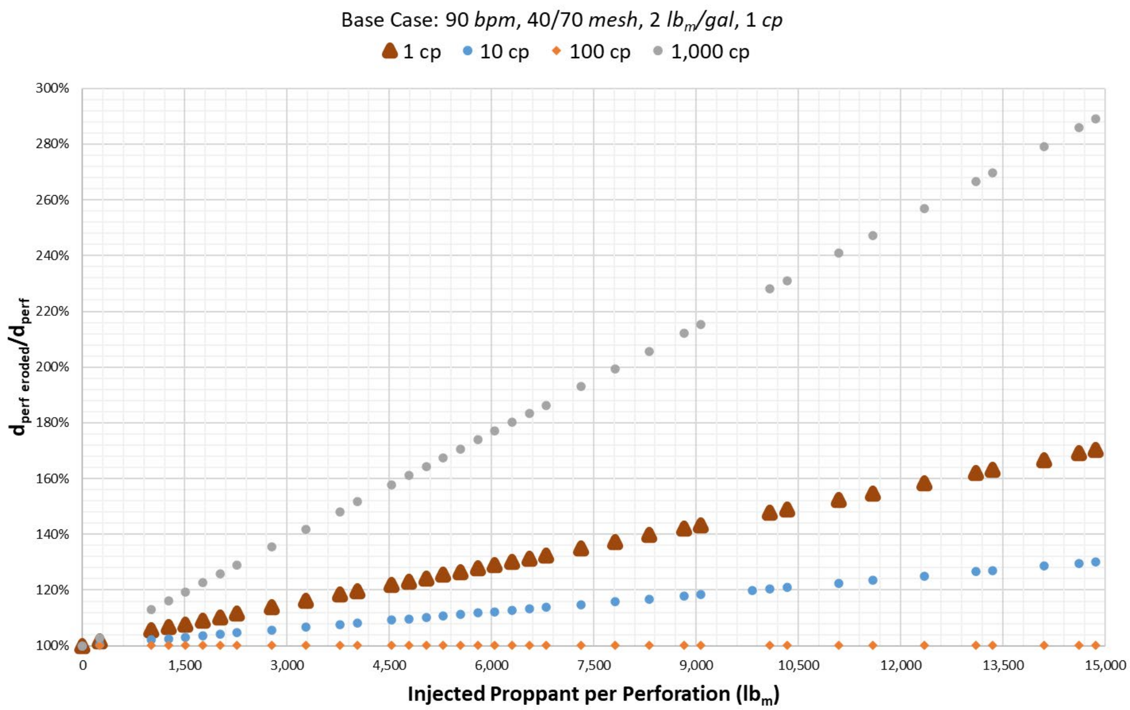

Figure **4-14** Effect of Fracture Fluid Viscosity

Figure 4-14 shows the ratio of eroded d_{perf} to the original d_{perf} vs. *pounds* of proppants for fracture fluid viscosities of 1 *cp*, 10 *cp*, 100 *cp*, and 1,000 *cp* where treatment rate is 90 *bpm*, proppant concentration is 2 lb_m/gal, and proppant size is 40/70 *mesh*. The overall trend shows erosion increases with increasing pounds of proppants. From **Figure 4-14**, we observed a decrease in erosion to the d_{perf} with increasing viscosities for the 10 and 100 *cp*, with 100 *cp* displaying negligible erosion. For the high viscosity fluid however, we observed a much higher erosion to the d_{perf} for the 1,000 *cp*. The mechanisms affecting fracture fluid viscosity and erosion rate are not well known as only a few studies have been performed to examine the effects of fracture fluid viscosity on erosion rate. Okita et al. (2012) conducted CFD studies to examine the effects of fluid viscosity to erosion rate, as they found the increasing fluid viscosity reduces the erosion rate of small and medium-sized particles (less than 0.150 *mm*). However, their viscosities only range from 1 *cp* to 50 *cp*. Sun et al. (2013) observed the erosion rate increases with increasing viscosity at higher viscosities between 125 *cp* to 625 *cp* through their experimental studies.

Figure 4-15 and **Figure 4-16** show the velocity contours for different viscosities at t = 3540 *s*. We noticed the downstream (to the perforation outlet) velocity profile for the high viscous fluid exhibits laminar flow. We can also observe the high viscous fluid entering the perforation experiences more curvature streamlines compare to the low viscous fluid. We furthered examined the turbulent properties for the flow domain as **Figure 4-17** shows the turbulent kinetic energy near the perforation entrance for different viscosities at t = 3540 *s*. It should exhibit laminar flow for the high viscous fluid (1,000 cp) as it has Reynolds number around 100 for the perforation entrance. However, we observed that the turbulence kinetic energy to be much higher for the high viscous fluid (1,000 cp), especially around the edges of the perforation entrance. The turbulent kinetic energy is the quantitative measure of the intensity of turbulence for a given flow as it is defined as the mean kinetic energy per unit mass; it is the difference between the instantaneous and mean velocity as it represents the fluctuations associated with the turbulence in each direction. The viscous shear stress dominates in the near wall region along with this type of flow geometry could possibly contribute to the high turbulence we are observing for the high viscous case. Based on the Ziskind et al. (2002) study on motion of inertial particles in shear flow near a solid surface, that if the particle size is the same, particles tend to impinge more frequently in high viscous liquid than particles in low viscous liquids. The high number of impingements for smaller particles is mostly likely due to the stable particle motion as particles impinge the wall and rebound, the smaller particles do have enough momentum to overcome the drag of the fluid and leave the shear layer. Instead, the particles are pushed back to the wall region and repeat the impingement motion.

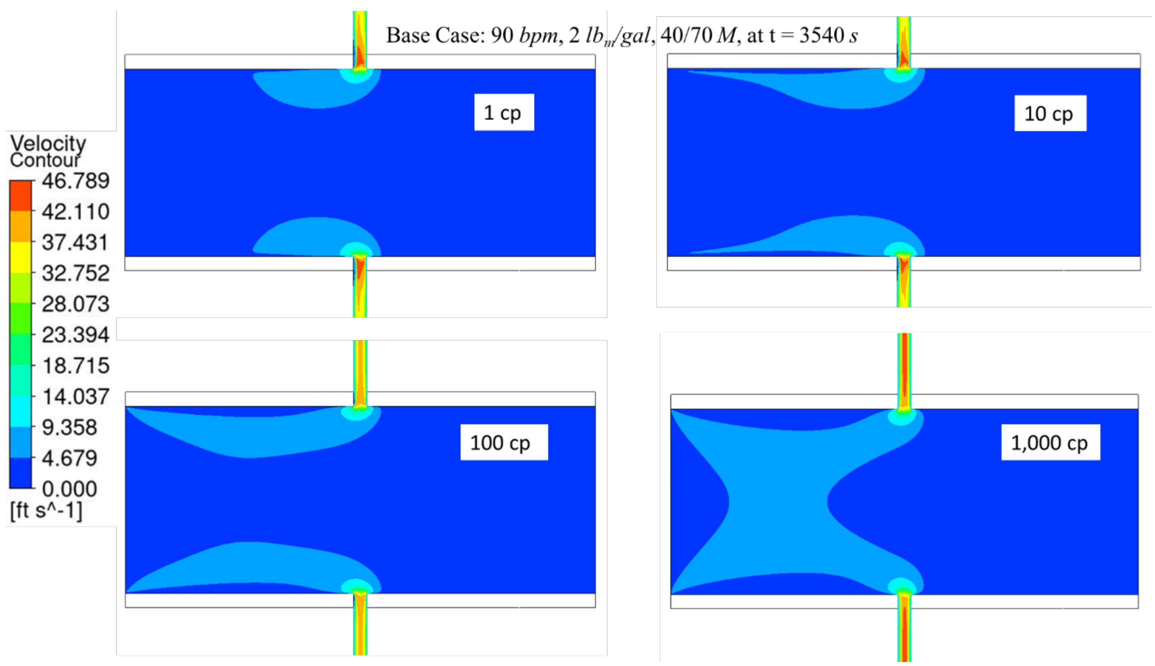

Figure **4-15** Velocity Contours for Base Case at 3540 *s* for Different Viscosities

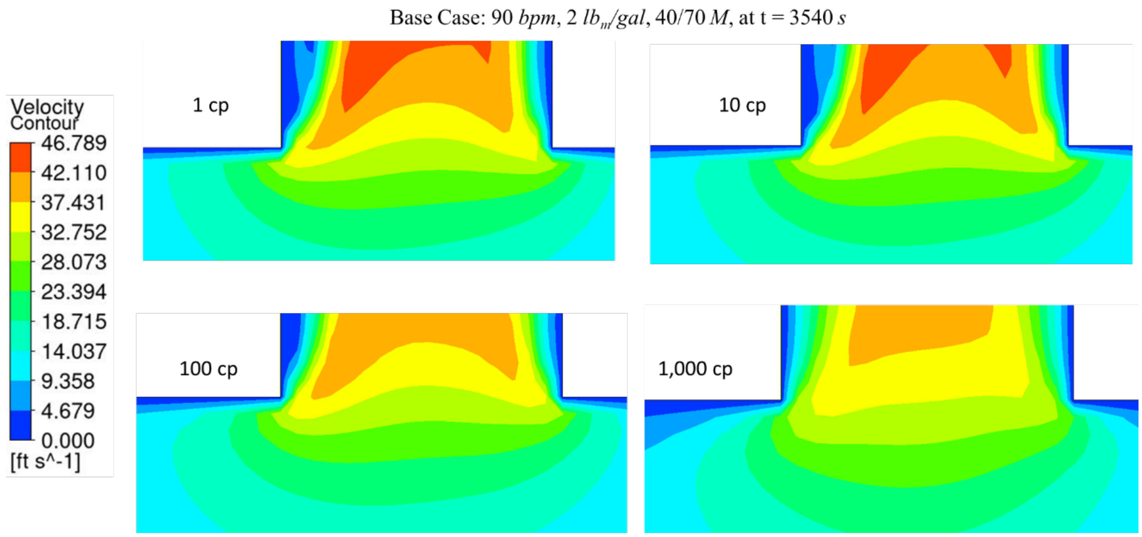

Figure **4-16** Perforation Velocity Contours for Base Case at 3540 *s* for Different Viscosities

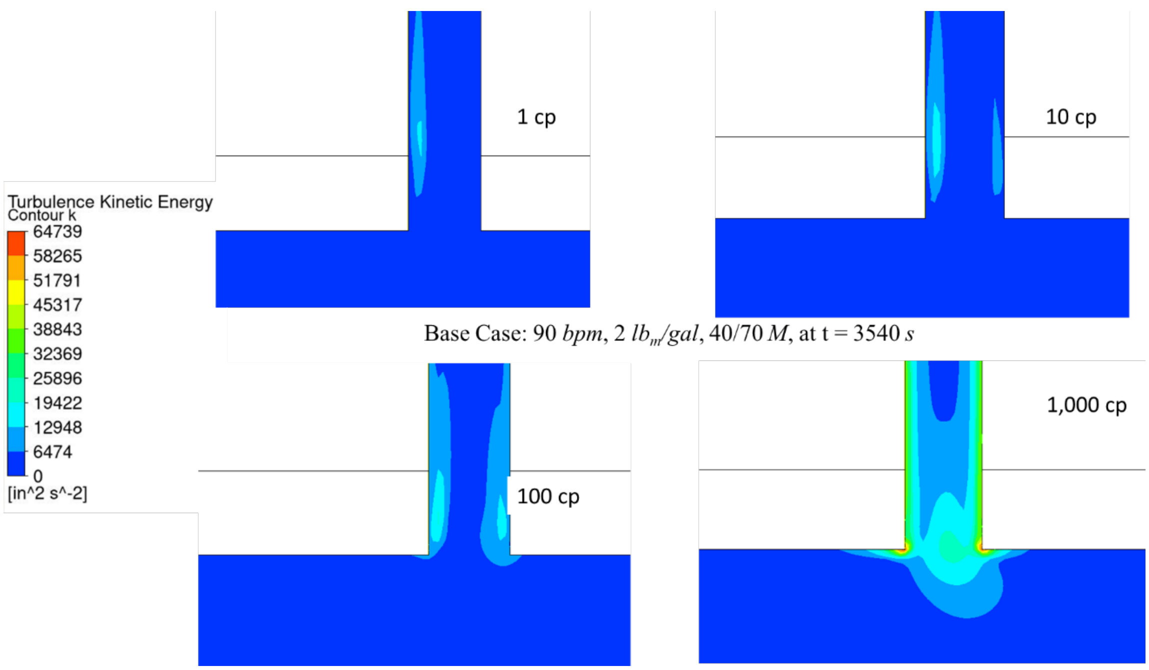

Figure **4-17** Perforation Turbulence Kinetic Energy Contours for Base Case at 3540 *s* for Different Viscosities

We observed similar trends for the 100 *mesh* as well as shown in **Figure 4-18**. But for the 100 *mesh*, the results show negligible erosion to the d_{perf} for both of the 10 and 100 *cp* cases.

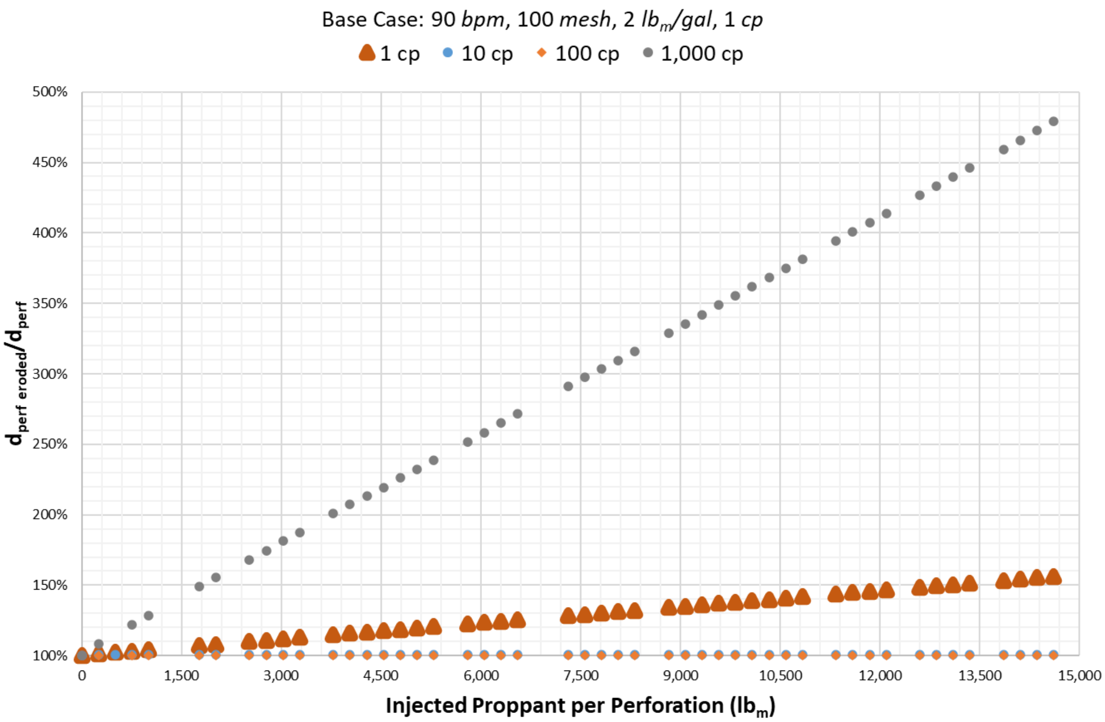

Figure **4-18** Effect of Fracture fluid viscosity

4.4 Conclusion

After performing parametric studies to examine the erosion effects of treatment rates, proppant concentrations, proppant sizes, and fracture fluid viscosities, the observations and recommendations are summarized as the following:

- Higher treatment rate will lead to higher erosion to the d_{perf} and vice versa. To minimize the erosion to the perforation diameter, lower treatment rate is recommended. However, lower treatment rate will also need more stimulation time which will lead to more treatment time.
- Different proppant concentrations have negligible effects toward the erosion to the d_{perf}, with lower concentration leads to slightly higher erosion to the perforation diameter.
- Larger proppant sizes will lead to higher erosion to the d_{perf} and vice versa. To minimize the erosion to the perforation diameter, both 40/70 *mesh* and 100 *mesh* are recommended as the erosion rate between the two proppant sizes are not significantly different; both sizes are widely used throughout the industry as well.
- Higher fracture fluid viscosity will reduce erosion to the d_{perf} for the 10 *cp* and 100 *cp*. However, the erosion becomes significantly higher for the much higher viscous fluid such as 1,000 *cp*. To minimize the erosion to the d_{perf}, 10 and 100 *cp* are recommended for the fracture fluid.

Reference

Behrmann, L.A., and J.L. Elbel. "Effect of Perforations on Fracture Initiation." *J Pet Technol* 43 (1991): 608–615.

Behrmann, L.A., 2012. Personal communication.

Blatt, W., et al. "The Influence of Hydrodynamics on Erosion-Corrosion in Two-Phase Liquid-Particle Flow." *CORROSION*, vol. 45, no. 10, 1989, pp. 793–804., doi:10.5006/1.3584985.

Cheng, Cheng, et al. "Optimal Perforation Location and Limited Entry Design for Promoting Simultaneous Growth of Multiple Hydraulic Fractures." *Day 1 Tue, February 09, 2016*, 2016, doi:10.2118/179158-ms.

Cramer, D.D. *Limited entry extended to massive hydraulic fracturing*. United States: N. p., 1987. Web.

Crump, J.B., and M.W. Conway. "Effects of Perforation-Entry Friction on Bottomhole Treating Analysis." *J Pet Technol* 40 (1988): 1041–1048. doi: https://doi-org.ezaccess.libraries.psu.edu/10.2118/15474-PA

El Rabaa, W. "Experimental Study of Hydraulic Fracture Geometry Initiated From Horizontal Wells." Paper presented at the SPE Annual Technical Conference and Exhibition, San Antonio, Texas, October 1989. doi: https://doi-org.ezaccess.libraries.psu.edu/10.2118/19720-MS

Gruesbeck, C., and R.E. Collins. "Entrainment and Deposition of Fine Particles in Porous Media." *SPE J.* 22 (1982): 847–856. doi: https://doi-org.ezaccess.libraries.psu.edu/10.2118/8430-PA

Ketter, Aaron Allen, Daniels, John Leonard, Heinze, James R., and George Waters. "A Field Study Optimizing Completion Strategies for Fracture Initiation in Barnett Shale Horizontal Wells." Paper presented at the SPE Annual Technical Conference and Exhibition, San Antonio, Texas, USA, September 2006. doi: https://doi-org.ezaccess.libraries.psu.edu/10.2118/103232-MS

Koneti, Srinivasa, and Samit Gokhale, 2015. “Brittle Longitudinal Splits of P-110 Couplings Due to Local Material Defects and Insufficient Control of Material Properties During Manufacturing of High Collapse P-110 Casing.” *SPE/IADC Drilling Conference and Exhibition*, p. D031S015R008, doi:10.2118/173044-MS.

Lagrone, K.W., and J.W. Rasmussen. "A New Development in Completion Methods-The Limited Entry Technique." *J Pet Technol* 15 (1963): 695–702. doi: https://doi-org.ezaccess.libraries.psu.edu/10.2118/530-PA

Lecampion, Brice, and Jean Desroches. “Simultaneous Initiation and Growth of Multiple Radial Hydraulic Fractures from a Horizontal Wellbore.” *Journal of the Mechanics and Physics of Solids*, vol. 82, 2015, pp. 235–258., doi:10.1016/j.jmps.2015.05.010.

Li, J. G., et al. “A Microstructural Investigation of the Surface of a Drilled Hole in Carbon Steels.” *Acta Materialia*, vol. 55, no. 4, 2007, pp. 1397–406, doi:10.1016/j.actamat.2006.09.043.

Li, Yongming, et al. “Influence of Perforation Erosion on Multiple Growing Hydraulic Fractures in Multi-Stage Fracturing.” *Natural Gas Industry B*, vol. 5, no. 1, 2018, pp. 8–15., doi:10.1016/j.ngib.2017.11.002.

Loehken, Joern , Yosefnejad, Davood , and Bernd Fricke. "Experimental Investigation on Parameters Affecting the Coefficient of Discharge of a Perforation Hole in Hydraulic Fracturing Treatments." Paper presented at the SPE Hydraulic Fracturing Technology Conference and Exhibition, The Woodlands, Texas, USA, February 2020. doi: https://doi-org.ezaccess.libraries.psu.edu/10.2118/199746-MS

Long, Gongbo , and Guanshui Xu. "The Effects of Perforation Erosion on Practical Hydraulic-Fracturing Applications." *SPE J.* 22 (2017): 645–659. doi: https://doi-org.ezaccess.libraries.psu.edu/10.2118/185173-PA

McLaury, B.S., 1993. "A Model to Predict Solid Particle Erosion in Oilfield Geometries." Master's Thesis, The University of Tulsa.

McLaury, B.S., Shadley, J.R., and Rybicki, E.F. "Modeling Erosion in Chokes," ASME-Fluids Engineering 236, 1 (1996): pp. 773-782.

Morita, Nobuo, and Sogo Shiozawa, 2014. "Stability Analysis of Casings During Plastic Deformation." *SPE Deepwater Drilling and Completions Conference*, p. D011S001R003, doi:10.2118/170303-MS.

Okita, Risa, et al. "Experimental and Computational Investigations to Evaluate the Effects of Fluid Viscosity and Particle Size on Erosion Damage." *Journal of Fluids Engineering, Transactions of the ASME*, vol. 134, no. 6, 2012, pp. 1–13, doi:10.1115/1.4005683.

Parsi, Mazdak, et al. "A Comprehensive Review of Solid Particle Erosion Modeling for Oil and Gas Wells and Pipelines Applications." *Journal of Natural Gas Science and Engineering*, vol. 21, 2014, pp. 850–873., doi:10.1016/j.jngse.2014.10.001.

Pavlina, E. J., and C. J. Van Tyne, 2008. “Correlation of Yield Strength and Tensile Strength with Hardness for Steels.” *Journal of Materials Engineering and Performance*, vol. 17, no. 6, pp. 888–93, doi:10.1007/s11665-008-9225-5.

Robinson, Stephen , Littleford, Thomas , Luu, Tim , Wardynski, Kacper , Evans, Andrew , Horton, Blake , and Michael Oman. "Acoustic Imaging of Perforation Erosion in Hydraulically Fractured Wells for Optimizing Cluster Efficiency." Paper presented at the SPE Hydraulic Fracturing Technology Conference and Exhibition, The Woodlands, Texas, USA, February 2020.

Romero, Louis A., et al. “Phase Encoding of Shot Records in Prestack Migration.” *GEOPHYSICS*, vol. 65, no. 2, 2000, pp. 426–436., doi:10.1190/1.1444737.

Somanchi, Kiran, O'Brien, Cris, Huckabee, Paul, and Gustavo Ugueto. "Insights and Observations into Limited Entry Perforation Dynamics from Fiber-Optic Diagnostics." Paper presented at the SPE/AAPG/SEG Unconventional Resources Technology Conference, San Antonio, Texas, USA, August 2016. doi: https://doi-org.ezaccess.libraries.psu.edu/10.15530/URTEC-2016-2458389

Sun, Ke, and Lin Lu. “Particle Flow Behavior of Distribution and Deposition throughout 90° Bends: Analysis of Influencing Factors.” *Journal of Aerosol Science*, vol. 65, Elsevier, 2013, pp. 26–41, doi:10.1016/j.jaerosci.2013.07.002.

Wasp, E.J., Kenny, J.P., Aude, T.C., Seiter, R.H., Jacques, R.B., 1970 Deposition velocities transition velocities and spatial distribution of solids in slurry pipelines. In: Hydro Transport 1, paper H42, BHRA Fluid Engineering, Coventry, pp. 53-76.

Willingham, J.D., Tan, H.C., and L.R. Norman. "Perforation Friction Pressure of Fracturing Fluid Slurries." Paper presented at the Low Permeability Reservoirs Symposium, Denver, Colorado, April 1993. doi: https://doi-org.ezaccess.libraries.psu.edu/10.2118/25891-MS

Xu, Tianhan, et al., 2012. "Study on the Static and Dynamic Fracture Mechanism of Different Casing-Drilling Steel Grades." *Materials Characterization*, vol. 67, pp. 1–9, doi:10.1016/j.matchar.2012.02.016.

Yosefnejad, Davood M., Fricke, Bernd , Loehken, Joern , and Liam McNelis. "The Role of Back Pressure and Perforation Hole Erosion on the Magnitude of the Coefficient of Discharge in Hydraulic Fracturing Stimulation." Paper presented at the SPE Europec, Virtual, December 2020.

Zhang, Yongli, et al. "Simulations of Particle-Wall-Turbulence Interactions, Particle Motion and Erosion in With a Commercial CFD Code." *Volume 1: Symposia, Parts A and B*, 2006, doi:10.1115/fedsm2006-98037.

Zhang, Jun, McLaury, Brenton S., and Siamack A. Shirazi. "Predicting Erosion from Small Particles in Sudden Contraction and Expansion Geometries with Improved Near Wall Treatment." Paper presented at the CORROSION 2016, Vancouver, British Columbia, Canada, March 2016.

Zhao Jinzhou, Xu Wenjun, Li Yongming. "A new method for cluster spacing optimization of multi-cluster staged fracturing in horizontal wells of low-permeability oil and gas reservoirs". NATURAL GAS INDUSTRY, 2016, 36(10): 63-69.

Ziskind, Gennady and Chaim Gutfinger. “Shear and gravity effects on particle motion in turbulent boundary layers.” *Powder Technology* 125 (2002): 140-148.

Chapter 5

Summary

To meet the needs for shale gas development and accurate measurement of high-volume gas wells, this paper provides a comprehensive and in-depth review and analysis of applicable metering and gas volume measurement technologies, including Coriolis, turbine, v-cone, and orifice meters. Conclusions include:

- For accurate orifice metering, one needs to understand and calibrate meters to eliminate effects of installation, swirl, chemical and organic contamination, physical deformation, etc.
- Out of the factors affecting Orifice metering and measurement, orifice bore diameter, flowing pressure, differential pressure, and gas composition affect measurement the most (in order of high to low impact). Flowing time is critical especially when gas flow is not continuous, such as when a plunger lift is installed.

We observed that in dry gas Marcellus and Utica gas region, most wells, with the except of one operator and twelve wells out of hundreds and thousands of wells, were equipped with orifice metering and measurement for its low cost, accuracy, and ease of calibration and maintenance. As gas flow rates drop and Reynolds number decreases, one could and should change Orifice plate size and calibrate the meter to maintain accuracy of measurement.

This part of the study provides one with up-to-date understanding of physics and practices needed in natural gas metering and volume measurement. Meter design and measurement could be improved if the following factors could be considered: variable flow rates during the life of a shale gas well, compositional change of shale gas, and potential storage and measurement of CO_2, H_2, and CH_4.

We performed parametric studies via CFD to further analyze the various factors that could affect the measurement accuracy of the orifice meter. We observed the effects of the chemical and organic contamination on the orifice bore plate as wider contamination layer would cause an increase in changes of the discharge coefficient. We also observed the most magnitude changes occurs when the length of the layer covers half of the orifice plate. We observed the following trends from the effects of erosion rate on the orifice bore plate through different particle sizes and gas flow rates:

- As particle sizes get smaller, we observed an increase in terms of maximum erosion on the orifice bore plate.
- As gas flow rates increase, we observed an increase of maximum erosion rate on the orifice bore plate for larger sized particles (100 μm and 300 μm). However, for the smaller sized particles (1 μm and 10 μm), we observed the opposite trend where an increase in gas flow rate would lead to a decrease in maximum erosion rate on the orifice bore plate.

We also observed that the magnitude of the erosion rate is quite small for all cases, to the point that it can be neglected as it would cause minimal changes to the orifice bore plate for a period of operation time since our studies are conducted based on 24 hours of flowing time. Since most of the sand particles will be filtered out before entering the orifice metering tube, we can conclude that the unfiltered sand particles carried by the flowing gas would have a negligible effect to the orifice bore plate. If the orifice bore plate was damaged due to particle erosion before the recommended plate changing schedule, it would most likely due to a dysfunction of the filters or other effects such as chemical and organic contamination, physical deformation, or some other uncertainty effects.

We performed parametric studies to examine the erosion effects of treatment rates, proppant concentrations, proppant sizes, and fracture fluid viscosities. The observations and recommendations are summarized as the following:

- Higher treatment rate will lead to higher erosion to the d_{perf} and vice versa. To minimize the erosion to the perforation diameter, lower treatment rate is recommended. However, lower treatment rate will also need more stimulation time which will lead to more treatment time.
- Different proppant concentrations have negligible effects toward the erosion to the d_{perf}, with lower concentration leads to slightly higher erosion to the perforation diameter.
- Larger proppant sizes will lead to higher erosion to the d_{perf} and vice versa. To minimize the erosion to the perforation diameter, both 40/70 *mesh* and 100 *mesh* are recommended as the erosion rate between the two proppant sizes are not significantly different; both sizes are widely used throughout the industry as well.
- Higher fracture fluid viscosity will reduce erosion to the d_{perf} for the 10 *cp* and 100 *cp*. However, the erosion becomes significantly higher for the much higher viscous fluid such as 1,000 *cp*. To minimize the erosion to the d_{perf}, 10 and 100 *cp* are recommended for the fracture fluid.

As perforation erosion is still relatively unknown area in the industry, we would like to continue to build upon our CFD model to further expand the capabilities, such as different SPF configurations, different geometries for the perforation to simulate the burr effects from the gun charges, increase the treatment cluster length/spacing, and increase the number of treatment clusters/stages. For future works, we should further examine the effects of fluid viscosities to the perforation erosion as this is also a relatively unknown area, especially as we observed the high turbulence kinetic energy associated with high viscous fluid near the perforation entrance. We can also expand our CFD model further to setup different cases based on all these suggested factors to examine the erosion effects from the treatment and the proppants.

Appendix A. Orifice Codes Validation

β=0.20618 d=1.2496 inch D = 6.606 inch

Run No.	Date	h_w (inch)	pf_1 (PSIA)	Temp (F)	Q_m (lb/sec)	Cd	ReD	ρ (lb/CF)
501	9/10/1984	6.1	682.53	77.42	0.33852	0.59767	117301	2.16385
502	9/10/1984	6.1	681.83	79.3	0.337543	0.59767	116981	2.15122
503	9/10/1984	6.1	681.14	81.03	0.336665	0.59767	116694	2.13989
504	9/10/1984	6.1	680.2	82.63	0.335768	0.59767	116398	2.12837
505	9/11/1984	17.4	637.19	95.18	0.539148	0.59745	187090	1.92518
506	9/11/1984	17.5	637.4	95.1	0.54082	0.59745	187669	1.92609
507	9/11/1984	17.6	638.2	94.96	0.54284	0.59745	188368	1.9295
508	9/11/1984	17.8	647.9	95.24	0.550197	0.59744	190925	1.95989
509	9/11/1984	44	653.98	91.42	0.872555	0.59729	302694	1.99725
510	9/11/1984	44	655.13	90.63	0.874167	0.59729	303233	2.00469
511	9/11/1984	44.1	656.19	89.88	0.876682	0.59728	304088	2.01173
512	9/11/1984	44.2	657.21	89.21	0.879112	0.59728	304914	2.01838
513	9/12/1984	91.8	660.15	87.13	1.271897	0.59719	441072	2.03835
514	9/12/1984	91.6	658.13	87.44	1.267878	0.59719	439690	2.02989
515	9/12/1984	91.2	656.08	87.43	1.262984	0.59719	437992	2.02307
516	9/12/1984	90.9	654.24	87.11	1.259499	0.59719	436772	2.01857
517	9/12/1984	141.4	648.55	87.22	1.561723	0.59715	541582	1.99903
518	9/12/1984	141.1	647.05	87.06	1.558484	0.59715	540452	1.99499
519	9/12/1984	140.9	646.25	87.03	1.556357	0.59715	539713	1.99237
520	9/12/1984	140.7	645.35	87.4	1.553348	0.59715	538685	1.98747

β=0.37125 d=2.25 inch D = 6.606 inch

Run No.	Date	h_w (inch)	pf_1 (PSIA)	Temp (F)	Q_m (lb/sec)	Cd	ReD	ρ (lb/CF)
344	8/15/1984	9.2	714.07	82.27	1.3905366	0.60001	482127	2.24567
345	8/15/1984	9.2	714.43	82.25	1.3910047	0.60001	482289	2.24719
346	8/15/1984	9.2	714.81	82.36	1.3912362	0.60001	482374	2.24793
347	8/15/1984	9.2	715.23	82.33	1.3916824	0.60001	482527	2.24937
348	8/15/1984	9.2	715.55	82.23	1.3921193	0.60001	482675	2.25079
349	8/15/1984	9.2	715.91	82.1	1.3928185	0.60001	482912	2.25307
350	8/15/1984	38.2	716.76	80.38	2.8432432	0.59976	985600	2.26534
351	8/15/1984	38.2	717.33	80.63	2.8437297	0.59976	985789	2.2661
352	8/15/1984	38.3	717.82	80.67	2.8483129	0.59976	987381	2.26748
353	8/15/1984	38.3	718.33	80.44	2.8503001	0.59976	988051	2.27066
354	8/15/1984	38.3	718.75	80.92	2.8495132	0.59976	987818	2.26936
355	8/15/1984	38.4	719.15	80.99	2.8538379	0.59976	989323	2.27033
594	9/20/1984	139.2	652.06	81.86	5.1357622	0.59961	1780447	2.03673
595	9/20/1984	139.1	651.53	81.25	5.1353437	0.59961	1780211	2.03791
596	9/20/1984	139	650.78	81.1	5.1312351	0.59961	1778765	2.03613
597	9/20/1984	138.8	650.09	81.35	5.1229922	0.59962	1775945	2.03249
602	9/21/1984	8.9	695.37	87.11	1.3403394	0.60002	464909	2.15629
603	9/21/1984	8.9	695.11	86.8	1.3404611	0.60002	464939	2.15671
604	9/21/1984	8.9	694.89	86.6	1.3406669	0.60002	465003	2.15739
605	9/21/1984	8.9	694.25	85.92	1.3410449	0.60002	465109	2.15866

β=0.57724 d=3.4984 inch D = 6.606 inch

Run No.	Date	h_w (inch)	pf_1 (PSIA)	Temp (F)	Q_m (lb/sec)	Cd	ReD	ρ (lb/CF)
176	8/3/1984	20.3	628.47	85.98	4.9089125	0.60454	1703065	1.93796
177	8/3/1984	20.3	628.34	86.4	4.9062346	0.60454	1702194	1.93582
178	8/3/1984	20.3	628.2	86.68	4.9041354	0.60454	1701505	1.93414
179	8/3/1984	20.3	628.09	86.47	4.9046288	0.60454	1701647	1.93454
180	8/3/1984	20.3	627.94	85.57	4.9092939	0.60454	1703140	1.9383
181	8/3/1984	20.3	627.83	85.48	4.9092606	0.60454	1703116	1.93828
182	8/3/1984	11.2	627.96	85.5	3.6488772	0.60477	1265945	1.93861
183	8/3/1984	11.2	627.85	85.31	3.6494202	0.60477	1266114	1.9392
184	8/3/1984	11.2	627.74	85.32	3.6488281	0.60477	1265910	1.93857
185	8/3/1984	11.2	627.61	85.71	3.6471738	0.60477	1265376	1.93678
186	8/3/1984	11.2	627.44	85.45	3.6475312	0.60477	1265473	1.93718
187	8/3/1984	11.2	627.3	85.47	3.6470592	0.60477	1265312	1.93668
634	9/26/1984	23.1	713.21	86.84	5.6005743	0.60444	1943112	2.21741
635	9/26/1984	23.1	714.02	86.81	5.6046475	0.60444	1944520	2.22064
636	9/26/1984	23.1	714.49	86.75	5.6067924	0.60444	1945254	2.22235
637	9/26/1984	23.1	714.88	86.63	5.6096699	0.60444	1946234	2.22464
644	9/26/1984	92.7	721.27	80.02	11.360905	0.60402	3938973	2.28295
645	9/26/1984	92.7	721.67	79.98	11.365993	0.60402	3940724	2.28499
646	9/26/1984	92.7	721.81	79.93	11.367614	0.60402	3941269	2.28565
647	9/26/1984	92.8	722.17	79.75	11.37842	0.60402	3944956	2.28755

β=0.37405 *d*=3.748 inch *D* = 10.02 inch

Run No.	Date	h_w (inch)	pf_1 (PSIA)	Temp (F)	Q_m (lb/sec)	Cd	ReD	ρ (lb/CF)
795	10/18/1984	16.8	605.97	89.24	4.7337266	0.60006	993241	1.84969
796	10/18/1984	16.8	605.02	89.25	4.7293521	0.60006	992324	1.84627
797	10/18/1984	16.8	604.53	89.3	4.7272254	0.60006	991882	1.84461
798	10/18/1984	16.8	604.07	89.3	4.7254262	0.60006	991504	1.84321
799	10/18/1984	37.5	601.89	88.37	7.0495074	0.59996	1479001	1.83991
800	10/18/1984	37.5	601.94	87.78	7.0549067	0.59996	1480063	1.84277
801	10/18/1984	37.4	601.84	87.49	7.0467534	0.59996	1478318	1.84344
802	10/18/1984	37.4	601.78	87.12	7.0496605	0.59996	1478883	1.84499
803	10/18/1984	102.6	597.62	80.95	11.699331	0.59986	2452981	1.85802
804	10/18/1984	103.3	601.31	81.24	11.773778	0.59986	2468649	1.86898
805	10/18/1984	102.7	598.59	81.38	11.709976	0.59986	2455301	1.85956
806	10/18/1984	102.8	598.7	81.58	11.713071	0.59986	2455990	1.85873
807	10/18/1984	147.9	596.41	79.26	14.046336	0.59983	2944632	1.86154
808	10/18/1984	147.8	596.33	79.34	14.039647	0.59983	2943250	1.86102
809	10/18/1984	148	596.69	79.35	14.053221	0.59983	2946098	1.86211
810	10/18/1984	148	596.97	79.46	14.055131	0.59983	2946525	1.8626

β=0.49876 d=4.9976 inch D = 10.02 inch

Run No.	Date	h_w (inch)	pf_1 (PSIA)	Temp (F)	Q_m (lb/sec)	Cd	ReD	ρ (lb/CF)
712	10/12/1984	12.2	648.84	83.61	7.69447	0.60297	1614046	2.017473
713	10/12/1984	12.2	648.33	83.66	7.6906	0.60297	1613239	2.015435
714	10/12/1984	12.2	647.94	83.7	7.6875	0.60297	1612595	2.013808
715	10/12/1984	12.2	647.77	83.69	7.68656	0.60297	1612397	2.013317
716	10/12/1984	21.4	646.43	81.43	10.1928	0.60285	2137641	2.019946
717	10/12/1984	21.4	646.26	81.45	10.1906	0.60285	2137184	2.019073
718	10/12/1984	21.3	645.96	81.45	10.1644	0.60285	2131697	2.018136
719	10/12/1984	21.3	645.71	81.49	10.1621	0.60285	2131215	2.017206
720	10/12/1984	47.9	642.16	77.3	15.2589	0.6027	3198863	2.025789
721	10/12/1984	47.8	641.79	77.32	15.2373	0.6027	3194344	2.024278
722	10/12/1984	47.9	641.81	77.27	15.2542	0.6027	3197857	2.024529
723	10/12/1984	47.8	641.64	77.2	15.2382	0.6027	3194499	2.024525
727	10/12/1984	98.8	635.76	72.48	21.8982	0.60258	4588666	2.027796
728	10/12/1984	98.8	635.67	72.5	21.8963	0.60258	4588264	2.027433
729	10/12/1984	98.7	635.54	72.56	21.8818	0.60258	4585251	2.02679
730	10/12/1984	98.8	635.61	72.7	21.8912	0.60258	4587281	2.02648
731	10/12/1984	148.6	632.48	70.1	26.8316	0.60253	5621171	2.028552
732	10/12/1984	148.5	632.27	70.08	26.8186	0.60253	5618447	2.027955
733	10/12/1984	148.3	631.2	70.04	26.7771	0.60253	5609724	2.024407
734	10/12/1984	148.2	630.83	70.04	26.7585	0.60253	5605820	2.022952

β=0.57373 d=5.7488 inch D = 10.02 inch

Run No.	Date	h_w (inch)	pf_1 (PSIA)	Temp (F)	Q_m (lb/sec)	Cd	ReD	ρ (lb/CF)
755	10/16/1984	12.4	687.97	82.48	10.9048	0.60418	2287486	2.155566
756	10/16/1984	12.4	688.09	83.1	10.8967	0.60418	2285916	2.152335
757	10/16/1984	12.4	688.2	83.42	10.8945	0.60418	2285499	2.151411
758	10/16/1984	12.4	688.32	83.5	10.8946	0.60418	2285549	2.151469
759	10/16/1984	19	676.92	80.35	13.4101	0.60406	2812427	2.129027
760	10/16/1984	19	676.58	80.3	13.4064	0.60406	2811650	2.127872
761	10/16/1984	19	676.11	80.26	13.4023	0.60406	2810766	2.126551
762	10/16/1984	19	675.71	80.22	13.3988	0.60406	2810027	2.12545
763	10/16/1984	56.3	668.21	71.92	23.1332	0.60378	4847754	2.143792
764	10/16/1984	56.3	667.57	71.7	23.1268	0.60378	4846320	2.142625
765	10/16/1984	56.3	667.16	71.56	23.1242	0.60378	4845719	2.142159
766	10/16/1984	56.3	666.81	71.48	23.1199	0.60378	4844771	2.141358
767	10/16/1984	101.3	662.67	68.1	31.0069	0.60365	6495345	2.145414
768	10/16/1984	101.3	662.97	68.04	31.0156	0.60365	6497147	2.146629
769	10/16/1984	101.3	663.12	67.98	31.0209	0.60365	6498212	2.147359
770	10/16/1984	101.3	662.7	67.89	31.0136	0.60365	6496640	2.146365
771	10/16/1984	137.8	655.62	66.24	36.0091	0.60359	7541852	2.130666
772	10/16/1984	137.6	655.12	66.18	35.9689	0.60359	7533401	2.128999
773	10/16/1984	137.7	655.57	66.18	35.9967	0.60359	7539224	2.130747
774	10/16/1984	137.9	655.89	66.15	36.0326	0.60359	7546705	2.131908

Appendix B. Orifice Codes Mass Flowrate Comparison to the Experimental Data

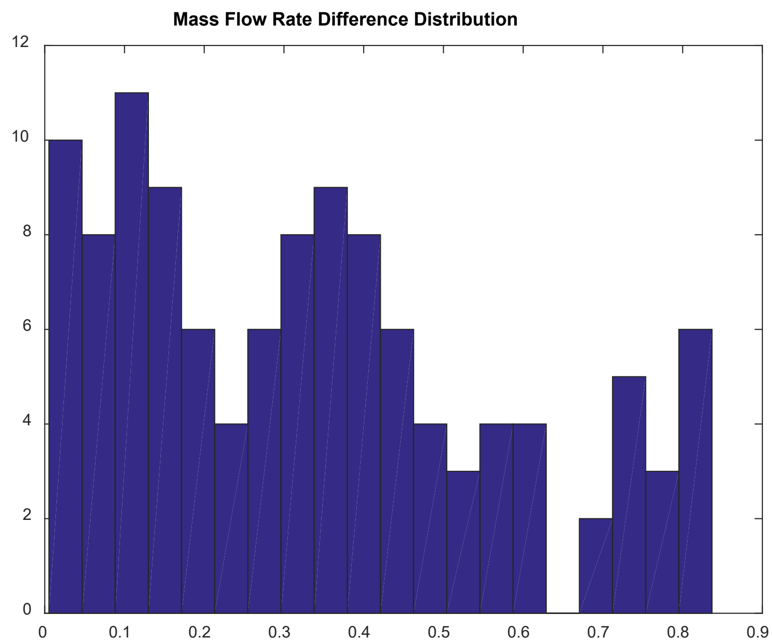

Run No.	Mass FlowRate (Experimental)	Mass FlowRate (Calculated)	Difference (lbm/sec)	Difference %
501	0.33862	0.33852	0.0001	0.029558
502	0.33782	0.337543	0.000277	0.081862
503	0.33703	0.336665	0.000365	0.108342
504	0.33616	0.335768	0.000392	0.116602
505	0.5399	0.539148	0.000752	0.139281
506	0.54017	0.54082	0.00065	0.120394
507	0.54086	0.54284	0.00198	0.366042
508	0.5491	0.550197	0.001097	0.199786
509	0.87305	0.872555	0.000495	0.056657
510	0.87539	0.874167	0.001223	0.139738
511	0.87763	0.876682	0.000948	0.108019
512	0.87981	0.879112	0.000698	0.07928
513	1.27546	1.271897	0.003563	0.27935
514	1.27099	1.267878	0.003112	0.244846

515	1.26673	1.262984	0.003746	0.295742
516	1.25797	1.259499	0.001529	0.121515
517	1.56774	1.561723	0.006017	0.383771
518	1.56417	1.558484	0.005686	0.363488
519	1.56213	1.556357	0.005773	0.369556
520	1.55938	1.553348	0.006032	0.386849
344	1.39466	1.390537	0.004123	0.29566
345	1.39555	1.391005	0.004545	0.3257
346	1.39604	1.391236	0.004804	0.344105
347	1.3968	1.391682	0.005118	0.366383
348	1.39753	1.392119	0.005411	0.387162
349	1.39836	1.392819	0.005541	0.396283
350	2.8598	2.843243	0.016557	0.578949
351	2.86158	2.84373	0.01785	0.623792
352	2.86359	2.848313	0.015277	0.533494
353	2.86674	2.8503	0.01644	0.573471
354	2.86718	2.849513	0.017667	0.616174
355	2.8682	2.853838	0.014362	0.500737
594	5.15403	5.135762	0.018268	0.354438
595	5.15269	5.135344	0.017346	0.336645
596	5.14815	5.131235	0.016915	0.328562
597	5.14138	5.122992	0.018388	0.357644
602	1.33991	1.340339	0.000429	0.03205
603	1.33967	1.340461	0.000791	0.059048
604	1.3395	1.340667	0.001167	0.087117
605	1.33901	1.341045	0.002035	0.151972
176	4.94815	4.908913	0.039237	0.792973
177	4.94481	4.906235	0.038575	0.780119
178	4.94198	4.904135	0.037845	0.765779
179	4.94185	4.904629	0.037221	0.753184
180	4.94523	4.909294	0.035936	0.726682
181	4.94527	4.909261	0.036009	0.728158
182	3.67896	3.648877	0.030083	0.817697

183	3.67998	3.64942	0.03056	0.830433
184	3.67962	3.648828	0.030792	0.836822
185	3.67725	3.647174	0.030076	0.817899
186	3.67694	3.647531	0.029409	0.799816
187	3.67655	3.647059	0.029491	0.802132
634	5.61768	5.600574	0.017106	0.304498
635	5.6251	5.604647	0.020453	0.363594
636	5.6296	5.606792	0.022808	0.405136
637	5.63383	5.60967	0.02416	0.428839
644	11.4279	11.36091	0.066995	0.586238
645	11.4351	11.36599	0.069107	0.604342
646	11.4379	11.36761	0.070286	0.614504
647	11.4434	11.37842	0.06498	0.567839
795	4.72666	4.733727	0.007067	0.149505
796	4.71932	4.729352	0.010032	0.212574
797	4.71492	4.727225	0.012305	0.260989
798	4.7112	4.725426	0.014226	0.301966
799	7.04815	7.049507	0.001357	0.019258
800	7.05323	7.054907	0.001677	0.023773
801	7.05449	7.046753	0.007737	0.109669
802	7.05684	7.04966	0.00718	0.101738
803	11.75	11.69933	0.050669	0.431221
804	11.8219	11.77378	0.048122	0.40706
805	11.7642	11.70998	0.054224	0.460923
806	11.762	11.71307	0.048929	0.415993
807	14.1159	14.04634	0.069564	0.492809
808	14.1133	14.03965	0.073653	0.521871
809	14.1227	14.05322	0.069479	0.491966
810	14.1283	14.05513	0.073169	0.517889
712	7.67893	7.694473	0.015543	0.202412
713	7.67218	7.690595	0.018415	0.240024
714	7.66811	7.687498	0.019388	0.252835
715	7.66532	7.686559	0.021239	0.277075

716	10.2062	10.19277	0.013431	0.131592
717	10.2036	10.19057	0.013029	0.127692
718	10.1986	10.16441	0.034192	0.335264
719	10.1942	10.16207	0.032127	0.315154
720	15.3074	15.25891	0.048487	0.316755
721	15.2973	15.23733	0.05997	0.392033
722	15.2986	15.25416	0.044444	0.290509
723	15.2954	15.23822	0.057176	0.373814
727	21.9973	21.89822	0.099084	0.450439
728	21.9956	21.89626	0.099343	0.451648
729	21.9887	21.88177	0.106934	0.486313
730	21.9863	21.89119	0.09511	0.432587
731	27.0205	26.8316	0.188903	0.699111
732	27.0204	26.81864	0.201758	0.746689
733	26.965	26.77709	0.187908	0.696859
734	26.9567	26.75845	0.198248	0.73543
755	10.8919	10.90477	0.012871	0.118171
756	10.8861	10.89673	0.010629	0.097636
757	10.8839	10.89446	0.010556	0.096984
758	10.8853	10.89462	0.009319	0.085614
759	13.3983	13.41008	0.011778	0.087908
760	13.3865	13.40643	0.019929	0.148872
761	13.3771	13.40226	0.025159	0.188073
762	13.3694	13.39878	0.029381	0.21976
763	23.1529	23.13322	0.019685	0.08502
764	23.136	23.12681	0.009192	0.039728
765	23.1262	23.12422	0.001978	0.008553
766	23.0712	23.11985	0.048653	0.210882
767	30.9993	31.00687	0.007568	0.024414
768	31.013	31.01564	0.002636	0.008499
769	31.0225	31.02088	0.001617	0.005211
770	31.0067	31.01362	0.006919	0.022315

771	36.0589	36.0091	0.0498	0.138107
772	36.0331	35.96893	0.064166	0.178076
773	36.0581	35.99674	0.061358	0.170163
774	36.0799	36.03256	0.047341	0.131211

Vita

Yiming Zhang was born in 1988 in Dandong, Liaoning, China. He came to the United States in 2001 in Houston, Texas. After finishing high school, he attended the University of Texas at Austin and finished with a degree in Economics. He then moved to State College in summer of 2013, to purse graduate studies in Petroleum and Natural Gas Engineering. He had to take a year as a nondegree student first to catch up on some Petroleum and Natural Gas related courses giving his background studies. After that, he was able to complete both his Master and Ph.D. degree as he defended his dissertation in June 2022.